UNIVERSITÀ
DEGLI STUDI
DI PADOVA

UNIVERSITÀ DEGLI STUDI DI PADOVA

Dipartimento di Ingegneria Industriale

Scuola di Dottorato di Ricerca in Ingegneria Industriale
Indirizzo in Progettazione e Dinamica dei Sistemi Meccanici
Ciclo XXVI

Sport vehicles and virtual riders modeling

Direttore della Scuola:
Ch.mo Prof. Paolo Colombo

Coordinatore d'Indirizzo:
Ch.mo Prof. Alberto Doria

Supervisore:
Ch.mo Prof. Roberto Lot

Dottorando: Davide Tavernini

A LLA MIA FAMIGLIA E AD ARIANNA *per aver creduto in me ed avermi sostenuto sempre e comunque.*

Contents

Abstract

0.1 Sport vehicles and virtual riders modeling (English version)

The Optimal Maneuver Method is a package for optimal control problem simulations based on the mathematical formulation of a vehicle model capable of getting the dynamics of the system and on the concept of ideal rider.
The work presented in this thesis covers different purposes: the development of the current methodology applied to motorcycles in order to improve matching between experimental evidence results and lap-time simulations, second to formulate different single, two, four-wheeled vehicle models for different application cases. Third to create flexible libraries to manage components that are communal between the different models and require a particular formulation. Fourth to apply the Optimal Maneuver Method for studying the optimality of some specialized driving techniques that are nowadays under investigation, as aggressive maneuvers outside the linear behavior of tires, which knowledge are at the base of modern active chassis control systems.

0.2 Modellazione di veicoli sportivi e piloti virtuali (Italian version)

Il Metodo della Manovra Ottima e' un pacchetto software per simulazioni basate su problemi di controllo ottimo. Esso consiste nella formulazione matematica di un modello di veicolo capace di cogliere la dinamica del sistema a cui e' associato e si basa sul concetto di pilota ideale. Il lavoro presentato in questa tesi copre diversi aspetti: lo sviluppo della gia' esistente metodologia applicata in campo motociclistico al fine di migliorare la corrispondenza tra prove sperimentali e risultati delle simulazioni, secondo la formulazione di diversi modelli di veicolo ad una, due e quattro ruote per diverse applicazioni. Terzo lo sviluppo di un pacchetto di librerie in grado di gestire alcuni componenti comuni a piu' modelli di veicolo che richiedono una particolare formulazione. Quarto l'applicazione del Metodo della Manovra Ottima per lo studio dell'ottimalita' di certe tecniche di guida adottate da piloti professionisti che sono al momento oggetto di studio, come manovre aggressive oltre il comportamento lineare degli pneumatici, la cui comprensione e' alla base dei moderni sistemi di controllo attivo del veicolo.

Introduction

The Optimal Maneuver Method (i.e. OMM) is a package for optimal control problem simulations developed by the Motorcycle Dynamics Research Group of the University of Padova and by the University of Trento.
This methodology has been employed in the last ten years as an advanced tool for the evaluation of maneuverability and handling of racing motorcycles ([1], [2], [3]): the first of the these two properties account for the maximum performance that is achievable with a certain vehicle, the latter considers also pilot effort to exploit a particular maneuver.
The method is based on the mathematical formulation of a vehicle model capable of getting the dynamics of the system and on the concept of ideal rider, or rather the best driver capable of employing the vehicle at its maximum potential in every situation.
Different other authors worked on these kind of optimization applied to vehicles in the last ten years employing other optimal control problem simulation packages in [4], [5], [6], [7].
The Optimal Maneuver Method is a tool developed expressly for vehicle dynamics and provides for minimum time simulations of a vehicle, subject to some physical limitations (e.g. boundaries of the track, maximum available power, tire adherence etc.), that has to travel from a starting point to a final one within a whole track or a single curve as fast as possible (Fig.1).
Results of these kind of optimization are the optimal maneuver, in terms of the state variables

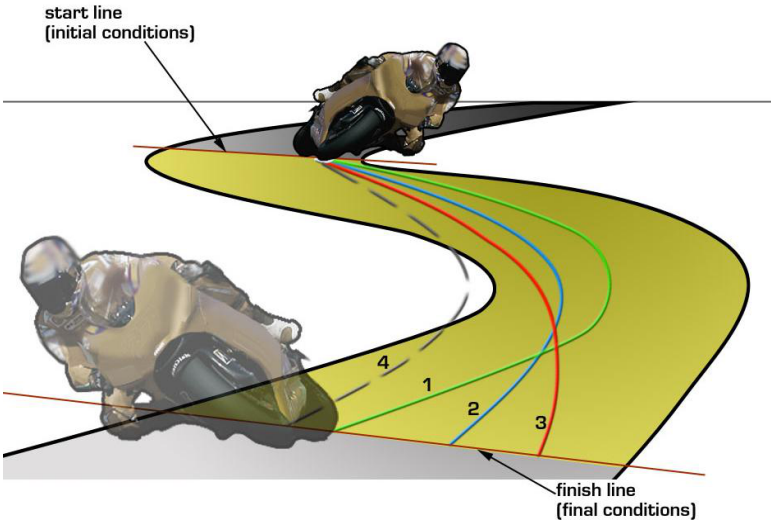

Figure 1: Optimal Maneuver Method approach.

of the systems, including the trajectory of the vehicle on the road, and the history of the input

of the system, thus the commands that must be applied to the vehicle to obtain the optimal maneuver.
Among any possible vehicle, motorcycle represents only one possibility and the pure performance on a whole track as the target to optimize the two-wheeled vehicle is just one of the possible choice in vehicle dynamics research field.
The same approach could be employed with four-wheeled vehicles as well and some of them could require special formulation of their single components to catch details in their dynamics, rather than accurate description of the bodies composing the vehicle itself, leading to large multibody systems (as in the case of motorcycles).
One of the intention here is to underline the advantage of this methodology, that consists of its applicability to different vehicle models for different purposes. These can be the diffusion of the method itself, to do this a simple model that is stable and quick while converging to the solution in every possible simulated scenario is needed. The same vehicle due its stability can be used to develop different formulations of the physical limitations during the simulation or simply to test new functionality for more complex models under development. Other applications are lap-time simulations for particular four-wheeled vehicles as go-kart and formula vehicles that require specific formulations (e.g. rigid drive-line in karts).
Furthermore an ideal driver without any preconceived could be exploit for very specialized maneuver typical of rally cars in order to extrapolate an optimality content from the simulations, trying to reproduce experimental evidence data (Fig.2). Setting different targets for the optimization, thus different optimal strategies, the user can figure out which strategy triggers the desired maneuver.
The large variety of the employable vehicle models could lead to a large number of different

Figure 2: Rally vehicle employed in experimental evidences.

versions of the models themselves due to the different possible formulations of tire-ground interaction forces, suspension forces, aerodynamics etc. Some models could require a detailed definition of the different bodies of the mbs (i.e. multibody system) and their kinematics, while requiring simple linear formulation for tire forces and suspension forces (e.g. racing motorcycles), on the contrary to achieve some specialized car maneuvers the mbs could not need particular attention, whereas a complicated non-linear formulation for tire-ground interaction definition may be needed to complete the study.
For these purpose the idea is to formulate all these components for vehicle dynamics separately from the models themselves, using a general formulation in the models equations for these components and specifying it later on through some external (i.e. linked at a later stage) libraries, communal for the different vehicle models.
The work presented in this thesis covers different aspects: the development of the current

methodology for motorcycles applications in order to improve matching between experimental data and lap-time simulation results, then to formulate different vehicle models including one, two, four wheels for different application purposes. Moreover to create and program libraries to manage components that are communal between the different models mentioned above and that require a particular formulation as explained. Lastly to apply the Optimal Maneuver Method for studying the optimality of some specialized driving techniques that are nowadays under investigation, as aggressive maneuvers outside the linear behavior of tires (i.e. limit handling conditions), which knowledge it is at the base of modern active chassis control systems and could lead to advanced systems with an extended operating envelope.

Chapter 1

Optimal Control and Dynamic Optimization

In the last years Optimal Control Problem simulations (also called Dynamic Optimization) have been considered by different both research and industrial group with the purpose of exploiting them in the "motion planning" for a large variety of applications. Now, even if the theory has been widely clarified and explored, their application to real problems is still cumbersome for the complexity and the dimensions of the system of equation that defined the problem.
The importance of this methodology is related to the fact that it is more accurate with respect to RMPA (i.e. Randomized Motion Planning Algorithms) that are employed for large dimension systems because of their capability of quickly exploring different possibilities of motion. Path trees are identified to be used in the whole configuration space by the integration of the motion equations between two nodes of the path itself.
For this kind of approach the optimality of a particular solution is only probabilistic and not all the possible solutions are considered.
Optimal Control Problems with their particular formulation, include the concept of optimality within a perfomance index and the optimal solution is find out between all the possible ones that verify both equations of motion and constraints.
Two groups of methods are basically employed to solve this kind of problems: "direct" and "indirect" methods.
The first method bases on the discretization of the optimal control problem to obtain a NLP (i.e. Non Linear Problem) that is then solved using some widespread numerical schemes, such as IVS (i.e. Initial Value Solver) and SQP (Sequential Quadratic Programming).
The latter (i.e. Indirect method) is based on the necessary solution of optimality derived by the calculus of variation. Indirect methods usually produce a very accurate solution and are quite sensitive to design parameter variations, since they directly solve the equations of first necessary condition.
This means that one has to produce the symbolical expressions of the necessary conditions of optimality. In details, adjoint equations have to be calculated along with their jacobians for the numerical solution of the Two Point Boundary Value Problem (TPBVP). In addition, the number of adjoint equations (also called co-equations) is equal to the original problem dimension, thus the indirect approach at least doubles the problem dimensionality.
For both these methods is important to find the solution of the TPBVP (i.e. Two Point Boundary Value Problem) in a fast way.
There are basically three main numerical schemes to solve the problems: single-shooting which

are quite sensitive to guess solution, multiple-shooting in which the domain is divided in smaller sub-intervals reducing sensitivity to guessed values, and discretization methods that are considered the most stable and for which the solution is simultaneously obtained for the whole domain.
In this chapter the theory of dynamic optimization extracted from [8] is presented starting from the basis and adding more terms and equations throughout the description, in order to explore different cases and approaches.
Afterwards the approach used in the Optimal Maneuver Method methodology is presented.
First discrete systems are considered to focus on the problem and same approaches are applied to continuous systems afterwards.

1.1 Discrete Dynamic Systems

Given a discrete dynamic system, described by an $n-$dimensional state vector $\mathbf{x}(i)$ at the step i, a control vector $\mathbf{u}(i)$ has to be found for the transition of the system to the state $\mathbf{x}(i+1)$ through:

$$\mathbf{x}(i+1) = f[\mathbf{x}(i), \mathbf{u}(i), i] \tag{1.1}$$

where:

$$\mathbf{x}(0) = x0 \tag{1.2}$$

The problem is to find the sequence of control vector $\mathbf{u}(i)$ for $i = 0, ..., N-1$ to minimize a performance index in the general form:

$$J = \phi[\mathbf{x}(N)] + \sum_{i=0}^{N-1} L[\mathbf{x}(i), \mathbf{u}(i), i] \tag{1.3}$$

subject to the equality constraints Eq.(1.1) and Eq.(1.2) with N, $x0$, f specified. Constraints (1.1) and (1.2) are then adjoint to the performance index (1.3) through the use of Lagrange multiplier vector $\boldsymbol{\lambda}(i)$:

$$\begin{aligned} \bar{J} =& \phi[\mathbf{x}(N)] + \sum_{i=0}^{N-1} \Big\{ L(i) + \boldsymbol{\lambda}^T(i+1)[f(i) - \mathbf{x}(i+1)] \Big\} \\ &+ \boldsymbol{\lambda}^T(0)[x_0 - \mathbf{x}(0)] \end{aligned} \tag{1.4}$$

which can be rewritten as

$$\bar{J} = \phi[\mathbf{x}(N)] - \boldsymbol{\lambda}^T(N)\mathbf{x}(N) + \boldsymbol{\lambda}^T(0)x_0 + \sum_{i=0}^{N-1} [H(i) - \boldsymbol{\lambda}^T(i)\mathbf{x}(i)] \tag{1.5}$$

when defining the Hamiltonian H as

$$H(i) = L(i) + \boldsymbol{\lambda}^T(i+1)f(i) \tag{1.6}$$

The necessary condition for a stationary solution for arbitrary $d\mathbf{u}(i)$ can be reduced to solve $d\bar{J} = 0$:

$$\begin{aligned} d\bar{J} =& [\boldsymbol{\phi}_x - \boldsymbol{\lambda}^T(N)]d\mathbf{x}(N) + \boldsymbol{\lambda}^T(0)d\mathbf{x}_0 \\ &+ \sum_{i=0}^{N-1} \Big\{ [\mathbf{H}_x(i) - \boldsymbol{\lambda}^T(i)]d\mathbf{x}(i) + \mathbf{H}_u(i)d\mathbf{u}(i) \Big\} = 0 \end{aligned} \tag{1.7}$$

where $\boldsymbol{\phi}_x$ is the gradient of ϕ with respect to x, while $\mathbf{H}_x$ and $\mathbf{H}_u$ are the gradient of H with respect to x and u respectively.
Solving the Eq.(1.7) corresponds to the solution of the following set of equations, when recalling that the initial conditions are constant and therefore $d\mathbf{x}_0 = 0$:

$$\boldsymbol{\phi}_x - \boldsymbol{\lambda}^T(N) = 0 \tag{1.8}$$

$$\mathbf{H}_x(i) - \boldsymbol{\lambda}^T(i) = 0, i = 0..N-1 \tag{1.9}$$

$$\mathbf{H}_u(i) = 0, i = 0..N-1 \tag{1.10}$$

Summarizing, the optimal solution is found by solving the Two Point Boundary Value Problem (TPBVP) defined by the model equations Eq.(1.1), co-equations Eq.(1.9), optimality equations Eq.(1.10), initial conditions Eq.(1.2) (first point of the TPBVP) and final conditions Eq.(1.8) (second point of the TPBVP).
Vectors $\mathbf{x}(i)$ and $\boldsymbol{\lambda}(i)$ have both dimension n, $\mathbf{u}(i)$ has dimension m, $i = 0, ..., N-1$ so the problem has $N(2n+m)$ unknowns and as many equations.

1.1.1 Terminal Constraints

Terminal constraints can be added to specify the final value of (some components of) $\mathbf{x}(N)$ in the form:

$$\psi[\mathbf{x}(N)] = 0 \tag{1.11}$$

As a consequence the performance index $\bar{J}$ in Eq.(1.5) is updated to include an additional term $\boldsymbol{\nu}^T\psi[\mathbf{x}(N)]$ (where $\boldsymbol{\nu}$ is the related Lagrange multiplier). When deriving $d\bar{J}$ the only difference is a new term $\boldsymbol{\nu}^T\boldsymbol{\psi}_x$ into the first bracket. Therefore Eq.(1.8) is updated to:

$$\boldsymbol{\phi}_x + \boldsymbol{\nu}^T\boldsymbol{\psi}_x - \boldsymbol{\lambda}^T(N) = 0 \tag{1.12}$$

Summarizing, when solving the optimal control problem with terminal conditions, the equations of the TPBVP to solve are Eq.(1.1), Eq.(1.9), Eq.(1.10), Eq.(1.2) (first point of the TPBVP) and final conditions Eq.(1.12) (second point of the TPBVP).

1.1.2 Open Final Time

The minimization of the final time can also be included in the formulation as follows.
The cost that has to be minimized becomes:

$$J = \phi[\mathbf{x}(N), t_f] + \sum_{i=0}^{N-1} L[\mathbf{x}(i), \mathbf{u}(i), i] \tag{1.13}$$

where $t_f = N\Delta$ and subject to the costraints:

$$\mathbf{x}(i+1) = f[\mathbf{x}(i), \mathbf{u}(i), i, \Delta] \ , \ \mathbf{x}(0) = x_0 \tag{1.14}$$

and

$$0 = \psi[\mathbf{x}(N), t_f] \tag{1.15}$$

For minimum time problems $\phi = t_f$.
Defining $H(i)$ and Φ as follows:

$$H(i) = L(i) + \boldsymbol{\lambda}^T(i+1) f[\mathbf{x}(i), \mathbf{u}(i), i, \Delta] \tag{1.16}$$

$$\Phi = \phi + \boldsymbol{\nu}^T \psi \tag{1.17}$$

Following the previous procedure the only additional necessary condition for a stationary solution is:

$$0 = \mathbf{\Phi}_\Delta + \sum_{i=0}^{N-1} \mathbf{H}_\Delta(i) \tag{1.18}$$

That determines the optimal time step Δ.

1.2 Continuous Dynamic Systems

Given a continuous dynamic system, described by an $n-$dimensional state vector $\mathbf{x}(t)$, a control vector $\mathbf{u}(t)$ has to be found for the transition of the system through the time:

$$\dot{\mathbf{x}} = f[\mathbf{x}(t), \mathbf{u}(t), t] \tag{1.19}$$

where:

$$\mathbf{x}(t_0) = x0 \tag{1.20}$$

The problem is to find the sequence of control vector $\mathbf{u}(t)$ for $t_0 \leq t \leq t_f$ to minimize a performance index in the general form:

$$J = \phi[\mathbf{x}(t_f)] + \int_{t_0}^{t_f} L[\mathbf{x}(t), \mathbf{u}(t), t] \tag{1.21}$$

subject to the equality constraints Eq.(1.19) and Eq.(1.20) with $x0$ specified. Constraints (1.19) and (1.20) are then adjoint to the performance index (1.21) through the use of Lagrange multiplier vector $\boldsymbol{\lambda}(t)$:

$$\bar{J} = \phi + \int_{t_0}^{t_f} \Big\{ L[\mathbf{x}(t), \mathbf{u}(t), t] + \boldsymbol{\lambda}^T(t)[f[\mathbf{x}(t), \mathbf{u}(t), t] - \dot{\mathbf{x}} \Big\} dt \tag{1.22}$$

which can be rewritten as

$$\bar{J} = \phi - \boldsymbol{\lambda}^T(t_f)\mathbf{x}(t_f) + \int_{t_0}^{t_f} [H(t) + \dot{\boldsymbol{\lambda}}^T(t)\mathbf{x}(t)]dt + \boldsymbol{\lambda}^T(t_0)x_0 \tag{1.23}$$

when defining the Hamiltonian H as

$$H(t) = L(t) + \boldsymbol{\lambda}^T(t) f[\mathbf{x}(t), \mathbf{u}(t), t] \tag{1.24}$$

The necessary condition for a stationary solution for arbitrary $d\mathbf{u}(t)$ can be reduced to solve $d\bar{J} = 0$:

$$\begin{aligned} d\bar{J} =& [\boldsymbol{\phi}_x - \boldsymbol{\lambda}^T(t_f)]d\mathbf{x}(t_f) + \boldsymbol{\lambda}^T(t_0)d\mathbf{x}_0 \\ &+ \int_{t_0}^{t_f} \Big\{ [\mathbf{H}_x(t) + \dot{\boldsymbol{\lambda}}^T]\delta x + \mathbf{H}_u(t)\delta u \Big\} dt = 0 \end{aligned} \tag{1.25}$$

where $\boldsymbol{\phi}_x$ is the gradient of ϕ with respect to x, while $\mathbf{H}_x$ and $\mathbf{H}_u$ are the gradient of H with respect to x and u respectively.
Solving the Eq.(1.25) corresponds to the solution of the following set of equations, when recalling that the initial conditions are constant and therefore $dx_0 = 0$:

$$\boldsymbol{\phi}_x - \boldsymbol{\lambda}^T(t_f) = 0 \tag{1.26}$$

$$\mathbf{H}_x(t) + \dot{\boldsymbol{\lambda}}^T = 0 \tag{1.27}$$

$$\mathbf{H}_u(t) = 0 \tag{1.28}$$

Summarizing, the optimal solution is found by solving the Two Point Boundary Value Problem (TPBVP) defined by the model equations Eq.(1.19), co-equations Eq.(1.27), optimality equations Eq.(1.28), initial conditions Eq.(1.20) (first point of the TPBVP) and final conditions Eq.(1.26) (second point of the TPBVP).
Terminal constraints can be added to specify the final value of (some components of) $\mathbf{x}(t_f)$ in the form:

$$\psi[\mathbf{x}(t_f)] = 0 \tag{1.29}$$

As a consequence the performance index $\bar{J}$ in Eq.(1.23) is updated to include an additional term $\boldsymbol{\nu}^T\psi[\mathbf{x}(t_f)]$ (where $\boldsymbol{\nu}$ is the related Lagrange multiplier). When deriving $d\bar{J}$ the only difference is a new term $\boldsymbol{\nu}^T\boldsymbol{\psi}_x$ into the first bracket. Therefore Eq.(1.26) is updated to:

$$\boldsymbol{\phi}_x + \boldsymbol{\nu}^T\boldsymbol{\psi}_x - \boldsymbol{\lambda}^T(t_f) = 0 \tag{1.30}$$

Summarizing, when solving the optimal control problem with terminal conditions, the equations of the TPBVP to solve are Eq.(1.19), Eq.(1.27), Eq.(1.28), Eq.(1.20) (first point of the TPBVP) and final conditions Eq.(1.30) (second point of the TPBVP).

1.2.1 Open Final Time and Terminal Constraints

If a continuous dynamic system is now considered the problem is formulated as finding the control vector $\mathbf{u}(t)$ for $t_0 \leq t \leq t_f$ and final time t_f to minimize

$$J = \phi[\mathbf{x}(t_f), t_f] + \int_{t_0}^{t_f} L[\mathbf{x}(t), \mathbf{u}(t), t] \tag{1.31}$$

in which for minimum time problems $\phi = t_f$ and subject to the constraints

$$\dot{\mathbf{x}} = f(\mathbf{x}, \mathbf{u}, t) \ , \ \mathbf{x}(t_0) = x_0 \tag{1.32}$$

$$0 = \psi[\mathbf{x}(t_f), t_f] \tag{1.33}$$

Adjoining the constraints (1.32) and (1.33) to the perfomance index (1.31) through Lagrange multipliers leads to:

$$\bar{J} = \phi + \boldsymbol{\nu}^T \psi + \int_{t_0}^{t_f} \Big\{ L[\mathbf{x}(t), \mathbf{u}(t), t] + \boldsymbol{\lambda}^T(t) \Big[f[\mathbf{x}(t), \mathbf{u}(t), t] - \dot{\mathbf{x}} \Big] \Big\} dt \tag{1.34}$$

Defining $H(t)$ and Φ as follows:

$$H(t) = L(t) + \boldsymbol{\lambda}^T(t) f[\mathbf{x}(t), \mathbf{u}(t), t] \tag{1.35}$$

$$\Phi = \phi + \boldsymbol{\nu}^T \psi \tag{1.36}$$

Now considering differential changes in $\bar{J}$ due to the variations of $\mathbf{u}(t)$ and a differential change in t_f

$$\begin{aligned} d\bar{J} =& [\boldsymbol{\Phi}_x - \boldsymbol{\lambda}^T(t_f)] d\mathbf{x}(t_f) + \dot{\Phi} dt_f + \boldsymbol{\lambda}^T(t_0) d\mathbf{x}_0 \\ &+ \int_{t_0}^{t_f} \Big\{ [\mathbf{H}_x(t) + \dot{\boldsymbol{\lambda}}^T] \delta x + \mathbf{H}_u(t) \delta u \Big\} dt = 0 \end{aligned} \tag{1.37}$$

Assuming that $\dot{\Phi} = \boldsymbol{\Phi}_{t_f} + \boldsymbol{\Phi}_x \dot{\mathbf{x}}(t_f)$, and choosing proper Lagrange multipliers $\boldsymbol{\lambda}(t)$:

$$\mathbf{H}_x(t) + \dot{\boldsymbol{\lambda}}^T = 0 \tag{1.38}$$

$$\boldsymbol{\phi}_x + \boldsymbol{\nu}^T \boldsymbol{\psi}_x - \boldsymbol{\lambda}^T(t_f) = 0 \tag{1.39}$$

The condition for a stationary solution becomes:

$$d\bar{J} = \dot{\phi} \ dt_f + \int_{t_0}^{t_f} \mathbf{H}_u \delta u \ dt = 0 \tag{1.40}$$

for arbitrary $\delta u(t)$ and dt_f and so:

$$\mathbf{H}_u(t) = 0 \ , \ t_0 \leq t \leq t_f \tag{1.41}$$

$$\Phi = 0 \tag{1.42}$$

$\boldsymbol{\nu}$ must be found so that $\psi = 0$. Eq.(1.42) is the so-called transversality condition that determines the optimal final time t_f. $\dot{\Phi}$ is the total time derivative of Φ:

$$\dot{\Phi} = \boldsymbol{\Phi}_{t_f} + \boldsymbol{\Phi}_x \dot{\mathbf{x}}(t_f) = 0 \tag{1.43}$$

where Φ has been defined by Eq.(1.36).

1.3 Optimal Maneuver Method theoretical approach: dynamic optimization for continuous systems

Starting from the theory presented in the previous chapter Optimal Maneuver Method approach is delimited herein and some concepts are resumed. Optimal control aims at minimizing a certain cost function subject to a certain number of equality and/or inequality constraints [8]. In more detail, given a continuous dynamic system

$$\dot{\mathbf{x}} = \mathbf{f}[\mathbf{x}(t), \mathbf{u}(t)] \tag{1.44}$$

with initial conditions:

$$\mathbf{x}(t_0) = \mathbf{x}_0 \tag{1.45}$$

the problem is to find the sequence of control vector $\mathbf{u}$ to minimize a certain performance index:

$$J = \phi[\mathbf{x}(t_f)] + \int_{t_0}^{t_f} L[\mathbf{x}(t), \mathbf{u}(t)] \tag{1.46}$$

subject to the equality constraints Eq.(1.44) and Eq.(1.45). The constraints (1.44) and (1.45) are then adjoint to the performance index (1.46) through the use of Lagrange multipliers $\boldsymbol{\lambda}$:

$$\bar{J} = \phi + \int_{t_0}^{t_f} \Big\{ L[\mathbf{x}(t), \mathbf{u}(t)] + \boldsymbol{\lambda}^T(t) \Big[\mathbf{f}[\mathbf{x}(t), \mathbf{u}(t)] - \dot{\mathbf{x}} \Big] \Big\} dt \tag{1.47}$$

Defining the Hamiltonian H as:

$$H(t) = L(t) + \boldsymbol{\lambda}^T(t) \mathbf{f}[\mathbf{x}(t), \mathbf{u}(t)] \tag{1.48}$$

Eq.(1.47) can be rewritten as:

$$\bar{J} = \phi + \int_{t_0}^{t_f} [H(t) - \boldsymbol{\lambda}^T(t) \dot{\mathbf{x}}] dt \tag{1.49}$$

that correspond to :

$$\bar{J} = \phi + \int_{t_0}^{t_f} H(t) dt - \int_{t_0}^{t_f} \boldsymbol{\lambda}^T(t) \dot{\mathbf{x}} dt \tag{1.50}$$

Now integrating by parts the second integral:

$$\bar{J} = \phi + \int_{t_0}^{t_f} H(t)dt - \Big\{ \Big[\boldsymbol{\lambda}^T(t)\mathbf{x}(t)\Big]_{t_0}^{t_f} - \int_{t_0}^{t_f} \dot{\boldsymbol{\lambda}}^T(t)\mathbf{x}(t)dt \Big\} \tag{1.51}$$

and thus:

$$\bar{J} = \phi - \boldsymbol{\lambda}^T(t_f)\mathbf{x}(t_f) + \int_{t_0}^{t_f} [H(t) + \dot{\boldsymbol{\lambda}}^T(t)\mathbf{x}(t)]dt + \boldsymbol{\lambda}^T(t_0)\mathbf{x}_0 \tag{1.52}$$

The necessary condition for a stationary solution for arbitrary δu is reduced to solve $d\bar{J} = 0$:

$$\begin{aligned} d\bar{J} =& [\boldsymbol{\phi}_x - \boldsymbol{\lambda}^T(t_f)]d\mathbf{x}(t_f) + \boldsymbol{\lambda}^T(t_0)d\mathbf{x}_0 \\ &+ \int_{t_0}^{t_f} \Big\{ [\mathbf{H}_x(t) + \dot{\boldsymbol{\lambda}}^T]\delta\mathbf{x} + \mathbf{H}_u(t)\delta\mathbf{u} \Big\} dt = 0 \end{aligned} \tag{1.53}$$

where $\boldsymbol{\phi}_x$ is the gradient of ϕ with respect to x, while $\mathbf{H}_x$ and $\mathbf{H}_u$ are the gradient of H with respect to $\mathbf{x}$ and $\mathbf{u}$ respectively.
Solving the Eq.(1.53) corresponds to the solution of the following set of equations:

$$\boldsymbol{\phi}_x - \boldsymbol{\lambda}^T(t_f) = 0 \tag{1.54}$$

$$\boldsymbol{\lambda}^T(t_0) = 0 \tag{1.55}$$

$$\mathbf{H}_x + \dot{\boldsymbol{\lambda}}^T = 0 \tag{1.56}$$

$$\mathbf{H}_u = 0 \tag{1.57}$$

Note that the number of Eq.(1.55) corresponds to the number of initial conditions left free in Eq.(1.45). In other words, if all initial conditions are set Eq.(1.55) is not used, while if all initial conditions are left free Eq.(1.55) has the size of the model state vector $\mathbf{x}$.
Terminal constraints, e.g. to specify the final value of some components of $\mathbf{x}(t_f)$, can be added in the form:

$$\boldsymbol{\psi}[\mathbf{x}(t_f)] = 0 \tag{1.58}$$

As a consequence the performance index $\bar{J}$ in Eq.(1.52) is updated to include an additional term $\boldsymbol{\nu}^T\boldsymbol{\psi}$ (where $\boldsymbol{\nu}$ is the related Lagrange multiplier). When deriving $d\bar{J}$ the only difference is a new term $\boldsymbol{\nu}^T\boldsymbol{\psi}_x$ into the first bracket. Therefore Eq.(1.54) is updated to:

$$\boldsymbol{\phi}_x + \boldsymbol{\nu}^T\boldsymbol{\psi}_x - \boldsymbol{\lambda}^T(t_f) = 0 \tag{1.59}$$

Summarizing, the optimal solution is found by solving the Two Point Boundary Value Problem (TPBVP) defined by the model equations Eq.(1.44), free initial states equations Eq.(1.55), co-equations Eq.(1.56), optimality equations Eq.(1.57), initial conditions Eq.(1.45) (first point of the TPBVP) and final conditions Eq.(1.59) (second point of the TPBVP).
Additional inequality constraints (e.g. those on inputs and those to account for physical limitations during the simulation) are added into the performance index J Eq.(1.47) using penalty functions (soft constraints strategy), thus not changing the problem formulation described.
These are functions that assume high values, penalizing the performance index while inequality constraints are violated or at least when they are very closed to zero.
Basically a sum of penalty functions is included in the performance index in Eq.(1.46).

$$J = \phi[\mathbf{x}(t_f)] + \int_{t_0}^{t_f} L[\mathbf{x}(t), \mathbf{u}(t)] + \sum_{i=1}^{q} p_i[d_i(\mathbf{x}(t), \mathbf{u}(t))] \tag{1.60}$$

where p_i are penalty functions and $d_i(\mathbf{x}(t), \mathbf{u}(t))$ are equations that has to be penalized by means of p_i.
Different shapes of these p functions are possible: once the user has selected the desired function its features are basically settable through a couple of parameters (i.e. h and ϵ) to adjust the shape of the function itself (Fig.1.1).

As an example a typical penalty function employed in bandwidth limitation for control variables: the Quadratic function is reported in herein. From Fig.1.2 it turns out how to allow

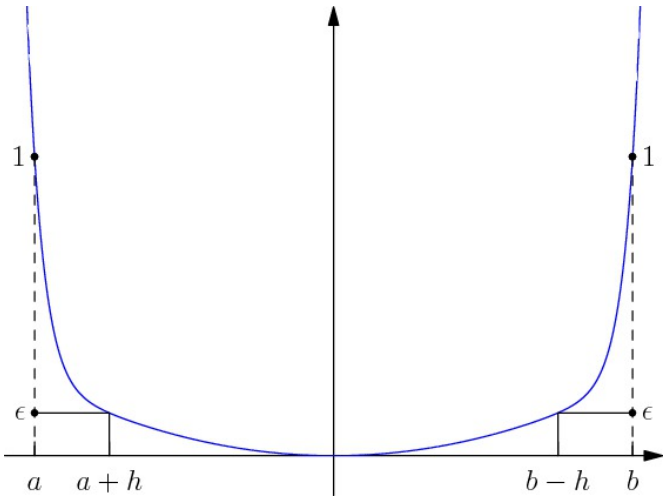

Figure 1.1: General penalty function setup for limitation in control bandwidth.

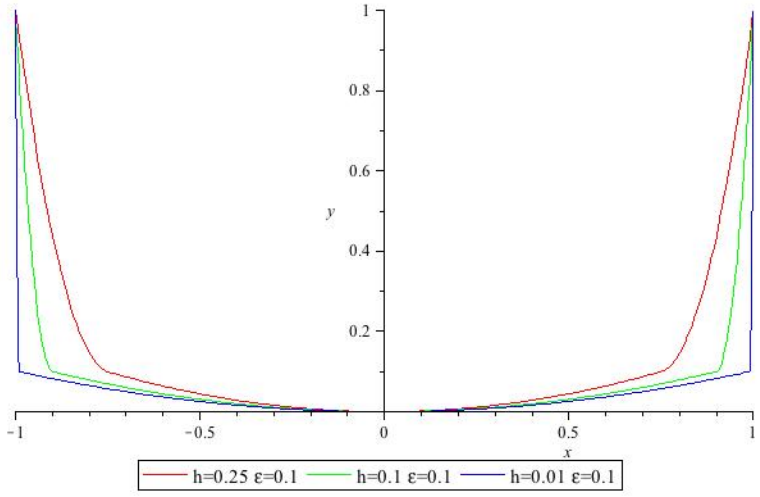

Figure 1.2: Diagram for Quadratic control penalty for different values of the parameter h.

values closer to the imposed limit the user have to set a lower h parameter. Fig.1.3 shows how to adjust the penalty behavior in order to grow its influence for values far from the limit through the parameter ϵ: lower is ϵ lower is penalty influence between the two (i.e. positive and negative) values in which the function start assuming high values (set by h parameter).

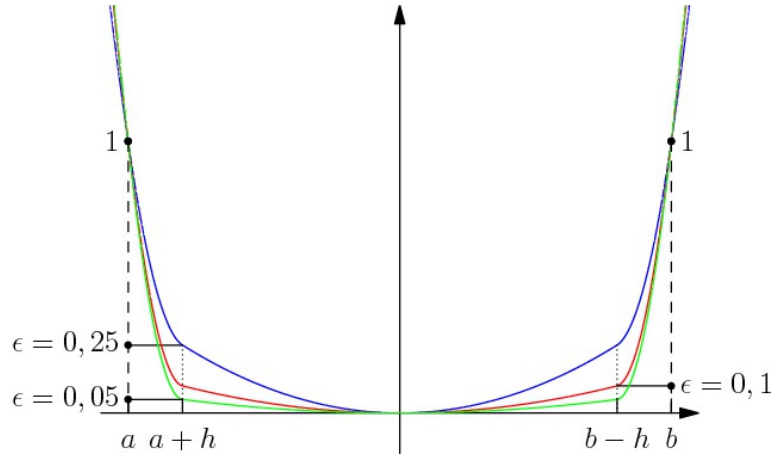

Figure 1.3: Diagram for Quadratic control penalty for different values of the parameter ϵ.

The resulting algebraic-differential system is discretized in order to obtain a finite dimensional algebraic problem. The simulation interval is splitted into N intervals. The resulting system can be solved using a solver for nonlinear algebraic equations. Concerning the perfomance index, it has been shown in section 1.2 that two possibilities can be investigated: open or fixed final time. In the former case (i.e. free time) a minimum time problem is solved: this means to find the motion of a vehicle than travel between two assigned points in the minimum time and satisfies all the constraints.
This approach has not been applied in the Optimal Maneuver Method formulation and the reason is that, as shown in section 1.2.1, additional states and equations are required (i.e. $\phi = t_f$ and transversality equation 1.42).
If time t_f is considered fixed, the specific problem for vehicle cases is formulated as maximizing the average speed and travel distance. Practically instead of minimizing the time for covering fixed distance, the idea is to maximize the travel distance within a fixed amount time. The Lagrange term of the cost function is basically expressed as:

$$L[\mathbf{x}, \mathbf{u}] = -\frac{\dot{s_s}}{V_0} \tag{1.61}$$

where s_s is the curvilinear coordinate measured in the middle lane of the road and V_0 is the scaling factor.
In fact the minimization of the integral $\int_{t_0}^{t_f} \Big(- \frac{\dot{s_s}(t)}{V_0} \Big) dt$ corresponds to maximize the final distance $s_s(t)$.
Starting from these considerations a change of the independent variable t become necessary. The reason of that is the necessity of performing an optimization on a fixed length of track or maneuver. The new independent variable becomes s_s, thus the curvilinear abscissa along the middle lane of the considered track or curve.
In this way for a fixed final s_s (i.e the length of the circuit) the average speed along the middle lane is maximized and the solution corresponds on on a minimum lap-time like solution.
In this methodology the problem is solved using an indirect method approach. In practice, the constrained problem defined above is transformed into a unconstrained problem, by means of Lagrange multipliers and penalty functions. From the first variation of the unconstrained problem a Boundary Value Problem (BVP) is obtained, and the finite difference discretization yields to a large nonlinear system. Full details on the solver are reported in [9].

1.3.1 Road description for the Optimal Maneuver Method

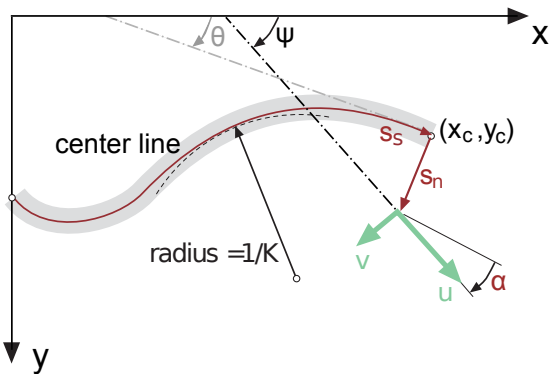

Figure 1.4: Transformation between cartesian and curvilinear coordinates explanation.

It is fundamental to track the vehicle position on the road during the maneuver. In the Optimal Maneuver Method formulation the standard cartesian coordinates are substituted by three curvilinear coordinates: the position of the vehicle along the road s_s, the lateral position perpendicular to the road centre line s_n, and the angle α of the vehicle with respect to the tangent to the road center line, Fig. 1.4. The related equations are:

$$\dot{s}_s = \frac{V\cos(\alpha+\beta)}{1-s_nK} \tag{1.62}$$

$$\dot{s}_n = V\sin(\alpha+\beta) \tag{1.63}$$

$$\dot{\alpha} = \Omega - K\frac{V\cos(\alpha+\beta)}{1-s_nK} \tag{1.64}$$

where K is the local curvature of the road.
Futhermore the road is described by a parametric curve that includes the middle lane and its direction, namely:

$x_c(s_s)$ $\rightarrow$ abscissa of the middle lane point,
$y_c(s_s)$ $\rightarrow$ ordinate of the middle lane point,
$\theta(s_s)$ $\rightarrow$ tangent to the middle lane in the (x_c, y_c) point.

These quantities can be obtained by the following differentiations:

$$\frac{\delta x_c(s_s)}{\delta s_s} = \cos(\theta(s_s)) \tag{1.65}$$

$$\frac{\delta y_c(s_s)}{\delta s_s} = \sin(\theta(s_s)) \tag{1.66}$$

$$\frac{\theta(s_s)}{\delta s_s} = K(s_s) \tag{1.67}$$

The choice of curvilinear coordinates rather than cartesian description make it easier to formulate initial and final conditions relative to the lane and to define trajectory constraints to keep the vehicle within the road.

For example if $\frac{l}{2}$ is the semi-width of the road: the constraints on allowed lateral displacement can be simply formulated as:

$$-\frac{l}{2} \leq s_n \leq \frac{l}{2} \tag{1.68}$$

Finally the transformation between curvilinear coordinates and cartesian coordinates is expressed by the following equations:

$$x = x_c(s_s) - s_n \sin(\theta(s_s)) \tag{1.69}$$

$$y = y_c(s_s) + s_n \cos(\theta(s_s)) \tag{1.70}$$

$$\psi = \theta(s_s) - \alpha \tag{1.71}$$

where (x, y) are cartesian coordinates of the vehicle in the absolute frame and ψ is the absolute yaw angle of the vehicle.

Chapter 2

System components for two-wheeled and four-wheeled vehicle models

The Optimal Maneuver Method is applied to vehicle models that are extremely different from each other: one-wheeled, two-wheeled, three-wheeled, four-wheeled vehicle have been simulated in recent years. Although the different complexity of the models, there are some parts of them that can be shared, and it may be helpful to shift these functionality from the mathematical formulation of a single model to an external flexible tool that can be easily linked to the different models at a later stage.
In this way the development of the model can be fractionated, some part can be simply linked without any possibilities of errors and in more confidential way (i.e. the sources files are cripted). The developer can decide to hide the definition of some parts of the model and release only some libraries.
Among the different components communal for wheeled vehicles modeling two of them: suspension system and tire-ground interaction have been chosen to be part of the first release of these libraries.

2.1 Suspension Forces

2.1.1 Parametric model

Different suspension forces definitions are possible for a vehicle. The total suspension force (or torque if torsion spring-damper system are considered in the modeling as for motorcycle rear suspensions modeling) due to both the spring and the damper elements is introduced in the dynamic model of the vehicle. The part of the force due to the spring can be defined as a linear or non-linear function of the stroke of the suspension, the same for the damper system with respect to the suspension rate. This particular parametric model allows the user to switch through the different possible definitions just varying some parameters.
The suspension force due to the spring element can be defined using a fifth degree polynomial function of the stroke z:

$$F_s = z \rightarrow F_0 + K\, z + c_2\, z^2 + c_3\, z^3 + c_4\, z^4 + c_5\, z^5 \tag{2.1}$$

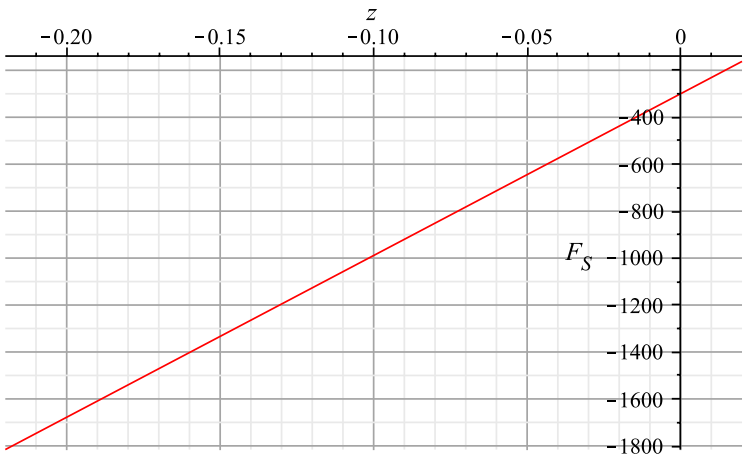

Figure 2.1: Suspension force due to the spring element, linear case.

in which K is the spring stiffness, F_0 is the spring preload and c_i with $i = \{2, 3, 4, 5\}$ are coefficients for the spring force diagram. The user can simply set to zero c_2, c_3, c_4, c_5 coefficients to obtain a simple linear model with preload F_0 (that can be set to zero as well):

$$F_s = z \rightarrow F_0 + K\ z \tag{2.2}$$

The diagram of F_s for the linear case is reported in Fig.(2.1) Another peculiarity regarding the spring force is the possibility of defining a pad that acts both in compression and extension of the suspension to limit the stroke of the suspension itself.
The pad force F_p that it is added to the spring force is defined through the function:

$$\begin{aligned} F_P = (z, \dot{z}, z_{\max}, k_p, z_0) \rightarrow \Big(& P(z, k_p, z_0) \\ & - P(-z - z_{\max}, k_p, z_0) \Big)\ |1 + 10\dot{z}| \end{aligned} \tag{2.3}$$

in which z is the suspension travel (i.e. stroke), $\dot{z}$ is the suspension rate, k_p is the pad stiffness, $z_{\max}$ is the maximum suspension travel and the function P is defined as:

$$P = (x, k_p, x_0) \rightarrow k_p \Big[(x - x0) w\Big(\frac{x - x_0}{x_0} \Big) \frac{x_0}{\pi} \Big] \tag{2.4}$$

the parameters x_0 defines the interface with the pad. The total pad force F_p for different x_0 values is presented in Fig. (2.2): Finally the amount of the suspension force due to the pad and the spring together is represented in Fig.(2.3):
Regarding the damper there is the possibility to set different damping coefficients for bump and rebound conditions, and two different non-linear coefficients can be set as well.
The damping coefficient is defined as follows:

$$c = R(1 + R_{nl}\ \dot{z}) w\Big(\frac{\dot{z}}{v_0} \Big) + C(1 - C_{nl}\ \dot{z}) \Big[1 - w\Big(\frac{\dot{z}}{v_0} \Big) \Big] \tag{2.5}$$

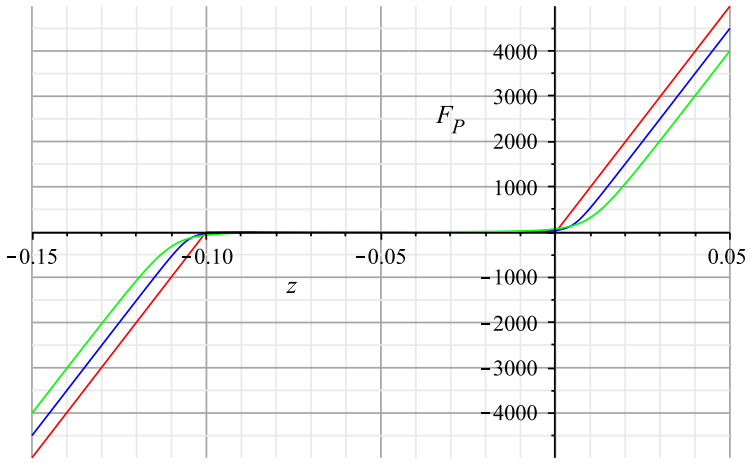

Figure 2.2: Pad element force with respect to the suspension displacement for three different values of the parameter x_0.

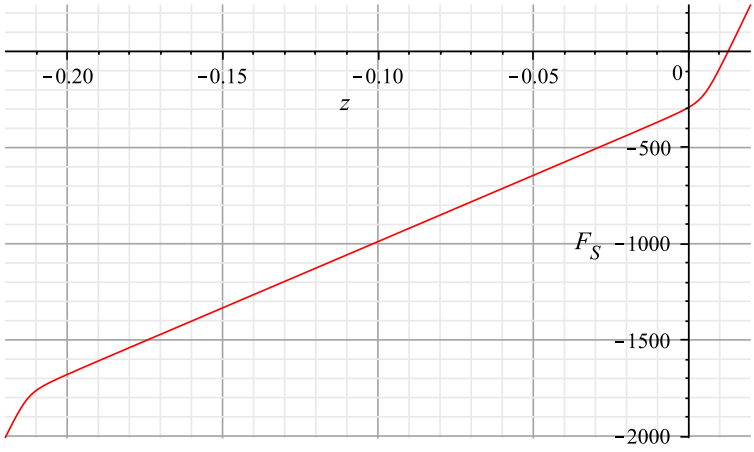

Figure 2.3: Suspension force due to the spring and the pad elements with respect to suspension stroke, linear case.

where R is rebound (i.e. extension) linear damping coefficient, R_{nl} is rebound non-linear damping coefficient, C is bump (i.e. compression) linear damping coefficient, C_{nl} is bump non-linear damping coefficient, v_0 is a working parameter and, the function w and its derivatives are respectively:

$$w = \frac{1}{2} + \frac{\arctan(x)}{\pi} \tag{2.6}$$

$$w' = \frac{1}{\pi(1+x^2)} \tag{2.7}$$

$$w'' = -\frac{2x}{\pi(1+x^2)^2} \tag{2.8}$$

and the diagram for this function is shown in Fig.(2.4). Finally the damping coefficient diagram in condition of non-linearity is reported in Fig.(2.5):
The total damping force is expressed by:

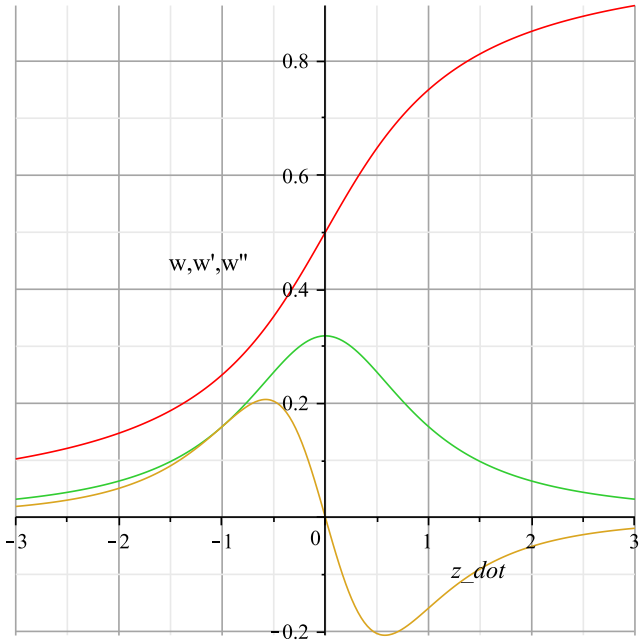

Figure 2.4: w function and its derivatives employed in the damping coefficient formulation.

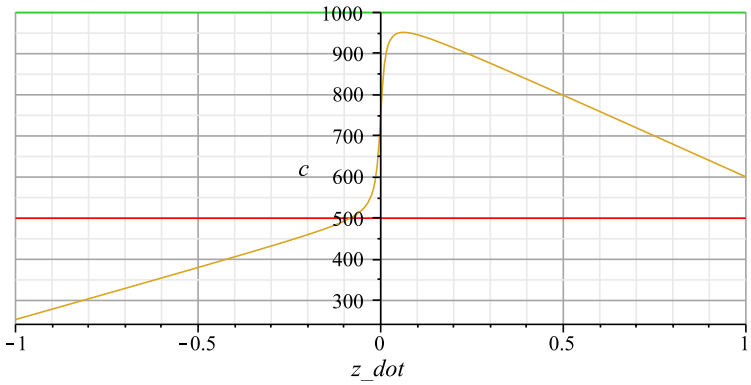

Figure 2.5: Damping coefficient diagram in presence of non linearity. Green and red lines represents rebound and bump linear coefficient values respectively.

$$F_D = \dot{z} \rightarrow c(\dot{z})\dot{z} \tag{2.9}$$

and Fig.(2.6) reports its diagram as a function of $\dot{z}$, the suspension rate.

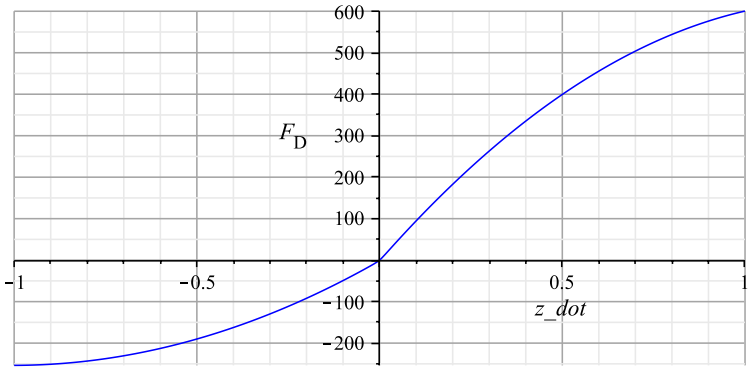

Figure 2.6: Suspension force due to the damper element with respect to suspension rate.

2.1.2 Data file format

As explained above, the user of the Optimal Maneuver Method has to set just a few parameters in order to define its own suspension forces curves. The code below shows that a LUA code structure "rearSuspension" (same for front suspension) is filled by means of a LUA function "suspension". This last can be change by the user to set another suspension model if available (in this case "suspension" corresponds to parametric model).
The function checks whether all the parameters are set, if not it assigns default values to them.

Listing 2.1: suspension LUA function syntax to set model parameters values.

```
rearSuspension = suspension{
  name = "Rear_Suspension",
  comment = "no_comment",
  stroke  =  0.1300    ,        -- Suspenson Travel [m]           -> default: 0.1
  pad_stiffness =  10.0e3,      -- Pad Stiffness [N/m]            -> default: 0.0
  spring = {
    preload   =   0.000 ,       -- Preload[N]                     -> default: 0.0
    stiffness =  10.0e3 ,       -- Stiffness[N/m]
    c2        =   0.000 ,       -- Non-linear stiffness factor    -> default: 0.0
    c3        =   0.000 ,       -- Non-linear stiffness factor    -> default: 0.0
    c4        =   0.000 ,       -- Non-linear stiffness factor    -> default: 0.0
    c5        =   0.000         -- Non-linear stiffness factor    -> default: 0.0
          },
  damper = {
    rebound               =   0.5e3 ,  -- Linear coeff.[Ns/m]
    nonlinear_rebound     =   0.000 ,  -- Non-linear coeff.[Ns/m] -> default: 0.0
    compression           =   0.5e3 ,  -- Linear coeff.[Ns/m]
    nonlinear_compression =   0.000    -- Non-linear coeff.[Ns/m] -> default: 0.0
          },
  pad_theta0 = 0.01,       -- Pad Stiffness Working Parameter     -> default: 0.01
  v0 = 0.05,               -- Working Parameter                   -> default: 0.05
  nil}
```

2.1.3 C++ code

The management of the different models that can be include in the suspension library is developed in C++ language. Different classes are defined as follows:

Suspension: it is a suspension manager, its setup method is capable of reading the type of the suspension model selected by the user. Setup and Forces methods (i.e. C++ functions) used are those of the chosen suspension model.
It contains all methods that are include in the SuspensionBase class.

SuspensionBase: it's basically a generic suspension, all sub-classes (i.e. suspension models) will implement their specific version of SuspensionBase virtual methods in order to employ their own suspension model.
In this class are code skeletons of all the methods including setup and suspensions forces.

SuspensionParametric: it inherits methods from SuspensionBase class and specifies them with its own mathematical definitions.

Setup methods for suspension manager and suspensions models classes are reported herein, whole code for **Suspension** and **SuspensionBase** classes is not shown for brevity.

Listing 2.2: Suspension manager setup method C++ code.

```
/*
  ____                                  _                                  _
 / ___| _   _ ___ _ __   ___ _ __  ___(_) ___  _ __        ___  ___| |_ _   _ _ __
 \___ \| | | / __| |_ \ / _ \ |_ \/ __| |/ _ \| |_ \ _____/ __|/ _ \ __| | | | |_ \
  ___) | |_| \__ \ |_) |  __/ | | \__ \ | (_) | | | |_____\__ \  __/ |_| |_| | |_) |
 |____/ \__,_|___/ .__/ \___|_| |_|___/_|\___/|_| |_|     |___/\___|\__|\__,_| .__/
                 |_|                                                         |_|
*/
  void
  Suspension::setup( MapValues const & vars, MapStrings const & strings ) {

    ofstream SuspensionStiffnessFile ((suspensionName +
                                       "SuspensionStiffnessFile.txt").c_str());
    ofstream SuspensionDamperFile    ((suspensionName +
                                       "SuspensionDamperFile.txt").c_str());
    string suspensionType = getStringWithPrefix( strings, suspensionName, "type");

    if   ( pSuspension   !=  NULL          ) delete pSuspension;
    if   ( suspensionType == "Parametric"  ) pSuspension = new SuspensionParametric;
    else  cerr << "Unknown␣Suspension␣type<" << suspensionType << ">"<< '\n';

    // setup model
    pSuspension -> setup( suspensionName, vars, strings );

    for ( double theta = -0.15 ; theta <= 0.02 ; theta += 0.001 )
      SuspensionStiffnessFile << setw(10) << theta << '\t'
                              << setw(10) << pSuspension->suspensionForce(theta,0)
                              << '\n' ;

    for ( double theta_dot = -1 ; theta_dot <= 1 ; theta_dot += 0.001 )
      SuspensionDamperFile << setw(10) << theta_dot << '\t'
                           << setw(10) << pSuspension->suspensionForce(0,theta_dot)
                           << '\n' ;
    SuspensionStiffnessFile.close();
    SuspensionDamperFile.close();
  }
```

Once the suspension model has been set through **type** variable its own **setup** method is defined. The main setup method produces also two files containing diagrams for spring and damper forces corresponding to the desired model. Parametric case setup method is shown in the following listed code:

Listing 2.3: Parametric suspension model setup C++ code.

```
/*
 ____                                          _          _
|  _ \ __ _ _ __ __ _ _ __ ___   ___| |_ _ __(_) ___
| |_) / _` | |__/ _` | |_ ` _ \ / _ \ __| |__| |/ __|
|  __/ (_| | | | (_| | | | | | |  __/ |_| |  | | (__
|_|   \__,_|_|  \__,_|_| |_| |_|\___|\__|_|  |_|\___|

*/
  void
  SuspensionParametric::setup( string     const & prefix,
                               MapValues  const & vars,
                               MapStrings const & strings ) {
    // Records name and comment in specified variables
    name                 = getStringWithPrefix( strings, prefix, "name" ) ;
    comment              = getStringWithPrefix( strings, prefix, "comment" ) ;
    // Records Kr, Kf in specified variables
    theta_travel         = getValueWithPrefix( vars, prefix, "theta_travel");
    pad_kr               = getValueWithPrefix( vars, prefix, "pad_kr");
    pad_theta0           = getValueWithPrefix( vars, prefix, "pad_theta0");
    preload              = getValueWithPrefix( vars, prefix, "preload");
    stiffness            = getValueWithPrefix( vars, prefix, "stiffness");
    c2                   = getValueWithPrefix( vars, prefix, "c2");
    c3                   = getValueWithPrefix( vars, prefix, "c3");
    c4                   = getValueWithPrefix( vars, prefix, "c4");
    c5                   = getValueWithPrefix( vars, prefix, "c5");
    rebound              = getValueWithPrefix( vars, prefix, "rebound" );
    nonlinear_rebound    = getValueWithPrefix( vars, prefix, "nonlinear_rebound" );
    compression          = getValueWithPrefix( vars, prefix, "compression" );
    nonlinear_compression = getValueWithPrefix( vars, prefix, "nonlinear_compression"
          ) ;
    v0                   = getValueWithPrefix( vars, prefix, "v0" );
  } ;

#include "parametric_suspension_formulas_lib.cc"
```

The last **include** command open another file containing the specific formulation for suspension force and its derivatives.
The user have just to define equations for its model by means of the symbolic algebra software Maple, and then execute a Maple procedure that automatically computes all derivatives for the different arguments of suspension force function and generates C++ file (e.g. parametric_suspension_formulas_lib.cc) that will be include in the libraries.
The power of this methodology is that it is completely automatic once defined model equations.

2.1.4 Maple procedure

The procedure for formulas and derivatives computation of the suspension functions and include file (for methods specification) generation is reported below:

Listing 2.4: Maple procedure for derivatives computation and include file generation.

```
# Print code
CgenerateFunction := proc(suspensionvars,ModelType,force,index1::integer:=0,index2::integer:=0)
  local F:
  printf("valueType %s::%s",ModelType,force):
  F := force(theta,theta_dot):
  if index1 > 0 then F := simplify(diff(F, suspensionvars[index1]),size): printf("_%d",index1): end:
  if index2 > 0 then F := simplify(diff(F, suspensionvars[index2]),size): printf("_%d",index2): end:
  printf("(
        valueType theta,
        valueType theta_dot
        )const
  { valueType f;\n",
  ModelType,"a",index1,index2);
  CodeGeneration[C]([f= F]);
  printf("return(f);
  };\n\n");
end proc:

# Main procedure
CodeGeneration_suspension := proc(susp, ModelType,suspensionvars)
    local suspensionForce:
    suspensionForce := (suspensionvars) -> susp;
    CgenerateFunction(suspensionvars,ModelType,suspensionForce);
    CgenerateFunction(suspensionvars,ModelType,suspensionForce,1);
    CgenerateFunction(suspensionvars,ModelType,suspensionForce,2);
    CgenerateFunction(suspensionvars,ModelType,suspensionForce,1,1);
    CgenerateFunction(suspensionvars,ModelType,suspensionForce,1,2);
    CgenerateFunction(suspensionvars,ModelType,suspensionForce,2,2);

end proc:

# Save maple input file
currentdir("userDir"):
save CgenerateFunction, CodeGeneration_suspension, "CodeGeneration_suspension.mpl":
```

2.2 Tire Horizontal Forces

Another "component" that has been include in these libraries is tire-ground interactions. The tire library includes different mathematical definitions of the horizontal forces (i.e. lateral and longitudinal forces) representing the interactions between tire and ground. Torques (e.g. self-aligning torque) are not considered in these formulation thus the user must add them directly in the model equations if necessary.
An explanation of the models included in the current version of the libraries is presented herein.

2.2.1 Linear model

The simplest model that the user can use for the simulations is the linear one.
The lateral force includes the effect of both side-slip and camber angle and it's defined as follows:

$$F_{lat} = (N, \lambda, \phi, \kappa) \rightarrow (K_\lambda \, \lambda + K_\phi \, \phi) \, N \tag{2.10}$$

where K_λ and K_ϕ are cornering and camber stiffness respectively, λ is the side-slip angle and ϕ is the camber angle of the wheel. N represents the vertical load. In this case κ has no effect on the lateral force. The longitudinal force it's formulated as a function of the longitudinal slip

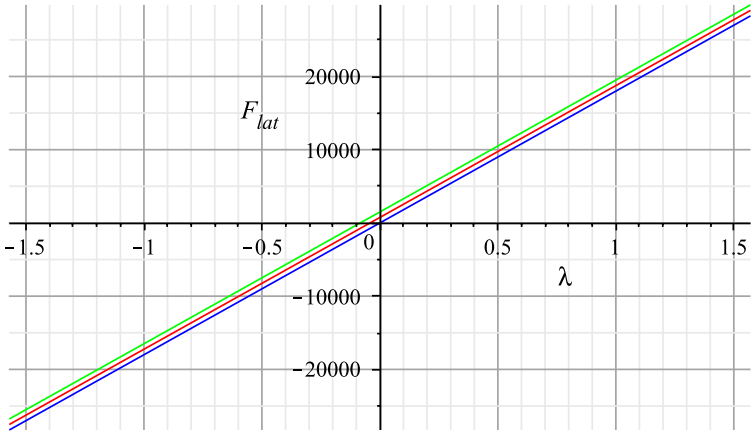

Figure 2.7: Lateral tire force due to the side-slip for three different camber angle configurations.

κ as follows:

$$F_{long} = (N, \lambda, \phi, \kappa) \rightarrow (K_\kappa \, \kappa) \, N \tag{2.11}$$

where K_κ is the longitudinal stiffness and N represents the vertical load. In this other case λ and ϕ have no effect on the longitudinal force.

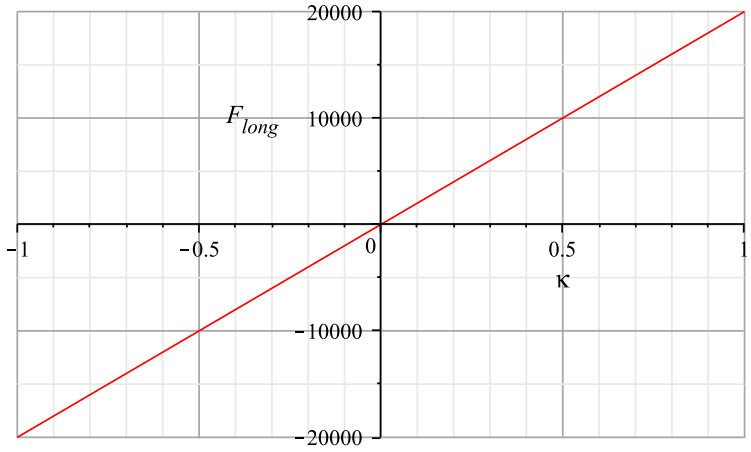

Figure 2.8: Longitudinal tire force due to longitudinal slip.

2.2.2 Pacejka model

Models that have been specifically designed to represent the tire as a vehicle component in vehicle simulations enviroment are called "semi-empirical". The reason is that these models are based on measured data but may also contain structures that find their origin in physical models.
H.B.Pacejka proposed his model based on the "similarity" concept [10]. This library includes two different models that employ this approach, namely: uncoupled and coupled model. Both lateral and longitudinal forces are expressed by the Pacejka "Magic Formula" that in its general form is formulated as:

$$y = D\ \sin\{C\ \arctan[B\ x - E(B\ x - \arctan B\ x)]\} \tag{2.12}$$

with $Y(X) = y(x) + S_V$ that represents the output variable F_{lat} or F_{long} and with $x = X + S_H$ that represent the input variable κ or $\tan(\lambda)$ including the effect of the camber angle ϕ.
The Magic Formula $y(x)$ typically produces a curve that passes through the origin (i.e. $x = y = 0$) and after reaching a maximum tends to a horizontal asymptote. in some conditions (e.g. for non null ϕ) the curve must present an offset with respect to the origin, thus two parameters S_H and S_V are introduced. S_H is the horizontal shift and S_V is the vertical shift. A new set of coordinates $Y(X)$ are defined.
An explanation of this formulation is given by Fig.(2.9).
D is the peak factor and represents the peak value (with respect to the central x-axis and for

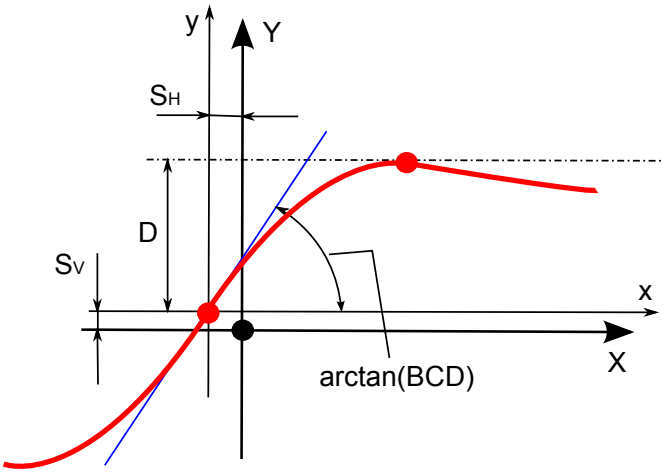

Figure 2.9: Curve produced by Magic Formula and parameters explanation.

$C \geq 1$), the product BCD corresponds to the slope at the origin, the shape factor C determines the shape of the resulting curve (i.e. limits of the range of the sine function in (2.12), B is the stiffness factor and determine the slope at the origin.

Uncoupled forces

This formulation includes pure slip condition, both for lateral and longitudinal forces thus the interactions in the two directions with ground results mutually uncoupled.
In this case the lateral force is expressed by:

$$F_{lat} = (N, \lambda, \phi, \kappa) \rightarrow D_\lambda \ \sin\{C_\lambda \ \arctan[B_\lambda \ \sigma - E_\lambda(B_\lambda \ \sigma - \arctan B_\lambda \ \sigma)]\} \ N \quad (2.13)$$

where $B_\lambda, C_\lambda, D_\lambda, E_\lambda$ are specific coefficients for side-slip force and σ is expressed with a particular function of λ and ϕ (side-slip and camber angles respectively) in order to consider the concurrent presence of these two angles through the equivalent side-slip angle approach:

$$\sigma = \lambda \frac{B_\phi \ C_\phi}{B_\lambda \ C_\lambda} \ \phi \quad (2.14)$$

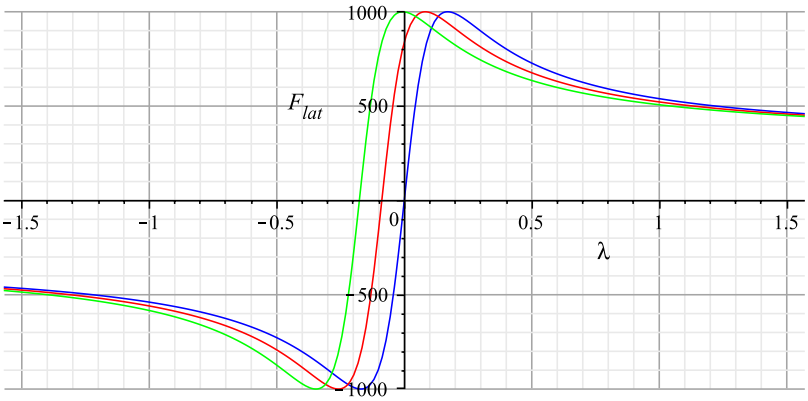

Figure 2.10: Lateral tire force due to the side-slip for three different camber angle configurations.

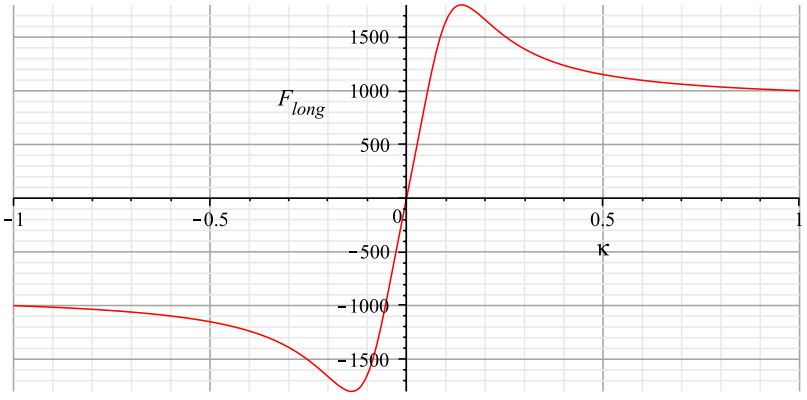

Figure 2.11: Longitudinal tire force due to longitudinal slip.

For the longitudinal interaction the formulation is equivalent to the previous:

$$F_{long} = (N, \lambda, \phi, \kappa) \rightarrow D_\kappa \ \sin\{C_\kappa \ \arctan[B_\kappa \ \kappa - E_\kappa(B_\kappa \ \kappa - \arctan B_\kappa \ \kappa)]\} \ N \quad (2.15)$$

where $B_\kappa, C_\kappa, D_\kappa, E_\kappa$ are specific coefficients for side-slip force and κ is the slip ratio .

Coupled forces

This tire model is the most accurate one that the user can select for Optimal Manoeuvre Method simulations.
It is based on the 'similarity' approach developed by Hans B. Pacejka [10]. The novel of this model is the combination of the longitudinal and the lateral slips that mutually limit both the lateral and the longitudinal forces. First of all the theoretical longitudinal slip (instead of a practical slip) is defined:

$$\sigma_x = \frac{\kappa}{1 + \kappa + \epsilon} \tag{2.16}$$

a small positive quantity ϵ has been added for an artificial limitation of $\sigma_x \to \infty$ when $\kappa \to -1$ the same for the theoretical lateral slip :

$$\sigma_y = \frac{\tan(\lambda^*)}{1 + \kappa} \tag{2.17}$$

where λ^* account for both side-slip and camber effect as follows:

$$\lambda^* = \lambda + \frac{K_\phi}{K_\lambda}\phi \tag{2.18}$$

in which $K_\phi = B_\phi\ C_\phi\ D_\phi$ and $K_\lambda = B_\lambda\ C_\lambda\ D_\lambda$ are camber and cornering stiffness respectively. Now the theoretical equivalent slip is calculated:

$$\sigma_{eq} = \sqrt{\sigma_x^2 + \sigma_y^2 + \epsilon^2} \tag{2.19}$$

Two new stiffness factors can be defined, the longitudinal one:

$$B_X = \sigma_{eq}\ B_\kappa \tag{2.20}$$

and the lateral as follows:

$$B_Y = \sigma_{eq}\ B_\lambda \tag{2.21}$$

Finally the resulting lateral force formula is the following:

$$F_{lat} = (N, \lambda, \phi, \kappa) \to -\frac{\sigma_y}{\sigma_{eq}}\ D_\lambda\ \sin\{C_\lambda\ \arctan[B_Y - E_\lambda(B_\lambda\ \arctan B_Y)]\}\ N \tag{2.22}$$

Fig.(2.12) shows how different values of the positive slip ratio (i.e. driving conditions) influence the lateral force and in particular causes a drastic decrease for high values of the longitudinal slip. The same effect due to the negative values of the slip ratio (i.e. braking conditions) is reported in Fig.(2.13). Moreover can be noticed how the representation in therms of practical slips results to be asymmetric with respect to longitudinal slip quantity. This is the reason for the different shape of the lateral force in different conditions (i.e. driving and braking). regarding the longitudinal force it is defined as:

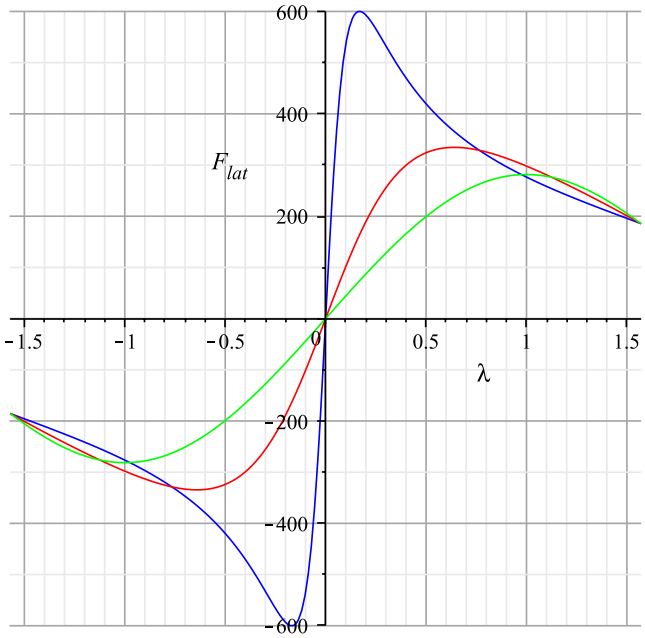

Figure 2.12: Lateral force varying the side-slip angle λ at different slip ratios: driving condition. Blue $= 0$, Red $= 0.5$, Green $= 0.99$.

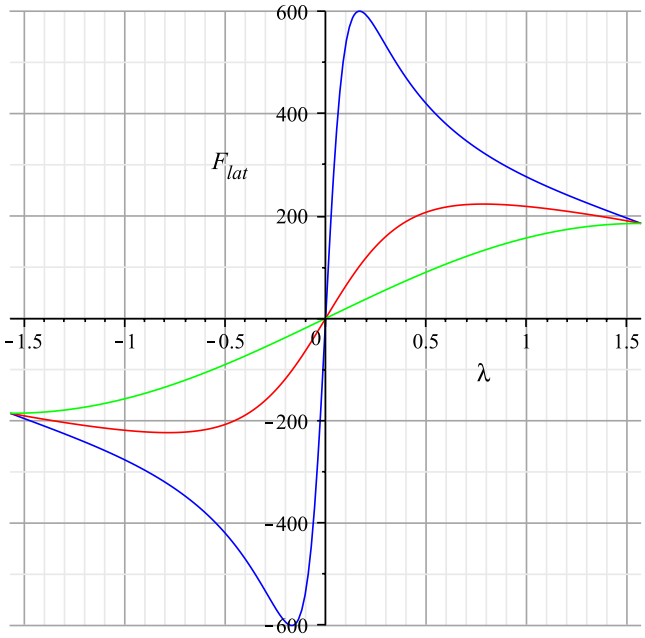

Figure 2.13: Lateral force varying the side-slip angle λ at different slip ratios: braking condition. Blue $= 0$, Red $= -0.5$, Green $= -0.99$.

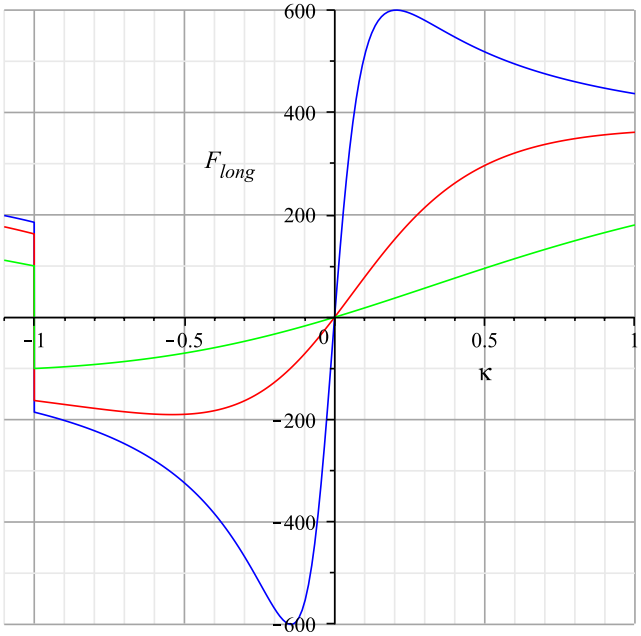

Figure 2.14: Longitudinal force varying the slip ratio κ at different side-slip angles. Blue $= 0\ rad$, Red $= 0.5\ rad$, Green $= 1\ rad$.

$$F_{long} = (N, \lambda, \phi, \kappa) \rightarrow -\frac{\sigma_x}{\sigma_{eq}} D_\kappa \sin\{C_\kappa \arctan[B_X - E_\kappa(B_\kappa \arctan B_X)]\}\ N \quad (2.23)$$

and an example of its shape varying the longitudinal slip for different side-slip angles is shown in Fig.(2.14).

In addition Fig.(2.15) and Fig.(2.16) are presented to clarify how the two interactions (i.e. lateral and longitudinal) vary and mutually influence each other both for low (Fig.(2.15)) and high (Fig.(2.16)) values of the side-slip angle for a certain range of longitudinal slip quantities. The asymmetry with respect to κ can be once more noticed.

It can be noticed how near the critical value for the longitudinal slip of $\kappa = -1$, that corresponds to wheel locked, the curve change its sign, thus the parameter ϵ mentioned above is necessary to avoid computational issue in the simulations of maneuvers involving such extreme condition.

Finally in Fig.(2.17) the adherence ellipse collecting the effects of the coupling between lateral and longitudinal interactions is reported. From the observation of its shape is once more relevant the asymmetry between driving and braking condition, due to a representation as function of practical slip quantities instead of theoretical.

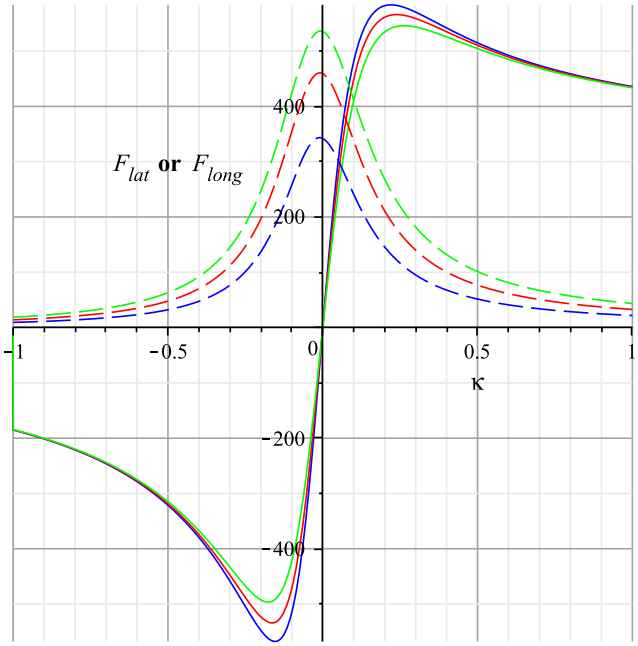

Figure 2.15: Lateral (dashed lines) and longitudinal (solid lines) forces varying the slip ratio at different low side-slip angle values. Blue $= 0.05\ rad$, Red $= 0.075\ rad$, Green $= 0.1\ rad$.

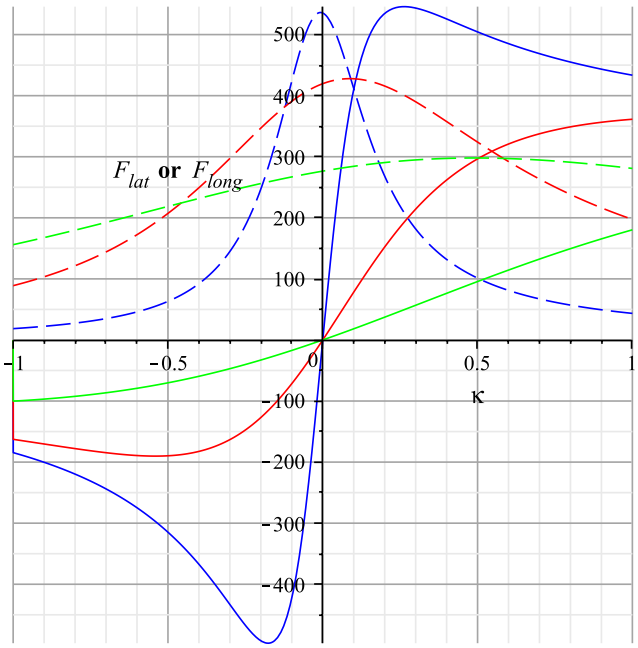

Figure 2.16: Lateral (dashed lines) and longitudinal (solid lines) forces varying the slip ratio at different high side-slip angle values. Blue $= 0.1\ rad$, Red $= 0.5\ rad$, Green $= 1\ rad$.

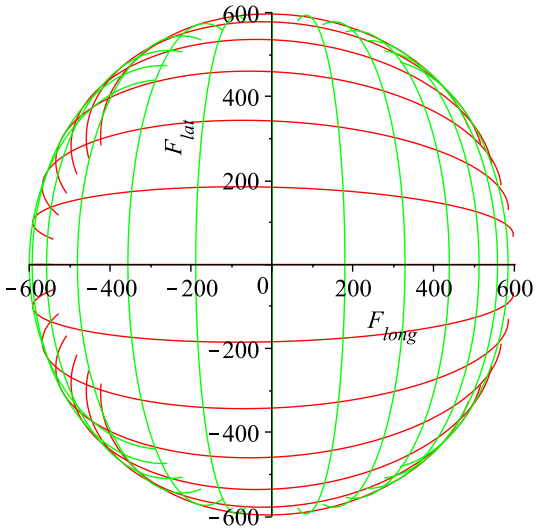

Figure 2.17: Adherence ellipse resulting from lateral and longitudinal interactions coupling.

2.2.3 Data file format

As in the suspension library case the user has to set just a few parameters in order to define its own tire-ground interaction curves corresponding to the selected model. The code below shows that a LUA code structure "rearTire" (same for front tire) is filled by means of a LUA function corresponding to the name of the desired tire model (e.g. "linear_tire"). This last can be change by the user to select all the available models.
Every model requires its own parameters as shown in the followings listed code.
The function checks whether all the parameters are set, if not it assigns default values to them.

Listing 2.5: Parameters for linear tire model set by the proper LUA function.

```
rearTire = linear_tire { name = "Rear Tire",comment = "No comment",

     sideslip_force     = {
                             stiffness = 34      -- stiffness  ->  default: 10
                          },
     camber_force       = {
                             stiffness = 0.9146  -- stiffness  ->  default: 1.0
                          },
     longitudinal_force = {
                             stiffness = 40      -- stiffness  ->  default: 15
                          },
nil}
```

Listing 2.6: Parameters for Uncoupled Pacejka tire model set by the proper LUA function.

```
rearTire = uncoupled_Pacejka_tire{ name = "Rear Tire",comment = "No comment",

     sideslip_force     = {
                             B  = 7.0,          -- Stiffness Factor
                             C  = 1.8,          -- Shape Factor     -> default: 1.5
                             D  = 1.0,          -- Peak Value       -> default: 1.5
                             E  = 0             -- Curvature Factor -> default: 0.0
                          },
     camber_force       = {
                             B  = 0.1500,       -- Stiffness Factor -> default: 0.15
                             C  = 5.730         -- Shape Factor     -> default: 5.5
                          },
     longitudinal_force = {
                             B  = 7.0,          -- Stiffness Factor -> default: 5.5
                             C  = 1.8,          -- Shape Factor     -> default: 1.5
                             D  = 1.0,          -- Peak Value       -> default: 1.5
                             E  = 0             -- Curvature Factor -> default: 0.0
                          },
 nil}
```

Listing 2.7: Parameters for Coupled Pacejka tire model set by the proper LUA function.

```
rearTire = coupled_Pacejka_tire{ name = "Rear Tire",comment = "No comment",

     sideslip_force     = {
                             B  = 7.0,          -- Stiffness Factor
                             C  = 1.8,          -- Shape Factor     -> default: 1.5
                             D  = 1.0,          -- Peak Value       -> default: 1.5
                             E  = 0,            -- Curvature Factor -> default: 0.0
                             eps = 1E-06        -- Working parameter -> default: 1E-06
                          },
     camber_force       = {
                             B  = 0.1500,       -- Stiffness Factor -> default: 0.15
                             C  = 5.730         -- Shape Factor     -> default: 5.5
                          },
     longitudinal_force = {
                             B  = 7.0,          -- Stiffness Factor -> default: 5.5
                             C  = 1.8,          -- Shape Factor     -> default: 1.5
                             D  = 0.6,          -- Peak Value       -> default: 1.5
                             E  = 0             -- Curvature Factor -> default: 0.0
                          },
nil}
```

2.2.4 C++ code

The management of the different models that can be include in the tire library is again developed in C++ language. Different classes are defined as follows:

Tire: it is a tire manager, its setup method is capable of reading the type of the tire model selected by the user. Setup and Forces methods (i.e. C++ functions) used are those of the chosen tire model.
It contains all methods that are include in the TireBase class.

TireBase: it's basically a generic tire, all sub-classes (i.e. tire models) will implement their specific version of TireBase virtual methods in order to employ their own tire model.
In this class are code skeletons of all the methods including setup and forces for tire-ground interaction forces.

TireLinear: it inherits methods from TireBase class and specifies them with its own mathematical definitions.

TireUncoupledPacejka: it inherits methods from TireBase class and specifies them with its own mathematical definitions.

TireCoupledPacejka: it inherits methods from TireBase class and specifies them with its own mathematical definitions.

Setup methods for tire manager and tire models classes are reported herein, whole code for Tire and TireBase classes is not shown for brevity.

Listing 2.8: Tire manager setup method C++ code.

```
/*
 _____  _                                _
|_   _|(_) _ __  ___          ___   ___ | |_  _   _  _ __
  | |  | || |__|/ _ \ _____ / __| / _ \| __|| | | || |_ \
  | |  | || |   |  __/|_____|\__ \|  __/| |_ | |_| || |_) |
  |_|  |_||_|    \___|       |___/ \___| \__| \__,_|| .__/
                                                    |_|
*/
  void
  Tire::setup( MapValues const & vars, MapStrings const & strings ) {
    ofstream TireLongFile ((tireName + "TireLongFile.txt").c_str());
    ofstream TireLatFile  ((tireName + "TireLatFile.txt").c_str());
    string tireType = getStringWithPrefix( strings, tireName, "type") ;
    // Reads the type of tire from TIRE0_data_type

    if      ( pTire    != NULL              ) delete pTire ;
    if      ( tireType == "Linear"          ) pTire = new TireLinear ;
    else if ( tireType == "UncoupledPacejka" ) pTire = new TireUncoupledPacejka ;
    else if ( tireType == "CoupledPacejka"   ) pTire = new TireCoupledPacejka ;
    else    cerr << "Unkwnon␣Tire␣type<" << tireType << ">"<< '\n' ;

    // setup model
    pTire -> setup( tireName, vars, strings ) ;

    // Finds the points of the diagram of the longitudinal force
    for ( valueType kappa = -1 ; kappa <= 1 ; kappa += 0.005 )
      TireLongFile << setw(10) << kappa << '\t'
                   << setw(10) << pTire->tireFLong(1000, 0, 0, kappa)
                   << '\n' ;

    // Finds the points of the diagram of the lateral force
    for ( valueType lambda = -1 ; lambda <= 1 ; lambda += 0.005 )
      TireLatFile << setw(10) << lambda << '\t'
                  << setw(10) << pTire->tireFLat(1000, lambda, 0, 0)
                  << '\n' ;

                TireLongFile . close() ;
                TireLatFile  . close() ;
  };
```

Once the tire model has been set through **type** variable its own **setup** method is defined. The main setup method produces also two files containing diagrams for lateral and longitudinal forces corresponding to the desired model. Setup methods for the different models are reported herein:

Listing 2.9: Linear tire model setup C++ code.

```
/*
  _      _
 | |    (_)_ __    ___  __ _ _ __
 | |    | | |_ \ / _ \/ _| | |__|
 | |___| | | | |  __/ (_| | |
 |_____|_|_| |_|\___|\__,_|_|

*/
  void
  TireLinear::setup(string const & prefix, MapValues const & vars,
                    MapStrings const & strings ) {
    // Checks if ex. TIRE0_name is present:
    name    = getStringWithPrefix( strings, prefix, "name" ) ;
    comment = getStringWithPrefix( strings, prefix, "comment" ) ;
    // Records KL, KLong in specified variables
    KLat  = getValueWithPrefix( vars, prefix, "KLat"  );
    Kphi  = getValueWithPrefix( vars, prefix, "Kphi" );
    KLong = getValueWithPrefix( vars, prefix, "KLong" );
  }

  #include "linear_tire_formulas_lib.cc"
```

The last **include** command open another file containing the specific formulation for tire-ground interaction forces force and its derivatives.
The user have just to define equations for its model by means of the symbolic algebra software Maple, and then execute a Maple procedure that automatically computes all derivatives for the different arguments of tire forces function and generates C++ file (e.g. linear_tire_formulas_lib.cc) that will be include in the libraries.

Listing 2.10: Uncoupled Pacejka tire model setup C++ code.

```
/*
  _   _                                  _          _ ____                  _ _
 | | | |_ __   ___ ___  _   _ _ __ | | ___  __| |  _ \ __ _  ___ ___ (_) | ____ _
 | | | | |_ \ / __/ _ \| | | | |_ \| |/ _ \/ _| | |_) / _| |/ __/ _ \| | |/ / _| |
 | |_| | | | | (_| (_) | |_| | |_) | |  __/ (_| |  __/ (_| | (_|  __/| |   < (_| |
  \_ __/|_| |_|\___\___/ \__,_| .__/|_|\___|\__,_|_|   \__,_|\___\___|/ |_|\_\__,_|
                              |_|                                    |__/
*/
  void
  TireUncoupledPacejka::setup( string const &  prefix, MapValues const & vars,
                               MapStrings const & strings ) {
    // Checks if ex. TIRE0_name is present:
    name    = getStringWithPrefix( strings, prefix, "name" ) ;
    comment = getStringWithPrefix( strings, prefix, "data_comment" ) ;
    // Records Bs,Cs,Ds,Es,Bl,Cl,Dl,El in the specified variables:
    LoadDep = getValueWithPrefix( vars, prefix, "data_sideslip_force_LoadDep" );
    Bs      = getValueWithPrefix( vars, prefix, "data_sideslip_force_B" );
    Cs      = getValueWithPrefix( vars, prefix, "data_sideslip_force_C" );
    Ds      = getValueWithPrefix( vars, prefix, "data_sideslip_force_D" );
    Es      = getValueWithPrefix( vars, prefix, "data_sideslip_force_E" );
    Bc      = getValueWithPrefix( vars, prefix, "data_camber_force_B" );
    Cc      = getValueWithPrefix( vars, prefix, "data_camber_force_C" );
    Dc      = getValueWithPrefix( vars, prefix, "data_camber_force_D" );
    Bl      = getValueWithPrefix( vars, prefix, "data_longitudinal_force_B" );
    Cl      = getValueWithPrefix( vars, prefix, "data_longitudinal_force_C" );
    Dl      = getValueWithPrefix( vars, prefix, "data_longitudinal_force_D" );
    El      = getValueWithPrefix( vars, prefix, "data_longitudinal_force_E" );
  }

  #include "uncoupled_Pacejka_tire_formulas_lib.cc"
```

Listing 2.11: Coupled Pacejka tire model setup C++ code.

```
/*
   ____                    _          _ _____                    _ _
  / ___|___  _   _ _ __ | | ___  __| |  _ \ __ _  ___ ___ (_) | ____ _
 | |   / _ \| | | | |_ \| |/ _ \/ _| | |_) / _| |/ __/ _ \| | |/ / _| |
 | |__| (_) | |_| | |_) | |  __/ (_| |  __/ (_| | (_|  __/| |    < (_| |
  \____\___/ \__,_| .__/|_|\___|\__,_|_|   \__,_|\___\___|/ |_|\_\__,_|
                  |_|                                    |__/
*/
 void
 TireCoupledPacejka::setup( string const &  prefix, MapValues const & vars,
                            MapStrings const & strings ) {
   // Checks if ex. TIRE0_name is present:
   name    = getStringWithPrefix( strings, prefix, "name" ) ;
   comment = getStringWithPrefix( strings, prefix, "data_comment" ) ;
   // Records Bs,Cs,Ds,Es,Bl,Cl,Dl,El in the specified variables:
   LoadDep = getValueWithPrefix( vars, prefix, "data_sideslip_force_LoadDep" );
   Bs      = getValueWithPrefix( vars, prefix, "data_sideslip_force_B" );
   Cs      = getValueWithPrefix( vars, prefix, "data_sideslip_force_C" );
   Ds      = getValueWithPrefix( vars, prefix, "data_sideslip_force_D" );
   Es      = getValueWithPrefix( vars, prefix, "data_sideslip_force_E" );
   Bc      = getValueWithPrefix( vars, prefix, "data_camber_force_B" );
   Cc      = getValueWithPrefix( vars, prefix, "data_camber_force_C" );
   Dc      = getValueWithPrefix( vars, prefix, "data_camber_force_D" );
   Bl      = getValueWithPrefix( vars, prefix, "data_longitudinal_force_B" );
   Cl      = getValueWithPrefix( vars, prefix, "data_longitudinal_force_C" );
   Dl      = getValueWithPrefix( vars, prefix, "data_longitudinal_force_D" );
   El      = getValueWithPrefix( vars, prefix, "data_longitudinal_force_E" );
   eps     = getValueWithPrefix( vars, prefix, "data_eps" );

 }

 #include "coupled_Pacejka_tire_formulas_lib.cc"
```

2.2.5 Maple procedure

The procedure for formulas and derivatives computation of the tire model functions and include file (for methods specification) generation is reported below:

Listing 2.12: Maple procedure for derivatives computation and include file generation.

```
# Print code
CgenerateFunction := proc(tirevars,ModelType,force,index1::integer:=0,index2::integer:=0)
  local F,list,i:
  printf("valueType %s::%s",ModelType,force):
  F := force(N,lambda,phi,kappa):
  if index1>0 then F := diff(F, tirevars[index1]): printf("_%d",index1): end:
  if index2>0 then F := diff(F, tirevars[index2]): printf("_%d",index2): end:
  printf("(
    valueType N,
    valueType lambda,
    valueType phi,
    valueType kappa) const
  { valueType f;\n");
  list := [codegen[optimize](F)];
  nops(list);
  for i from 1 to nops(list) do printf("valueType"),
  printf(lhs(list[i])),printf(";\n") end do;
  interface(warnlevel=0);
  CodeGeneration[C]([codegen[optimize](F)]);
  CodeGeneration[C]([f= lhs(list[nops(list)])]);
  printf("return(f);
  };\n\n");
end proc:
```

```
# Main procedure
CodeGeneration_tire := proc(FLateral, FLongitudinal, ModelType,tirevars)
    local tireFLat,tireFLong:
    tireFLat  := (tirevars) -> FLateral;
    tireFLong := (tirevars) -> FLongitudinal;

    CgenerateFunction(tirevars,ModelType,tireFLat);
    CgenerateFunction(tirevars,ModelType,tireFLat,1);
    CgenerateFunction(tirevars,ModelType,tireFLat,2);
    CgenerateFunction(tirevars,ModelType,tireFLat,3);
    CgenerateFunction(tirevars,ModelType,tireFLat,4);
    CgenerateFunction(tirevars,ModelType,tireFLat,1,1);
    CgenerateFunction(tirevars,ModelType,tireFLat,1,2);
    CgenerateFunction(tirevars,ModelType,tireFLat,1,3);
    CgenerateFunction(tirevars,ModelType,tireFLat,1,4);
    CgenerateFunction(tirevars,ModelType,tireFLat,2,2);
    CgenerateFunction(tirevars,ModelType,tireFLat,2,3);
    CgenerateFunction(tirevars,ModelType,tireFLat,2,4);
    CgenerateFunction(tirevars,ModelType,tireFLat,3,3);
    CgenerateFunction(tirevars,ModelType,tireFLat,3,4);
    CgenerateFunction(tirevars,ModelType,tireFLat,4,4);

    CgenerateFunction(tirevars,ModelType,tireFLong);
    CgenerateFunction(tirevars,ModelType,tireFLong,1);
    CgenerateFunction(tirevars,ModelType,tireFLong,2);
    CgenerateFunction(tirevars,ModelType,tireFLong,3);
    CgenerateFunction(tirevars,ModelType,tireFLong,4);
    CgenerateFunction(tirevars,ModelType,tireFLong,1,1);
    CgenerateFunction(tirevars,ModelType,tireFLong,1,2);
    CgenerateFunction(tirevars,ModelType,tireFLong,1,3);
    CgenerateFunction(tirevars,ModelType,tireFLong,1,4);
    CgenerateFunction(tirevars,ModelType,tireFLong,2,2);
    CgenerateFunction(tirevars,ModelType,tireFLong,2,3);
    CgenerateFunction(tirevars,ModelType,tireFLong,2,4);
    CgenerateFunction(tirevars,ModelType,tireFLong,3,3);
    CgenerateFunction(tirevars,ModelType,tireFLong,3,4);
    CgenerateFunction(tirevars,ModelType,tireFLong,4,4);

end proc:

# Save maple input file
currentdir("UserDir"):
save CgenerateFunction, CodeGeneration_tire, "CodeGeneration_tire_OPTIMIZED.mpl":
```

Chapter 3

Enhanced vehicle models and Optimal Maneuver Method applications

Since it has been developed, the Optimal Maneuver Method has been widely used to study handling and maneuverability of motorcycles but also focusing on performance. Minimum lap time simulations have been performed with the aim of optimizing main vehicle geometric and inertial properties on different tracks.
To do this complex model equations must be integrated to allow for very particular aspects of the vehicle dynamics and detailed description of components such as power-train and chain force transmission required a specific attention.
The virtual prototyping of a motorcycle is not the only application of this methodology. In the next sections different vehicle models will be presented. They have been developed for different purposes that cover other aspects in vehicle dynamics and will be illustrate afterwards.
For each model a brief description of its peculiarities is presented before going deep in the mathematical formulation reporting equations of motion when possible for their complexity.
As explained in the previous chapter the modeling of some parts are communal for more models, thus it will be referred to section 2 for further details.
For each of the mentioned model specific applications or at least simulations examples are reported.

3.1 Monobike: single motorcycle rigid wheel running on a track

Working with complex models can be useful for studying details in vehicle dynamics. Instead, if the purpose of the research is to analyze the accuracy and the potentiality of a methodology such as the Optimal Maneuver Method, the complexity of the model can represent a limit.
The purpose is to present one of the most essential model that can be used to study the behavior of a motorcycle and, at the same time, to investigate the causes of the problems that occurs when the Optimal Maneuver Method is employed to simulate different vehicles such as motorcycles and four-wheeled vehicles, as the mathematical definition of physical limits of the vehicle itself (e.g. maximum power limit) or regarding its interaction with the road in terms of adherence.
The simplest model capable of capturing the essential motorcycle dynamics is a rigid body running on a track and free to roll. In particular, one can imagine this model as a rolling motorcycle wheel of proper size and inertia including center of mass of the motorcycle, gyroscopic

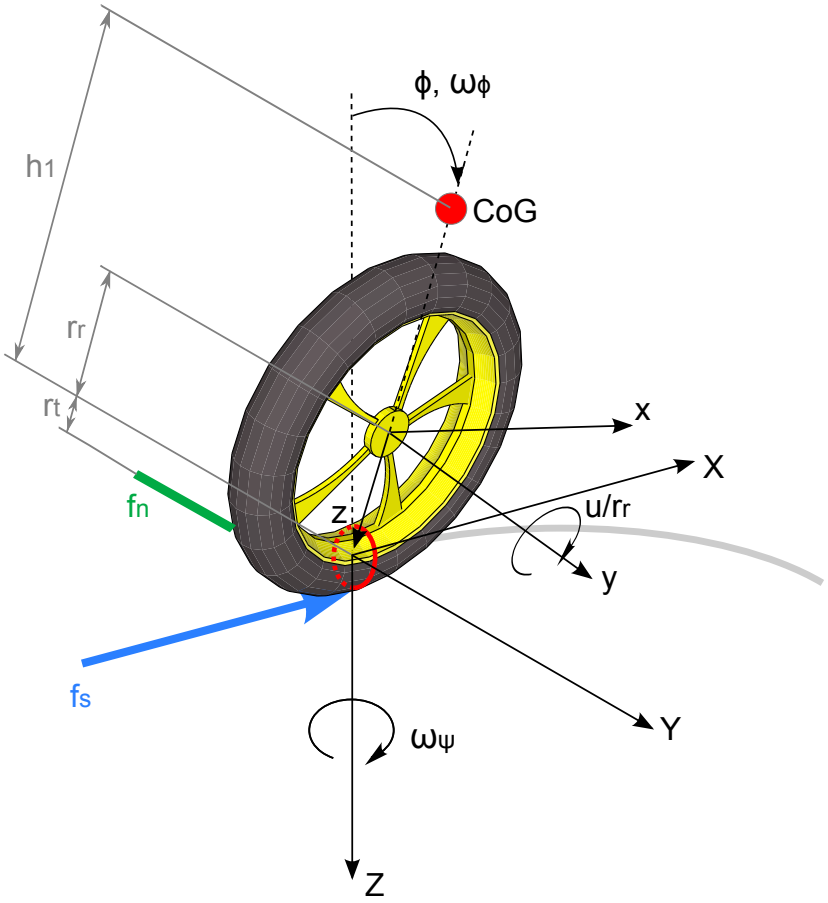

Figure 3.1: Monobike model scheme

effects and tire shape features that are important in motorcycle dynamics, as is well known. The vehicle model consists of 7 differential equations, which comprise 2 equations of motion:

$$\dot{u} = \left[2\,\omega_\psi\,\cos(\phi)\,\omega_\phi + \psi_{acc}\,\sin(\phi)\right]\,h_1 + g\,f_s - \frac{k_A\,u^2}{m} \tag{3.1}$$

$$\begin{aligned}\dot{\omega}_\phi = &\frac{\left[\omega_\psi\,(m_w\,r_r^2 + m\,h_1^2)\,\sin(\phi) - u\,(r_r\,m_w + m\,h_1)\right]\,\omega_\psi\,\cos(\phi)}{I_X + m\,h_1\,\cos(\phi)\,r_t + m\,h_1^2} \\ &+ \frac{\left[h_1\,(\omega_\psi^2\,r_t + g + r_t\,\omega_\phi^2)\,\sin(\phi) - \omega_\psi r_t\,u\right]\,m}{I_X + m\,h_1\,\cos(\phi)\,r_t + m\,h_1^2}\end{aligned} \tag{3.2}$$

two first order equations:

$$\dot{\omega}_\psi = \psi_{acc} \tag{3.3}$$

$$\dot{\phi} = \omega_\phi \tag{3.4}$$

plus eq.(1.62-1.64) for the position of the vehicle on the road, these last adjusted for u and v (longitudinal and lateral vehicle speeds) quasi-coordinates (instead of V and β), that will be shown later on, and as many state variables:

$$\mathbf{x} = \{u, \omega_\phi, \omega_\psi, \phi, s_s, s_n, \alpha\}^T \tag{3.5}$$

where u is the longitudinal speed with respect to the vehicle axis, ω_ϕ is the roll rate expressed by eq.3.4, ω_ψ is the yaw rate and ϕ is the roll angle of the wheel.
s_s, s_n, α are variables for the road definition.
It has to be noticed how v state is assumed equal to zero, thus lateral velocity for the wheel body is neglected.
The control vector consists of two elements:

$$\mathbf{u} = \{f_s, \psi_{acc}\}^T \tag{3.6}$$

where f_s is the the longitudinal tire force and ψ_{acc} is the rate of variation of the yaw rate (i.e. the acceleration of the yaw angle ψ).

3.1.1 Optimal Control Problem formulation

Now for a complete formulation of the optimal control problem employing this essential model some simplification are introduced in the equations.
It is assumed lenticular wheel, thus the radius of the toroid cross section of the tire is $r_t = 0$.
From this assumption the second equation of motion of the dynamic model results to be:

$$\dot{\omega}_\phi = \frac{\left[\omega_\psi \left(m_w\, r_r^2 + m\, h_1^2\right)\, \sin(\phi) - u\, (r_r\, m_w + m\, h_1)\right]\, \omega_\psi\, \cos(\phi)}{I_X + m\, h_1^2} + \frac{h_1\, g\, m\, \sin(\phi)}{I_X + m\, h_1^2} \tag{3.7}$$

then if we define $C_1 = \frac{m_w\, r_r^2 + m\, h_1^2}{I_X + m\, h_1^2}$, $C_2 = \frac{r_r\, m_w + m\, h_1}{I_X + m\, h_1^2}$ and $C_3 = \frac{h_1\, g\, m}{I_X + m\, h_1^2}$:
the dynamic system including both vehicle and road equations is the following:

$$\begin{aligned}
\dot{u} &= \left[2\, \omega_\psi\, \cos(\phi)\, \omega_\phi + \psi_{acc}\, \sin(\phi)\right]\, h_1 + g\, f_s - \frac{k_A\, u^2}{m} && (3.8)\\
\dot{\omega}_\phi &= \left[\omega_\psi\, C_1\, \sin(\phi) - u\, C_2\right]\, \omega_\psi\, \cos(\phi) + C_3\, \sin(\phi) && (3.9)\\
\dot{\omega}_\psi &= \psi_{acc} && (3.10)\\
\dot{\phi} &= \omega_\phi && (3.11)\\
\dot{s} &= \frac{u\cos(\alpha)}{1 - nK} && (3.12)\\
\dot{n} &= u\sin(\alpha) && (3.13)\\
\dot{\alpha} &= \omega_\psi - K\frac{u\cos(\alpha)}{1 - nK} && (3.14)
\end{aligned}$$

where $s = s_s$ and $n = s_n$ with respect to to the formulation in section 1.3.1. Since the dynamics of a vehicle is computed the changing in independent variable form time t to curvilinear abscissa s explained in section 1.3.1 it is necessary. To do this a different state variable $\zeta_{dot} = \dot{s}$ and a different differential equation are introduced in the formulation.
This last is a stabilization equation (τ is the stabilizing factor) for the equation 3.12 that for

the variable change would result algebraic (in this way it is transformed into a differential one). Because of the independent variable change all equations must be multiplied by $\frac{1}{\zeta_{dot}}$ as follows:

$$\dot{u} = \frac{1}{\zeta_{dot}} \left\{ \left[2\,\omega_\psi\ \cos(\phi)\,\omega_\phi + \psi_{acc}\ \sin(\phi) \right] h_1 + g\ f_s - \frac{k_A\ u^2}{m} \right\} \tag{3.15}$$

$$\dot{\omega}_\phi = \frac{1}{\zeta_{dot}} \left\{ \left[\omega_\psi\ C_1\ \sin(\phi) - u\ C_2 \right] \omega_\psi\ \cos(\phi) + C_3\ \sin(\phi) \right\} \tag{3.16}$$

$$\dot{\omega}_\psi = \frac{1}{\zeta_{dot}} \psi_{acc} \tag{3.17}$$

$$\dot{\phi} = \frac{1}{\zeta_{dot}} \omega_\phi \tag{3.18}$$

$$\dot{\zeta}_{dot} = \frac{1}{\zeta_{dot}} \frac{u\cos(\alpha) + (n\ K - 1)\zeta_{dot}}{(1 - n\ K)\tau} \tag{3.19}$$

$$\dot{n} = \frac{1}{\zeta_{dot}}\, u \sin(\alpha) \tag{3.20}$$

$$\dot{\alpha} = \frac{1}{\zeta_{dot}} \left\{ \omega_\psi - K \frac{u\cos(\alpha)}{1 - n\ K} \right\} \tag{3.21}$$

The performance index that has to be minimized, according to section 1.3, is the following:

$$J = \phi[\mathbf{x}(s_f)] + \int_{s_0}^{s_f} L[\mathbf{x}(s), \mathbf{u}(s)] ds \tag{3.22}$$

that in this particular case in which no costs on the final value of the state vector (i.e. Mayer term) (i.e. $\phi[\mathbf{x}(s_f)] = 0$) are assumed and a Lagrange term that aims at maximizing the speed of the vehicle on the middle lane of the road throughout the maneuver is chosen, Eq.3.22 becomes:

$$J = \int_{s_0}^{s_f} \frac{1}{\zeta_{dot}} ds \tag{3.23}$$

this is subject to equality constraints represented by equations of the dynamic system shown before, initial boundary conditions:

$$\mathbf{x}(s_0) = \mathbf{x}_0 \tag{3.24}$$

that for the case study are basically

$$u(s_0) = 10 \tag{3.25}$$

$$\zeta_{dot}(s_0) = 10 \tag{3.26}$$

and terminal constraints:

$$\boldsymbol{\psi}[\mathbf{x}(t_f)] = 0 \tag{3.27}$$

System equations are included in the performance index J by means of Lagrange multipliers $\boldsymbol{\lambda}$ to obtain:

$$\bar{J} = \boldsymbol{\nu}^T \boldsymbol{\psi} + \int_{s_0}^{s_f} \left\{ L[\mathbf{x}(s), \mathbf{u}(s)] + \boldsymbol{\lambda}^T(s) \left[\mathbf{f}[\mathbf{x}(s), \mathbf{u}(s)] - \dot{\mathbf{x}} \right] \right\} ds \tag{3.28}$$

and thus because for the current case also no terminal constraints are assumed (i.e. $\psi[\mathbf{x}(s_f)] = 0$) we obtain:

$$\begin{aligned}\bar{J} = \int_{s_0}^{s_f} \Big\{ & \frac{1}{\zeta_{dot}} + \lambda_1 \Big[\frac{1}{\zeta_{dot}} \Big\{ \Big[2\,\omega_\psi\ \cos(\phi)\,\omega_\phi + \psi_{acc}\ \sin(\phi) \Big]\ h_1 + g\ f_s - \frac{k_A\ u^2}{m} \Big\} - \dot{u} \Big] + \\ & + \lambda_2 \Big[\frac{1}{\zeta_{dot}} \Big\{ \Big[\omega_\psi\ C_1\ \sin(\phi) - u\ C_2 \Big]\ \omega_\psi\ \cos(\phi) + C_3\ \sin(\phi) \Big\} - \dot{\omega}_\phi \Big] + \\ & + \lambda_3 \Big[\frac{1}{\zeta_{dot}} \psi_{acc} - \dot{\omega}_\psi \Big] + \\ & + \lambda_4 \Big[\frac{1}{\zeta_{dot}} \omega_\phi - \dot{\phi} \Big] + \\ & + \lambda_5 \Big[\frac{1}{\zeta_{dot}}\ \frac{u\cos(\alpha) + (n\ K - 1)\zeta_{dot}}{(1 - n\ K)\tau} - \dot{\zeta}_{dot} \Big] + \\ & + \lambda_6 \Big[\frac{1}{\zeta_{dot}}\ u\sin(\alpha) - \dot{n} \Big] + \\ & + \lambda_7 \Big[\frac{1}{\zeta_{dot}}\ \Big\{ \omega_\psi - K \frac{u\cos(\alpha)}{1 - n\ K} \Big\} - \dot{\alpha} \Big] \Big\} ds \end{aligned} \tag{3.29}$$

being the Hamiltonian H:

$$H(s) = L(s) + \boldsymbol{\lambda}^T(s)\mathbf{f}[\mathbf{x}(s), \mathbf{u}(s)] \tag{3.30}$$

and thus for the specific case:

$$\begin{aligned} H = & \frac{1}{\zeta_{dot}} + \lambda_1 \Big[\frac{1}{\zeta_{dot}} \Big\{ \Big[2\,\omega_\psi\ \cos(\phi)\,\omega_\phi + \psi_{acc}\ \sin(\phi) \Big]\ h_1 + g\ f_s - \frac{k_A\ u^2}{m} \Big\} \Big] + \\ & + \lambda_2 \Big[\frac{1}{\zeta_{dot}} \Big\{ \Big[\omega_\psi\ C_1\ \sin(\phi) - u\ C_2 \Big]\ \omega_\psi\ \cos(\phi) + C_3\ \sin(\phi) \Big\} \Big] + \\ & + \lambda_3 \Big[\frac{1}{\zeta_{dot}} \psi_{acc} \Big] + \\ & + \lambda_4 \Big[\frac{1}{\zeta_{dot}} \omega_\phi \Big] + \\ & + \lambda_5 \Big[\frac{1}{\zeta_{dot}}\ \frac{u\cos(\alpha) + (n\ K - 1)\zeta_{dot}}{(1 - n\ K)\tau} \Big] + \\ & + \lambda_6 \Big[\frac{1}{\zeta_{dot}}\ u\sin(\alpha) \Big] + \\ & + \lambda_7 \Big[\frac{1}{\zeta_{dot}}\ \Big\{ \omega_\psi - K \frac{u\cos(\alpha)}{1 - n\ K} \Big\} \Big] \end{aligned} \tag{3.31}$$

For the sake of brevity mathematical transformations Eq.(1.49)-Eq.(1.52) are not shown for the current case. From these the necessary condition for a stationary solution for arbitrary δu is reduced to solve 1.53 and corresponds to the following set of equations:

final condition equations for the case without Mayer term on final states and without terminal constraints:

$$-\boldsymbol{\lambda}^T(s_f) = 0 \tag{3.32}$$

that for the current case study are

$$\lambda_i(s_f) = 0 \qquad with \quad i = 1..7 \tag{3.33}$$

free initial states equations:

$$\boldsymbol{\lambda}^T(s_0) = 0 \tag{3.34}$$

that are

$$\lambda_i(s_0) = 0 \qquad with \quad i = 2, 3, 4, 6, 7 \tag{3.35}$$

where the index i corresponds to the states whom initial value has been set (Eq.(3.25-3.26)).
Co-equations:

$$\mathbf{H}_x + \dot{\boldsymbol{\lambda}}^T = 0 \tag{3.36}$$

that in this specific case are:

$$\frac{(-\lambda_5 + \lambda 7\ K\ \tau)\cos(\alpha)}{\zeta_{dot}\ (n\ K-1)\tau} - \frac{(-2\ \lambda_1\ g\ f_s\ k_A\ u - \lambda_6 \sin(\alpha) m + \lambda_2\ C_2 \omega_\psi \cos(\phi) m)}{\zeta_{dot}\ m} + \dot{\lambda}_1 = 0 \tag{3.37}$$

$$\frac{2\ \lambda_1\ \omega_\psi \cos(\phi) h_1 + \lambda_4}{\zeta_{dot}} + \dot{\lambda}_2 = 0 \tag{3.38}$$

$$\frac{(2\ \lambda_1\ \omega_\phi h_1 + 2\ \lambda_2\ \omega_\psi C_1\ \sin(\phi) - \lambda_2\ u\ C_2)\cos(\phi) + \lambda_7}{\zeta_{dot}} + \dot{\lambda}_3 = 0 \tag{3.39}$$

$$\begin{aligned} &\frac{\lambda_2\ \omega_\psi^2\ C_1 \cos^2(\phi) + (\lambda_1\ h_1\ \psi_{acc} + \lambda_2\ C_3)\cos(\phi)}{\zeta_{dot}} + \\ &+ \frac{\omega_\psi \sin(\phi)(-\lambda_2\ \omega_\psi C_1 \sin(\phi) - 2\lambda_2\ \omega_\phi h_1 + \lambda_2\ u\ C_2)}{\zeta_{dot}} + \dot{\lambda}_4 = 0 \end{aligned} \tag{3.40}$$

$$\begin{aligned} &\frac{-2\ \omega_\psi(\frac{1}{2}\lambda_2 \omega_\psi C_1 \sin(\phi) + \lambda_1 \omega_\phi h_1 - \frac{1}{2}\lambda_2\ u\ C_2)\cos(\phi)}{\zeta_{dot}^2} + \\ &+ \frac{(\lambda_1\ h_1\ \psi_{acc} + \lambda_2\ C_3)\sin(\phi)}{\zeta_{dot}^2} - \frac{u\cos(\alpha)(-\lambda_5 + \lambda_7\ K\ \tau)}{\zeta_{dot}^2 (n\ K-1)\tau} - \\ &- \frac{\lambda_6\ u \sin(\alpha) m + (\lambda_4 \omega_\phi + \lambda_7 \omega_\psi + \lambda_3 \psi_{acc} + 1) m + \lambda_1\ g\ f_s\ k_A\ u^2}{\zeta_{dot}^2\ m} + \dot{\lambda}_5 = 0 \end{aligned} \tag{3.41}$$

$$-\frac{K\ u\ \cos(\alpha)(-\lambda_5 + \lambda_7\ K\ \tau}{\zeta_{dot}(n\ K-1)^2 \tau} + \dot{\lambda}_6 = 0 \tag{3.42}$$

$$\frac{\tau\ \lambda_6 (n\ K-1)\cos(\alpha) - \sin(\alpha)(-\lambda_5 + \lambda_7\ K\ \tau))u}{\zeta_{dot}(n\ K-1)\tau} + \dot{\lambda}_7 = 0 \tag{3.43}$$

Optimality equations:

$$\mathbf{H}_u = 0 \tag{3.44}$$

which are:

$$\frac{1}{\zeta_{dot}\, m}\lambda_1\, g\, k_A\, u^2 = 0 \tag{3.45}$$

$$\frac{1}{\zeta_{dot}}\lambda_1\, \sin(\phi)\, h_1\, \lambda_3 = 0 \tag{3.46}$$

Summarizing, the optimal solution for this specific case is found by solving the Two Point Boundary Value Problem (TPBVP) defined by the model equations Eq.(3.15-3.21), free initial states equations Eq.(3.35), co-equations Eq.(3.37-3.43), optimality equations Eq.(3.45), initial conditions Eq.(3.25-3.26) (first point of the TPBVP) and final conditions Eq.(3.33) (second point of the TPBVP).
To include inequality constraints in the current formulation Eq.(3.22) has to substituted by the following:

$$J = \phi[\mathbf{x}(s_f)] + \int_{s_0}^{s_f} L[\mathbf{x}(s), \mathbf{u}(s)] + \sum_{i=1}^{q} p_i[d_i(\mathbf{x}(s), \mathbf{u}(s))] \tag{3.47}$$

where p_i are penalty functions corresponding to an unilateral (or bilateral) version of the one shown in section 1.3 and d_i for the current case study represents lateral boundaries of the road thus:

$$n - W_R \leq 0 \tag{3.48}$$

$$n + W_L \geq 0 \tag{3.49}$$

so for the case study the performance index becomes:

$$J = \int_{s_0}^{s_f} \frac{1}{\zeta_{dot}} + p_1(n - W_R) + p_2(n + W_L)\, ds \tag{3.50}$$

where p_1 and p_2 are unilateral penalty functions whom shapes are the right hand side and left hand side of the one shown in section 1.3 respectively. Adjoining equality constraints in this particular case, leads to the following $\bar{J}$:

$$\bar{J} = \boldsymbol{\nu}^T\boldsymbol{\psi} + \int_{s_0}^{s_f} \Big\{ L[\mathbf{x}(s), \mathbf{u}(s)] + \sum_{i=1}^{q} p_i[d_i(\mathbf{x}(s), \mathbf{u}(s))] + \boldsymbol{\lambda}^T(s)\Big[\mathbf{f}[\mathbf{x}(s), \mathbf{u}(s)] - \dot{\mathbf{x}}\Big]\Big\} ds \tag{3.51}$$

then from Eq.(3.31) to Eq.(3.45) the formulation have to be updated to include these additional terms concerning inequality constraints limitations.

3.1.2 Testing new formulations

As mentioned above, one of the possible application for such an essential model is to employ it as lab vehicle in order to test new way to formulate the problem. As an example a test on different penalty functions corresponding to rider skills while driving the vehicle is presented. The complete formulation for the vehicle presented at the beginning of the chapter is assumed, and other penalty functions are added to the ones regarding road lateral limits.
A penalty on the maximum available power is formulated as:

$$\frac{f_s\, m\, g\, u}{P_{\max}} - 1 \leq 0 \tag{3.52}$$

another limitation is assumed coming from tire adherence and it's formulated as an adhesion ellipse as follows:

$$\frac{f_s^2}{\mu_X^2} + \frac{u^2\, \omega_\psi^2}{\mu_Y^2\, g^2} - 1 \leq 0 \tag{3.53}$$

Now since a limit for tire adherence is provided, the rider could be not able to exploit the whole available adhesion. As an example let's assume that from experimental evidence data it turns out that the driver cannot employ tires at their maximum capability. If simulations are used to test different solutions for the vehicle, but employable by that specific rider with its limits, another limitation must be provide to consider rider skills in the optimization:

$$\frac{f_s^2}{R_X^2} + \frac{u^2\, \omega_\psi^2}{R_Y^2\, g^2} - 1 \leq 0 \tag{3.54}$$

where R_X and R_Y are longitudinal and lateral acceleration limitations respectively. It has to be noticed how rider skills in term of accelerations are included again through an ellipse mathematical formulation. If the rider is not skilled at all it won't be able to generate high longitudinal and lateral acceleration at the same time. A new formulation aiming at realizing proper limitation for different riders is presented afterwards.
The idea is to add another penalty working in combination with the two previous ellipses having the shape of a rhombus, that can be enlarged or restrict to obtain different shapes between a pure ellipse and a pure rhombus.
The four equations corresponding to the four sides of the rhombus are:

$$-\frac{f_s}{R_X} + \frac{u\, \omega_\psi}{R_Y\, g} - q_r \leq 0 \tag{3.55}$$

$$-\frac{f_s}{R_X} - \frac{u\, \omega_\psi}{R_Y\, g} - q_r \leq 0 \tag{3.56}$$

$$\frac{f_s}{R_X} - \frac{u\, \omega_\psi}{R_Y\, g} - q_r \leq 0 \tag{3.57}$$

$$\frac{f_s}{R_X} + \frac{u\, \omega_\psi}{R_Y\, g} - q_r \leq 0 \tag{3.58}$$

where q_r is a parameter to set the tightness of the rhombus. Results for simulations including the different mentioned penalties are presented herein. Fig.3.2 reports trajectories for a whole

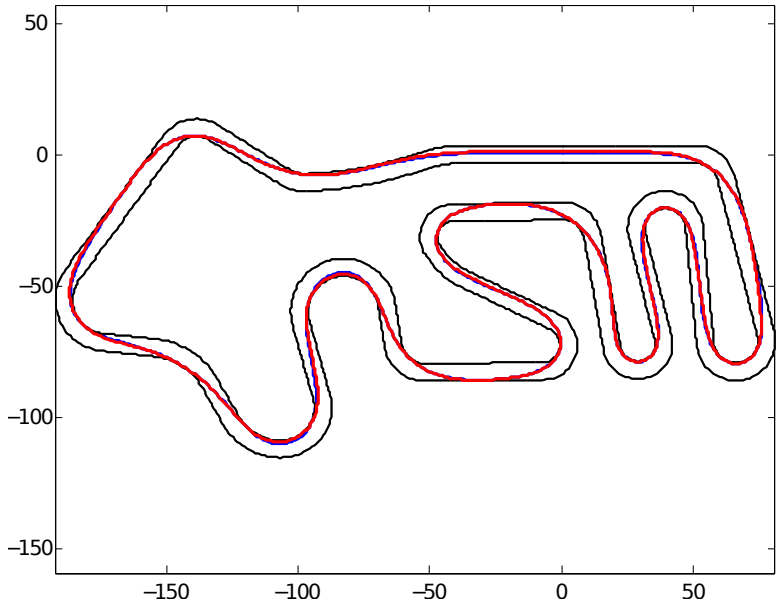

Figure 3.2: Trajectories calculated employing Monobike model with two different penalty functions: pure ellipse for the skilled rider (blue line) and combination between ellipse and rhombus for the less skilled rider (red line).

lap on closed circuit in the two cases of skilled and less skilled riders, corresponding to ellipse formulation and rhombus plus ellipse formulation respectively.

It turns out that the trajectories are really close in the two cases, although the non-skilled rider performs slightly different trajectories on u-turn throughout the track because of its inability of braking and accelerating while cornering.

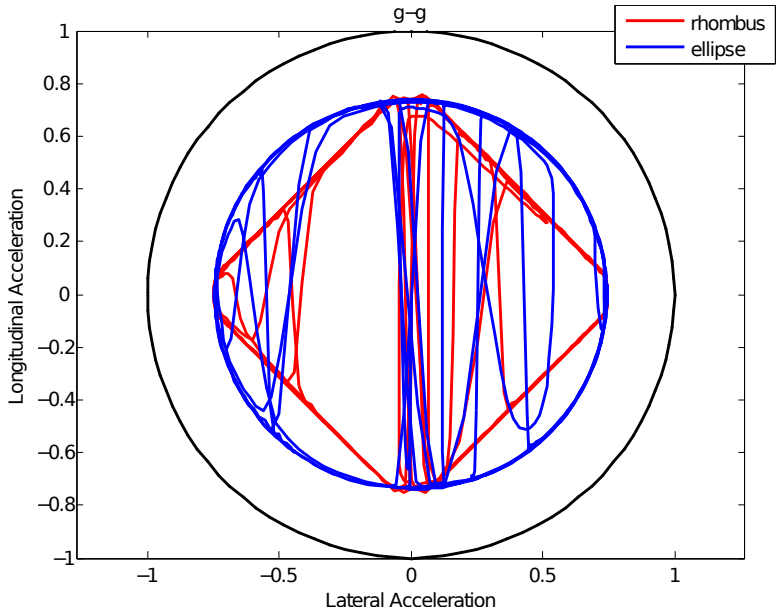

Figure 3.3: g-g diagrams of the whole track simulations for the ellipse (blue line) and rhombus-ellipse (red line) cases, in black tire adhesion ellipse is represented.

As explained above only penalty function regarding rider skills has been adjust in the two different cases. Fig.3.3 presents the acceleration diagrams (i.e. g-g diagram) for the same two

simulations of Fig.3.2 in which it's clear how the rider uses the available combined lateral and longitudinal accelerations. Furthermore tire adhesion is included to shows that if the rider is not enough skilled, the limit of tires is not reached.

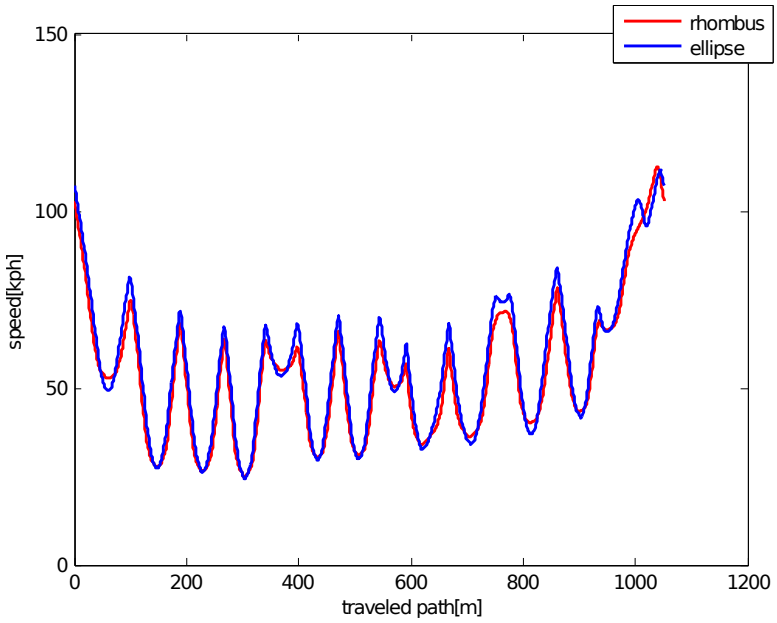

Figure 3.4: Longitudinal speed u for the the whole track simulations employing Monobike vehicle model.

The last diagram in Fig.3.4 reports longitudinal speed for the two simulations. It can be noticed that the non-skilled rider uses a different strategy with respect to the skilled one: on the apex of some of the turns it reaches higher speeds, but at the entry and at exit it is not able to accelerate hard longitudinally and laterally at the same time thus for the rest of the parts of the track it rides slower. In conclusion this example shows how the skills of the rider not only influence the total performance on the track lap, but also oblige to change strategy in terms of trajectories and speeds throughout the whole track.

3.1.3 Optimal Maneuver Method for motorcycles: Matlab GUI

In order to make know the Optimal Maneuver Method to industry and research groups for vehicle dynamics applications a simple program has been built in Matlab GUI (i.e. Graphic User Interface) environment.
The most important features for such application is that it has to be fast, simple and stable. To achieve this results the "Monobike" vehicle model presented in section 3.1 has been employed herein. A motorcycle like tire running one a track represents the most simple vehicle model capable of reproducing motorcycle maneuvers and run stably on every computed scenario (e.g. changing circuit track, adherence conditions, available power, etc.).
The easiness of this tool is that just a few parameters are adjustable by the user: the maximum available power, the adherence ellipse, thus longitudinal and lateral adherence limits.
Vehicle parameters and track are fixed, so that one can appreciate the speed in reaching the solution for a whole track and play with just a few parameters to immediately recognize the effect of their variation on the dynamics of the wheel vehicle. Outputs are simply the trajectory of the vehicle on the track enriched with colored markers speed profile, moreover final lap-time and maximum speed values, longitudinal speed profile, roll angle profile and yaw rate profile

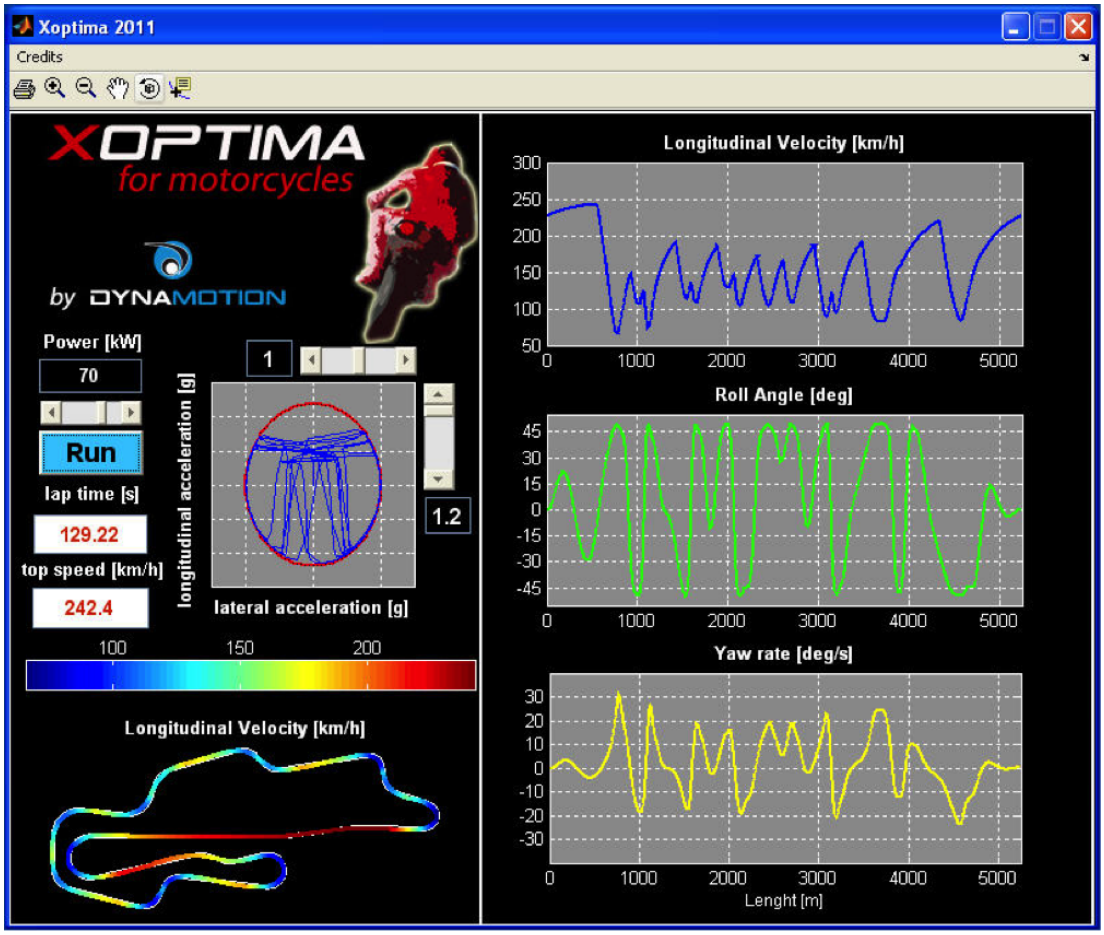

Figure 3.5: Demo for Optimal Maneuver Method promulgation based on the "Monobike" model.

are shown.
To start the optimization one have just to press the run button, and after a few seconds outputs are available. Furthermore the g-g acceleration diagram appears within the adherence ellipse, so that the user can check whether the imposed limits have been reached or not for the current track lap.

3.2 Single-Track: single-track model mimicking car maneuvers

The car model described herein is the single-track vehicle model consisting in a single rigid body shown in Fig. 3.18. For each axle the wheel includes the contribution of the left and the right wheel of the real vehicle. Pitch and roll rotations are neglected thus the motion is planar. However fore/aft load transfer are considered in the formulation.
If the aim is to optimize racing cars running on a track in a championship, it's important to describe in detail the different components and overall characteristics of the car, in order to appreciate the difference on the lap time when some parameters are slightly varied.
On the contrary if the focus is on the different driving styles that a driver can used while approaching the same curve, and the study of which of those can be considered optimal for the current conditions of the road, the complexity of the model can be reduced.
The reasons are that some aspects of the model can be ignored without losing the macro dynamics of the vehicle and that complex models could lead to wide systems of equations that are not simply either quick to solve. For example while using non-linear tire characteristics with particular lateral and longitudinal forces diagrams and combinations.
Recent papers [6, 11] have shown the capability of this simple model to reproduce complex and also aggressive maneuvers while matching experimental data logged on real vehicles.
In details: the equations of motion consist of Newton-Euler equations in the longitudinal,

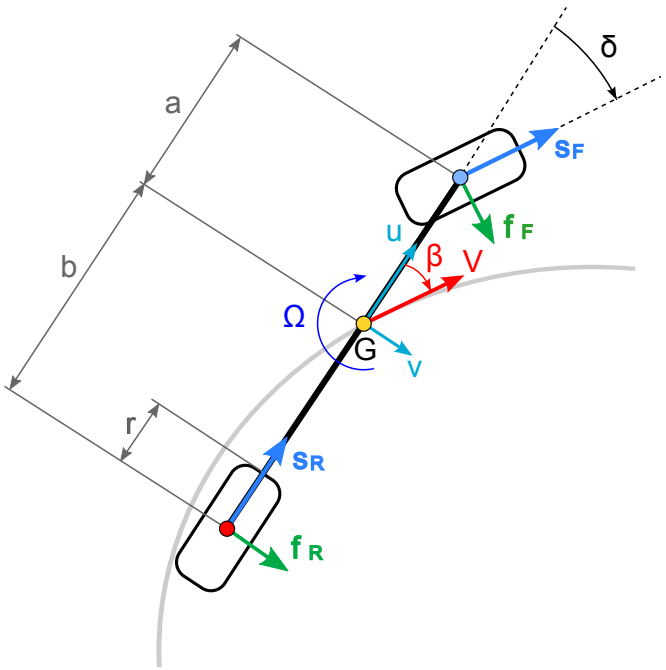

Figure 3.6: SingleTrack model scheme

lateral and yaw direction:

$$\begin{aligned}\dot{V} =& g\left(s_F\cos(\delta-\beta) - f_F\sin(\delta-\beta) + s_R\cos\beta + f_R\sin\beta\right)\\ &- \frac{k_D V^2(\cos\beta)^3}{M}\end{aligned} \tag{3.59}$$

$$\begin{aligned}\dot{\beta} =& \frac{g}{V}\left(s_F \sin(\delta-\beta) + f_F \cos(\delta-\beta) - s_R \sin\beta + f_F \cos\beta\right) \\ & - \Omega + \frac{k_D V \sin\beta (\cos\beta)^2}{M}\end{aligned} \tag{3.60}$$

$$\dot{\Omega} = \frac{Mg}{I_G}\left(a\left(f_F \cos\delta + s_F \sin\delta\right) - b f_R\right) \tag{3.61}$$

where V is the absolute vehicle velocity, β is the vehicle drift angle, Ω is the yaw rate, f_R and f_F are the normalized lateral forces, s_R and s_F are the normalized longitudinal forces and δ is the steer angle. Note that the lateral and longitudinal forces are normalized with the weight Mg. Note that the absolute velocity V and drift angle β are used in place of the longitudinal velocity u and lateral velocity v which are often used instead. The reason is that in limit handling condition (that we want to study with this model) the two differ substantially (e.g. on a $90deg$ drift u is null) and the absolute V is the one the driver aims to control.
The choice of the driven axle can be done by the user throughout some parameters thus in the general formulation equilibria equations must be considered for both axles.
These are expressed using the following equations of motion:

$$\dot{\omega}_R = \frac{\left(\gamma_R + h_b - r\, s_R\right) M\, g}{I_M} \tag{3.62}$$

$$\dot{\omega}_F = \frac{\left(\gamma_F - r\, s_F\right) M\, g}{I_M} \tag{3.63}$$

where γ_r and γ_f are the rear and front axle propulsive/braking torques, h_b is the handbrake torque (that engages rear wheel only), ω_R and ω_F are rear and front wheel spin velocities respectively.
Normalized vertical loads on the front and rear axle are computed from the vertical and pitch equations of motion which are solved to give:

$$n_{R0} = \frac{a}{a+b} + \frac{h\left(s_F \cos\delta - f_F \sin\delta + s_R\right)}{a+b} \tag{3.64}$$

$$n_{F0} = \frac{b}{a+b} - \frac{h\left(s_F \cos\delta - f_F \sin\delta + s_R\right)}{a+b} \tag{3.65}$$

where h is the height of the center of mass from the ground. To introduce time lag due to suspension dynamics the current vertical loads are computed from relaxation equations:

$$\tau_N \dot{n}_R + n_R = n_{R0} \tag{3.66}$$

$$\tau_N \dot{n}_F + n_F = n_{F0} \tag{3.67}$$

where τ_N approximates the non-instantaneous load transfer related to suspension dynamics.
Tire forces depend on longitudinal slip κ, lateral slip λ and tire vertical load n.
Rear and front (practical) longitudinal slip κ_R and κ_F as well as (practical) rear and front lateral

slip λ_R and λ_F are defined as follows:

$$\kappa_R = \frac{\omega_R\, r - V\cos\beta}{V\cos\beta} \tag{3.68}$$

$$\kappa_F = \frac{\omega_F\, r - V\cos(\beta-\delta) - \Omega\, a\, \sin\delta}{V\cos(\beta-\delta) + \Omega\, a\, \sin\delta} \tag{3.69}$$

$$\lambda_R = -\arctan\left(\frac{-\Omega\, b + V\sin\beta}{V\cos\beta}\right) \tag{3.70}$$

$$\lambda_F = -\arctan\left(\frac{V\sin(-\delta+\beta) + \cos\delta\, \Omega\, a}{V\cos(-\delta+\beta) + \sin\delta\, \Omega\, a}\right) \tag{3.71}$$

This particular model has been thought with the aim of employing coupling between longitudinal and lateral forces. Thus Coupled Pacejka model described above in section 2.2.2 applying the Similarity Method described in [10] Ch.3 is linked herein. As already shown, the theoretical longitudinal slip σ_x, lateral slip σ_y and equivalent slip σ are computed from the practical slips κ and λ:

$$\sigma_x = \frac{\kappa}{1+\kappa} \qquad \sigma_y = \frac{\tan\lambda}{1+\kappa} \qquad \sigma = \sqrt{{\sigma_x}^2 + {\sigma_y}^2} \tag{3.72}$$

and used to compute the lateral μ_f and longitudinal μ_s tire friction coefficient:

$$\mu_f = \frac{\sigma_y}{\sigma} D_\lambda \sin[C_\lambda \arctan\{\sigma B_\lambda - E_\lambda(\sigma B_\lambda - \arctan\sigma B_\lambda)\}] \tag{3.73}$$

$$\mu_s = \frac{\sigma_x}{\sigma} D_\kappa \sin[C_\kappa \arctan\{\sigma B_\kappa - E_\kappa(\sigma B_\kappa - \arctan\sigma B_\kappa)\}] \tag{3.74}$$

necessary to compute the steady-state tire longitudinal $s_{R,F}$ and lateral $f_{R,F}$ forces:

$$s_{R0} = n_R\, \mu_{s_R}(\lambda_R, \kappa_R) \qquad s_{F0} = n_F\, \mu_{s_F}(\lambda_F, \kappa_F) \tag{3.75}$$

$$f_{R0} = n_R\, \mu_{f_R}(\lambda_R, \kappa_R) \qquad f_{F0} = n_F\, \mu_{f_F}(\lambda_F, \kappa_F) \tag{3.76}$$

B, C, D, E being the well known Pacejka coefficients.
Current longitudinal and lateral forces are computed from steady-state values using the widespread relaxation equations:

$$\frac{\sigma_r\, \dot{f}_R}{V\cos\beta} + f_R = f_{R0} \tag{3.77}$$

$$\frac{\sigma_r\, \dot{f}_F}{V\cos\beta} + f_F = f_{F0} \tag{3.78}$$

$$\frac{\sigma_r\, \dot{s}_R}{V\cos\beta} + s_R = s_{R0} \tag{3.79}$$

$$\frac{\sigma_r\, \dot{s}_F}{V\cos\beta} + s_F = s_{F0} \tag{3.80}$$

where σ_r is the relaxation length both for lateral and longitudinal forces. This last account for the distance that a tire have to travel to generate the lateral or the longitudinal force, and it's a value coming from tire measurements.
Summarizing, the vehicle model consists of 14 differential equations Eq. (3.59-3.63,3.66-3.67,3.77-3.80,1.62-1.64) and as many state variables:

$$\mathbf{x} = \{V, \beta, \Omega, \omega_R, \omega_F, f_R, f_F, s_R, s_F, n_R, n_F, s_s, s_n, \alpha\}^T \tag{3.81}$$

Road states and equations have been included in the formulation following the mathematical approach introduced in section 1.3.1.

$$\dot{s}_s = \frac{V\cos(\alpha+\beta)}{1-s_nK} \tag{3.82}$$

$$\dot{s}_n = V\sin(\alpha+\beta) \tag{3.83}$$

$$\dot{\alpha} = \Omega - K\frac{V\cos(\alpha+\beta)}{1-s_nK} \tag{3.84}$$

The control vector consists of three elements:

$$\mathbf{u} = \{\delta, h_b, \gamma_t\}^T \tag{3.85}$$

where δ is the steer angle, h_b is the handbrake torque (normalized by the total weight Mg) on the rear axle wheels and γ_t is the total driving or pedal braking torque (normalized by the total weight Mg) which is split between the rear and front axle according to the torque distribution factor k_t:

$$\gamma_R = k_t\gamma_t \qquad \gamma_F = (1-k_t)\gamma_t \tag{3.86}$$

In addition a rear brake torque saturation is included in the formulation to account for the effect of the proportioning valve mounted on many rally vehicles (to avoid tires locking on one of the two axles during pedal braking) [12], [13]. This valve can be used to saturate either front or rear brake effort. In the vehicle used for experimental tests the saturation is on the rear and therefore the modeling reads:

$$\gamma_R = \max(k_t\gamma_t, \gamma_{R_{min}}) \tag{3.87}$$

3.2.1 Multiple steady-states computation

Even though single-track vehicle models are relative simple they are still capable of exploiting complex maneuvers if tire-ground interaction is properly described. Before starting to employ this kind of vehicle in dynamic simulations a set of steady-states calculations have been performed.
The target is to study the behavior of the system when pushed to critical conditions such as aggressive maneuvers.
Single states calculations for this vehicle do not present particular numerical issues inside the linear region of tires, whereas when trying to push the single-track to travel in steady-turning conditions (i.e. constant curve radius and state variables) at aggressive vehicle drift and side-slip angles computational problem occur most of the time.
For this reason a particular approach has been followed in the calculation of these "aggressive" states. The final desired state is not immediately computed but it is "reached" starting from a simple solution at low vehicle drift and side-slip angles, whom first guess solution can be simply calculated or assumed, and then changing drift angle step by step until the "aggressive" desired value is reached.
From the computation of the following steps, the initial guess solution is assumed to be equal to the previous calculated state. In this way even "aggressive" high vehicle drift and side-slips states can be computed.
Since experience suggests that on low adherence grounds aggressive maneuvers can be triggered with a low driver effort, it has been chosen low adhesion coefficient for both lateral and longitudinal tire-ground interactions. Non linear-tire and coupling between lateral and longitudinal forces are necessary to exploit this kind of states.
Set-up parameters are reported in Tab.3.1.

Table 3.1: Pacejka tire parameters.

Low	adherence	-	asphalt
B	7.0	D	0.6
C	1.8	E	0.0

Vehicle parameters are those that will be used for the studies presented in the next sections and are reported in Tab.3.2.
It is important to notice that a FWD (i.e. Front Wheel Drive) vehicle has been assumed for states computations.
Three different sets of multiple steady-states are presented, each solution is computed at low speed of 3 m/s at different imposed vehicle drift angle.
The choice of this low value of the vehicle absolute speed V is related to the fact that at this velocity condition two different completely opposite maneuvers can be computed through steady-states: the parking maneuver and the drift maneuver. The first one is characterized by high positive vehicle drift angles β following the convention shown in Fig.3.6 and always positive steer angles δ (i.e. wheels turned inward the curve), the latter is more complicated, it presents even very high negative drift angles with a steer that can reach negative values as well (i.e. counter-steering).
In [14] E.Velenis shows the possibility of reaching "aggressive" steady-state conditions for a RWD (i.e. Rear Wheel Drive) vehicle through stabilization methods. This suggest that steady-

Table 3.2: Parameters of the vehicle model.

Parameter	Symbol	Value	Unit
Gravity	g	9.81	m/s^2
Mass	M	1300	kg
Total yaw inertia	I_G	2000	$kg\ m^2$
Height of CoM	h	0.50	m
Distance of CoM from rear	b	1.53	m
Distance of CoM from front	a	0.96	m
Axle inertia	I_M	1.8	$kg\ m^2$
Wheel radius	r	0.28	m
Drag coefficient ($\frac{1}{2}\rho C_x A$)	K_D	0.2107	kg/m
Propulsive torque ratio (FWD)	k_t	0	
Braking torque ratio	k_t	0.4	
Braking torque saturation	$\gamma_{R_{\min}}$	-0.028	

states at critical stability conditions are possible and interesting for future vehicle dynamics studies as it will be shown later on.
In this chapter it is not considered how to enter into these states driving the vehicle but simply their computation is investigated.
The first case is the parking maneuver condition. Starting from $\beta = 0\ rad$ states are computed until reaching $\beta = 0.80\ rad$ ($45\ deg$) with a step size of $0.05\ rad$.
Vehicle transition through the different steps is presented in Fig.3.7, where V is the absolute speed of the single-track vehicle.

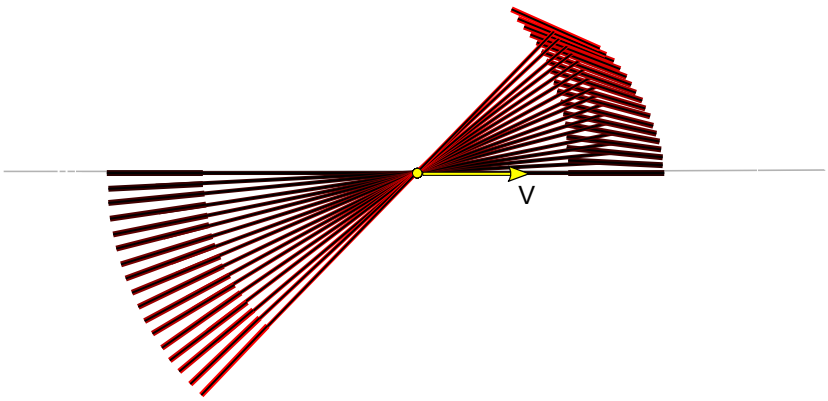

Figure 3.7: Vehicle representation in multiple steady-state, parking maneuver condition.

When observing the steer angle δ (Fig.3.8) it can be noticed that is always inward the curve

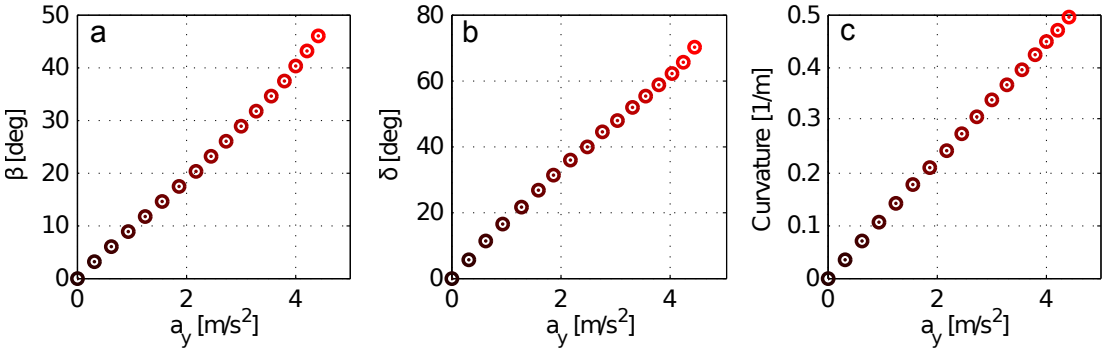

Figure 3.8: Observed variables representation in multiple steady-state in parking maneuver condition with respect to lateral acceleration a_y. (a) vehicle drift angle β, (b) steer angle δ, (c) path curvature.

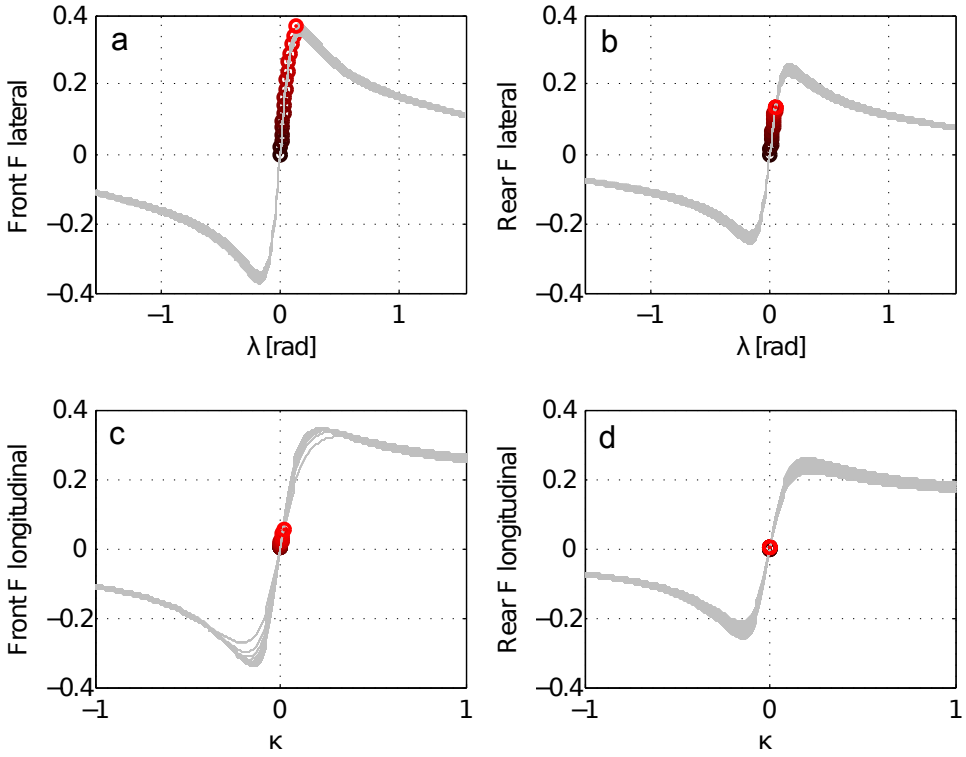

Figure 3.9: Tire forces representation in multiple steady-state in parking maneuver condition.

and it reaches really high values (even unreal for standard cars) of about 70 deg for the limit condition computed.
The vehicle is performing a steering pad of small radius as confirmed by the curvature diagram that shows values between $0 - 0.5\ 1/m$ and corresponds to curves of radius that reach a lower limit of $2m$.
As expected tires are not employed beyond their peak of lateral and longitudinal tire-ground interaction forces.
Fig.3.9 shows the different states conditions on their current tire curve, that as explained in section 2.2.2 depends on the simultaneous presence of lateral and longitudinal interactions.

The second case is the drift maneuver condition. The drift angle for the first computed state is $\beta = -0.1\ rad$ $(-6\ deg)$ and it is varied with a step size of $0.05\ rad$ until $\beta = -0.70\ rad$ $(-40\ deg)$.
Vehicle transition presented in Fig.3.10, and observed variables in Fig.3.11 reveal that the first state is a low vehicle drift one with steer angle δ inward the curve. In the followings, as the drift angle β grow up until its negative limit the steer angle δ gradually decreases until reaching null even positive values that denote counter-steering condition.

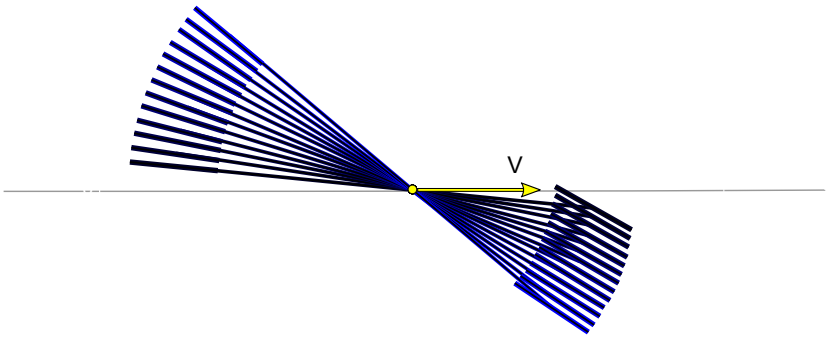

Figure 3.10: Vehicle representation in multiple steady-state, drift condition.

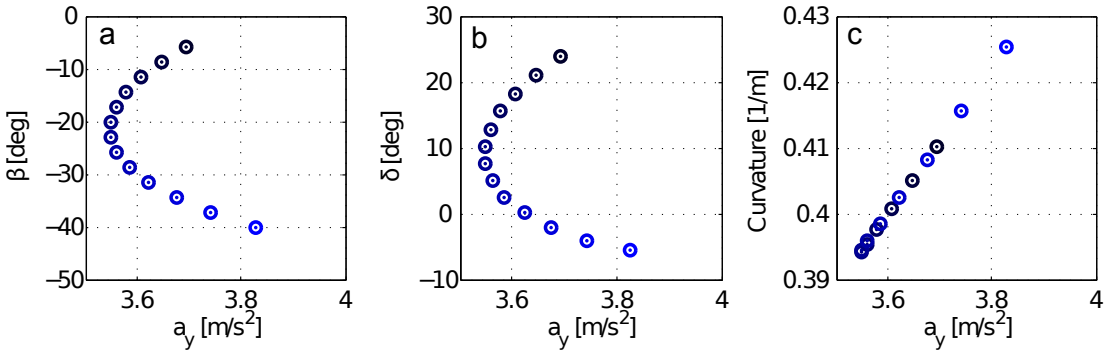

Figure 3.11: Observed variables representation in multiple steady-state in drift condition with respect to lateral acceleration a_y. (a) vehicle drift angle β, (b) steer angle δ, (c) path curvature.

Curvature diagram shows that the vehicle is always traveling on a curve of radius from $2.3 - 2.6\ m$, thus still a tight one, and at about $4\ m/s2$ of lateral acceleration (a_y).
Fig.3.12a shows as the front tire is laterally employed beneath its peak of force (i.e. its limit of side-slip for linear behavior), whereas rear tire is laterally skidding (Fig.3.12b) since the first step state as revealed by transitions through states shown on the tire diagram.
The third case is a sort of hybrid solution between the other presented above. It has to be noticed how for an imposed absolute velocity V and a vehicle drift angle β different solutions are acceptable, they mainly depends on the first guess that is provided and on which state

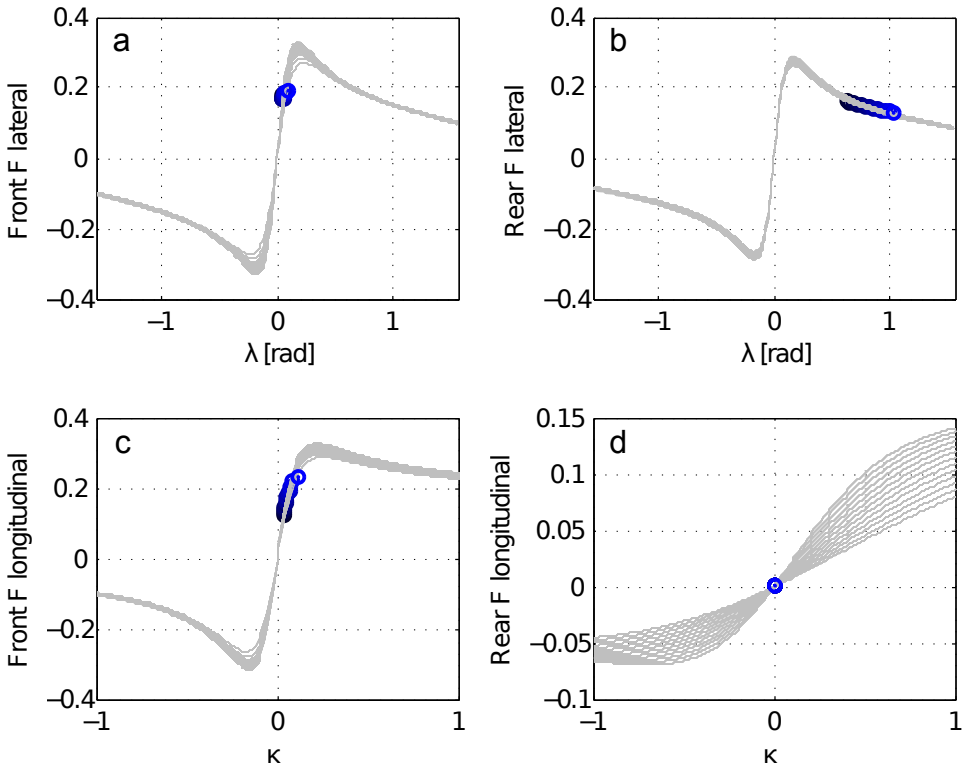

Figure 3.12: Tire forces representation in multiple steady-state in drift condition.

solution that fulfill the imposed tolerance is first computed.
In the previous case the state corresponding on $V = 3\ m/s$ and $\beta = -11.5\ deg$ has been computed starting from another state ($V = 3\ m/s$, $\beta = -8.5\ deg$, $\delta = 22\ deg$, etc.) and it revealed a certain steer angle of about $\delta = 18\ deg$ and curvature of about $c = 0.4\ 1/m$ (Fig.3.11). Now the same state represents the starting point and it has been computed from an initial guess in which for example $\delta = 0\ deg$.

In this case the steer angle is found to be $\delta = 47\ deg$ for more or less the same previous curvature $c = 0.4\ 1/m$ (Fig.3.14).
These two solution for the same steady-state input are possible only if the conditions of tire engagement are deeply different.
As shown in Fig.3.15a in this latter case the front tire is engaged with an high longitudinal slip, this causes a strong reduction in the front lateral force (Fig.3.15c) that allow the front wheel to skid laterally even without exceeding the peak of the lateral force itself.
In the drift case the same state, presented lower longitudinal and lateral slips at the front tire, that because of its lower steer angle could travel almost in free rolling conditions.
These preliminary study represents a starting point for further dynamic simulations involving aggressive maneuvers that will be presented later on.

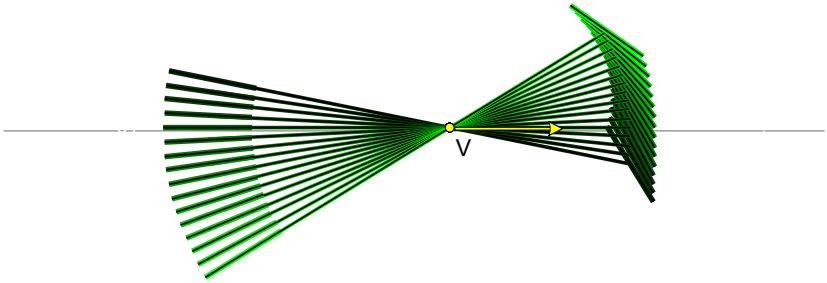

Figure 3.13: Vehicle representation in multiple steady-state, hybrid driving condition.

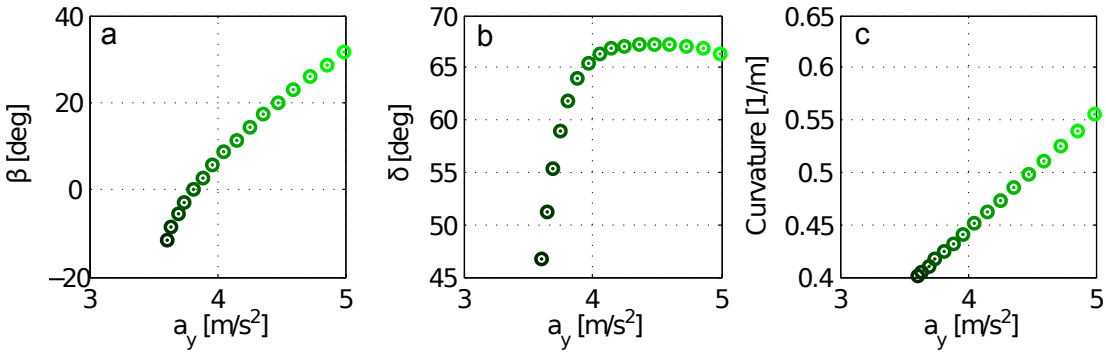

Figure 3.14: Observed variables representation in multiple steady-state in hybrid driving condition with respect to lateral acceleration a_y. (a) vehicle drift angle β, (b) steer angle δ, (c) path curvature.

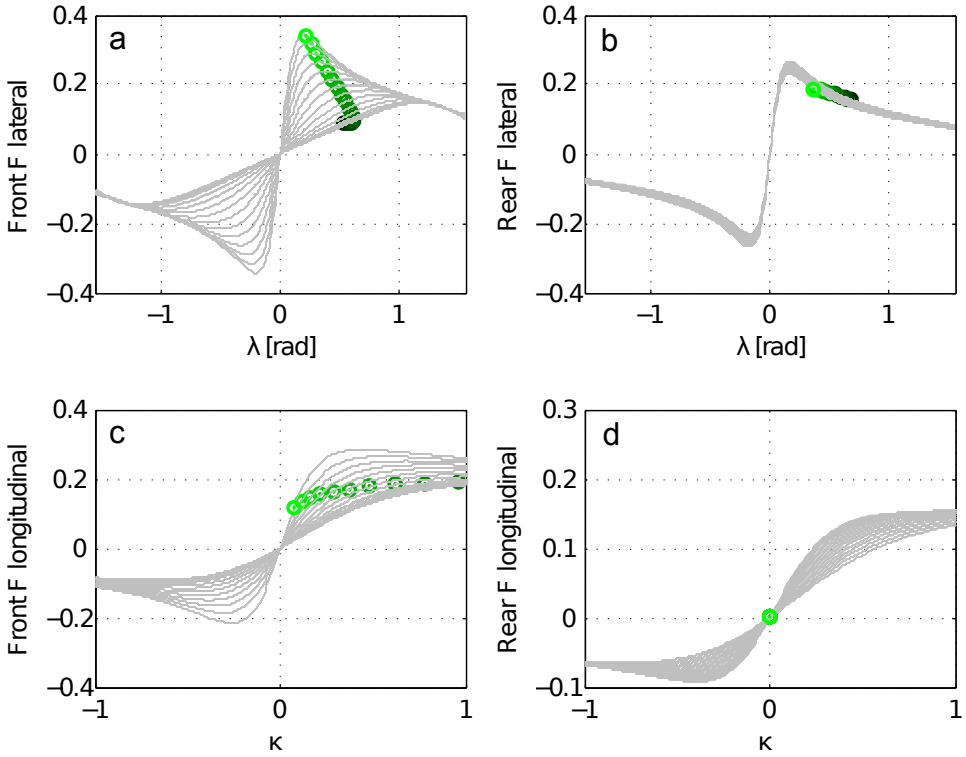

Figure 3.15: Tire forces representation in multiple steady-state in hybrid driving condition.

3.3 Minimum time cornering: the effect of road surface and car transmission layout

3.3.1 Introduction

In recent years there is a growing interest in the investigation of the so-called aggressive maneuvering (see e.g. [14], [6], [15]), following the idea that high drift and even counter-steering maneuvers may be more efficient than typical low drift maneuvers under certain road-tire characteristics and vehicle layout. In particular, experimental evidence shows that rally drivers are used to such maneuvers, thus suggesting that under low friction conditions this driving strategy could be even optimal from the minimum time point of view. In addition, a better understanding of such limit handling conditions could lead to advanced Electronic Stability Control (ESC) systems with an extended operating envelope.

As an experimental example of aggressive maneuvers by expert drivers, Fig. 3.16 shows a RWD car performing a $180deg$ turn on off-road surface. The recorded maneuver starts with the car traveling at a speed $V = 67kph$ in straight motion. After $0.25s$ (between the first two snapshots of the trajectory plot) the driver starts braking (still in straight motion) and after $1.25s$ (between the third and fourth snapshots) he steers inward the curve (negative δ) while still braking. At $3s$ (seventh snapshot) the driver throttles on and steers outward the curve (positive δ, counter-steering). The minimum speed of $26kph$ and maximum vehicle drift/slip angle $\beta = 25deg$ are reached at $4s$ (ninth snapshot). From here on the driver accelerates while exiting the curve. The steering angle is rather vibrating and can be noted that full throttle phases are associated with counter-steering phases.

On the other side, an experimental example of low vehicle drift maneuver is reported in Fig. 3.17, where a FWD car performs a $180deg$ turn on a paved track. Similar to the previous case,

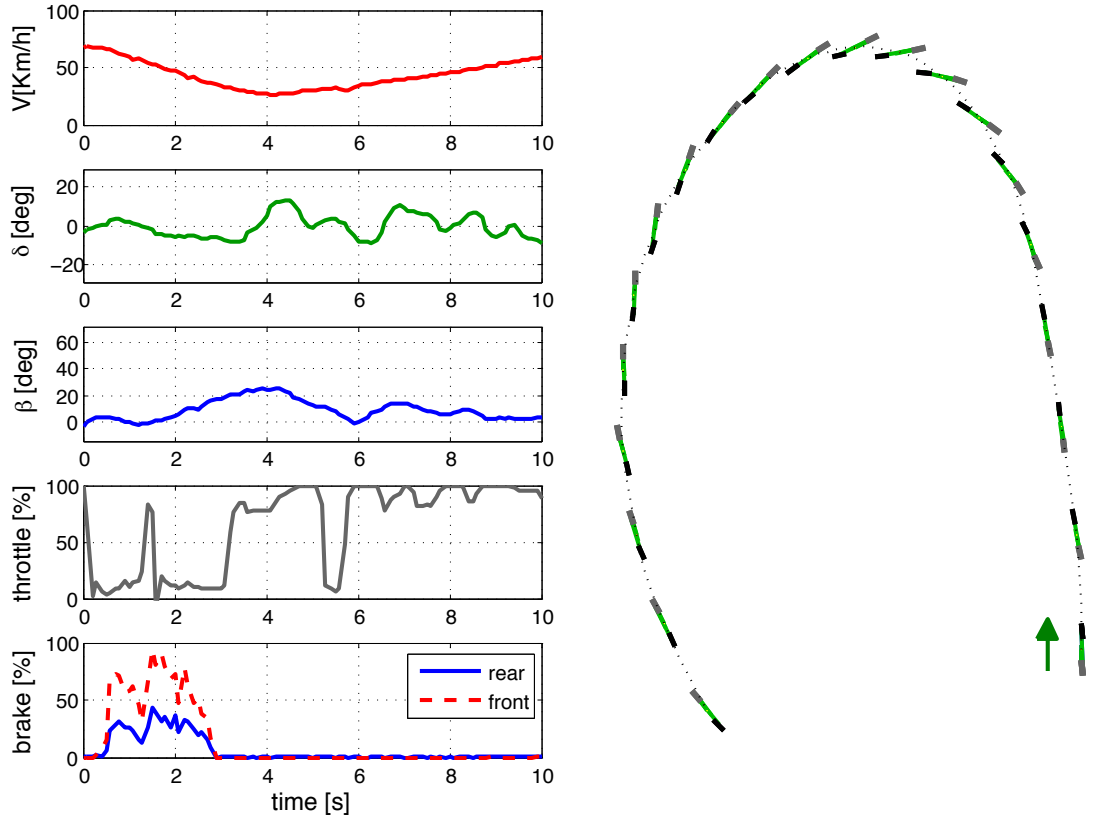

Figure 3.16: Experimental data of a RWD car performing a $180deg$ curve on a off-road surface. The trajectory snapshots are with $0.5s$ time increment. From [16].

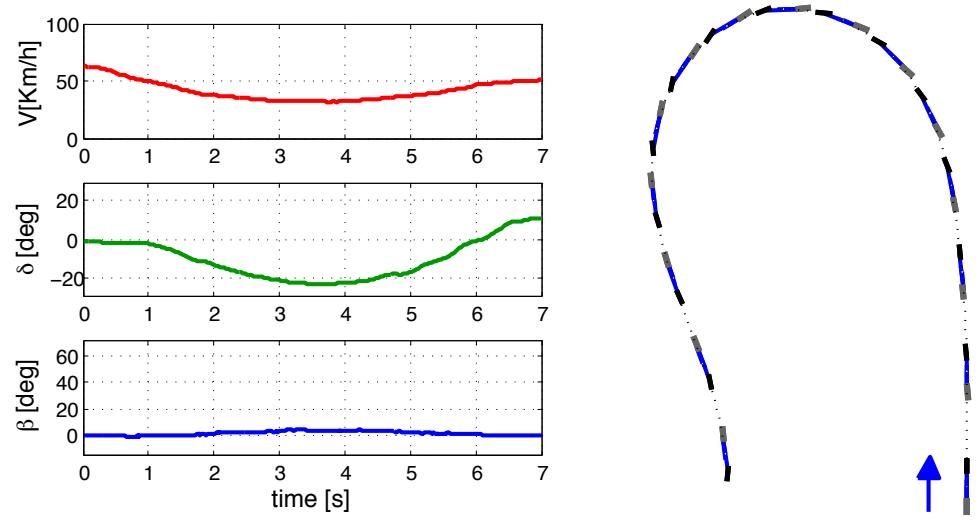

Figure 3.17: Experimental data of a FWD car performing a $180deg$ curve on paved track. The trajectory snapshots are with $0.5s$ time increment. From [16].

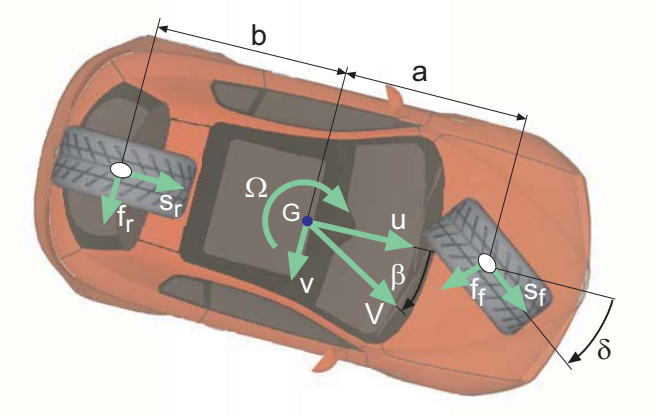

Figure 3.18: Car model with variables. From [16].

the recorded maneuver starts with the car in straight motion at a speed of $63kph$. The driver starts braking and at $1s$ (second snapshot) he steers inward the curve. The steer is kept inward the curve (negative δ) all along curve, with a peak value of $22deg$ at $4s$ (eighth snapshot). The vehicle drift β remains low ($< 5deg$). Nevertheless the lateral acceleration reach $0.9g$, i.e. the maneuver is quite demanding (it is a C-segment medium car driven by an expert driver).
The present work addresses the optimality of cornering maneuvering through the use of nonlinear optimal control techniques. The control problem is defined as follows: find the minimum time 'optimal' maneuver (in terms of vehicle states, trajectory and control inputs) given the car characteristics, tire-road characteristics, road geometry and driver limitations (control bandwidth and magnitude). The resulting nonlinear optimal control problem is solved using the indirect method detailed in [9].
Driver's input are limited in frequency and magnitude to reproduce real drivers limitations [17].
The method has been used successfully in the past for minimum time maneuvering of motorcycles [1, 3]. Similar approaches on minimum time maneuvering are reported in [5, 7] (based on direct methods) and [18] (limited to constant speed).
The car model employed herein is based on the well known single-track model formulated in section 3.2 and introduced by Segel in [19] and included in most vehicle dynamics textbooks, e.g. [10, 20]. The model has been enriched with nonlinear tires, coupling between longitudinal and lateral tire forces [21] as well as longitudinal load transfer. In [6] the capability of this simple model to reproduce complex and aggressive maneuvers consistent with experimental data is shown.
The work is organized as follows. In section 3.4.3 the mathematical formulation of the problem is presented, in section 3.4.4 the effect of road condition on road/tire characteristics are discussed, and finally in section 3.4.5 the minimum time simulations with different road-tire characteristics and vehicle layout are presented.

3.3.2 Mathematical formulation

Vehicle model

A single-track model including nonlinear tires and front/rear load transfer is employed and shown in Fig.3.18.
The model has been described in section 3.2 with the exception that the handbrake command has been unable and is not compute as an input of the system.

Optimal control

Optimal control aims at minimizing a certain cost function subject to a certain number of equality and/or inequality constraints.
In this case the cost function is the total maneuver time T, while the vehicle equations of motion are included in the optimization as equality constraints:

$$\mathbf{f}\left(\mathbf{x}, \dot{\mathbf{x}}, \mathbf{u}\right) = 0 \tag{3.88}$$

where $\mathbf{f}$ consists of Eq. (3.59-3.63,3.66-3.67,3.77-3.80,1.62-1.64), $\mathbf{x}$ is the state vector reported in Eq. (3.141) and $\mathbf{u}$ are the driver controls of Eq. (3.145).
Since the maximum steering angle on vehicles is limited to a certain $\delta_{\max}$, a corresponding inequality constraint is added as follows:

$$\delta \leq |\delta_{\max}| \tag{3.89}$$

To include the limited bandwidth of real drivers, also the maximum steer angle rate is limited to $\dot{\delta}_{\max}$:

$$\dot{\delta} \leq \left|\dot{\delta}_{\max}\right| \tag{3.90}$$

A similar bandwidth limitation is added to the whole propulsive/braking torque, i.e. to the driver throttling/braking actions:

$$\dot{\gamma}_t \leq |\dot{\gamma}_{t_{\max}}| \tag{3.91}$$

To account for the limited engine power, another inequality constraint is added, stating that the whole propulsive torque (rear axle plus front axle) is limited:

$$\left(\gamma_t k_t \omega_R + \gamma_t \left(1 - k_t\right) \omega_F\right) Mg \leq P_{\max} \tag{3.92}$$

In order to constraint the vehicle trajectory within the road boundaries the following inequality constraints are added:

$$-L_w \leq s_n - b \sin\alpha \leq R_w \tag{3.93}$$
$$-L_w \leq s_n + a \sin\alpha \leq R_w \tag{3.94}$$

where R_w and L_w are right and left road widths respectively.
Initial and final conditions, e.g. vehicle velocities and positions on the road at the start and finish line given by:

$$\mathbf{b}_1\left(\mathbf{x}\left(0\right), \mathbf{u}\left(0\right)\right) = 0 \qquad \mathbf{b}_2\left(\mathbf{x}\left(T\right), \mathbf{u}\left(T\right)\right) = 0 \tag{3.95}$$

The result of the optimal control problem completely describes both the dynamics of the vehicle system during the maneuver and the driver inputs that produce it. One of the main advantages of this method is that no driving rules have to be predefined.

Table 3.3: Pacejka tire parameters.

tire 1			
B	6.8488	D	1.0
C	1.4601	E	-3.6121
tire 2			
B	11.415	D	0.6
C	1.4601	E	-0.20939
tire 3			
B	15.289	D	0.6
C	1.0901	E	0.86215
tire 4			
B	1.5289	D	0.6
C	1.0901	E	-0.95084

Road-tire interaction

Nowadays measuring the tire properties in terms of forces/torques as a function of slips is a consolidated procedure among car and tire manufacturers. Nevertheless, it is worth to remember that what is measured is not the absolute tire response, rather the response of the tire on the specific tested surface is measured. In other words the same tire behaves differently on different road surfaces. However, experience highlighted some general patterns, see e.g. [20, 22]. In particular, when using the same tire on different road asphalts, the cornering stiffness keeps almost unchanged while there may be changes on the friction peak coefficient. Even when moving to wet asphalt (in non hydroplaning condition) the cornering stiffness does not change significantly while the friction peak is greatly reduced. In practice, as long as the ground surface can be considered rigid with respect to the tire carcass, the tire has basically the same cornering stiffness (as predicted by theoretical brush and string models in [10] Ch.3,5). It follows that when off-road surfaces are considered (e.g. gravel), the ground cannot be considered rigid with respect to the tire, and a reduction on the cornering stiffness is therefore expected. In [23, 24] it is highlighted that the changes in the tire force vs slip curve are in the direction of a reduction of the cornering stiffness, while in [25] it is shown that the peak of the lateral force moves towards high slips and even disappears (in very soft surfaces a bulldozing effect related to the plowing of the soil may even take place). The same adjustments characterize the curve of longitudinal forces vs longitudinal slip [24].
In the current work, four types of tire-road interaction curves named tire1, tire2, tire3, tire4 are considered and simulated to evaluate their effect on optimal driving strategies. They are obtained by varying the Pacejka coefficients B, C, D, E, see Tab.3.6 (same values are used for the lateral and longitudinal forces). In other words, we consider the same tire on different road surfaces.
The first tire-road characteristic (tire1, blue curve in Fig. 3.19) has a typical high adherence curve (e.g. dry paved road): the cornering stiffness and longitudinal stiffness are $10 rad^{-1}$, the friction peak value is 1 and is reached at a low slip value of 0.15.

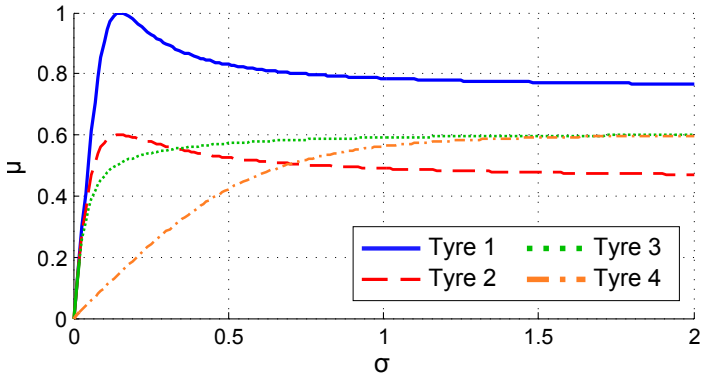

Figure 3.19: Tire-road friction coefficient μ as a function of the slip σ. From [16].

The second tire (tire2, red curve in Fig. 3.19) differs from the previous only by the friction peak value, which is reduced to 0.6, and can be considered typical of a wet paved road (no hydroplaning) or a reduced friction paved road.
The third (tire3, green curve in Fig. 3.19) corresponds to a tire on a dirt off-road surface: again the cornering/longitudinal stiffness is $10rad^{-1}$ (like tire1 and tire2), the maximum friction is 0.6 (like tire2) but it is reached at very high slip values, in other words there is no peak in the operating range of slips and the curve is monotonic.
The last curve, tire4 (orange curve in Fig. 3.19) is an extreme off-road curve (e.g. gravel), where the tire is rolling on a soft surface that contributes to the reduction of cornering/longitudinal stiffness, reduction in the maximum friction and absence of a visible peak in the force vs slip curve. The cornering/longitudinal stiffness is $1rad^{-1}$, the maximum friction is 0.6 (like tire2 and tire3) and is reached at very high slips (monotonic behaviour).
It is expected that typical off-road surfaces would be in between tire3 and tire4.

3.3.3 Simulations

The aim is to investigate how road surface (i.e. different tire-road curves) and transmission layout affect minimum time maneuver strategies. The simulations are performed on a classic maneuver for vehicle dynamics: the U-turn. In particular, a $180deg$ turn with a curvature radius of $10m$ (on the center line) connects two straight sections of $30m$. The road width is 10m.
The same vehicle is simulated with the four road-tire adhesion curves discussed in the previous section and with different transmission layout, namely Front-Wheel-Drive (FWD), Rear-Wheel-Drive (RWD) and All-Wheel-Drive (AWD). The transmission layout is simply changed by varying the parameter k_t of Eq. (3.86,3.101) in propulsive condition. In particular it is $k_t = 0$ in case of FWD, $k_t = 1$ in case of RWD and $0 < k_t < 1$ in case of AWD. In braking condition k_t is the same for all cases. The car parameters are reported in Tab.3.7.
Boundary conditions are the same for all the simulations: at the starting line the vehicle is going straight on the center of the road with a speed of $55kph$ while on the finish line the vehicle is only requested to go straight and parallel to the center line, see Tab.3.8 for a summary of initial and final conditions.
Minimum time optimal maneuvers in case of tire1 (paved dry) and different transmission layout are reported in Fig.3.20. All the three maneuvers are characterized by low vehicle drift ($\beta < 6deg$), low tire slips (indeed maximum friction coefficient is achieved at small slips) and the trajectories are those typical of racing cars on paved circuits, where the driver uses most of the available width of the road reaching the apex of the maneuver in the middle of the turn and

Table 3.4: Parameters of the vehicle model.

Parameter	Symbol	Value	Unit
Gravity	g	9.81	m/s^2
Mass	M	1300	kg
Total yaw inertia	I_G	2000	$kg\,m^2$
Height of CoM	h	0.50	m
Distance of CoM from rear	b	1.53	m
Distance of CoM from front	a	0.96	m
Axle inertia	I_M	1.8	$kg\,m^2$
Wheel radius	r	0.28	m
Drag coefficient ($\frac{1}{2}\rho C_x A$)	K_D	0.2107	kg/m
tire relaxation lenght	σ_r	0.50	m
Suspensions time-lag	τ_N	0.25	s
Propulsive torque distribution (FRW/RWD/AWD)	k_t	0/1/0.5	
Braking torque distribution	k_t	0.4	
Engine power	$P_{\max}$	110	kW

Table 3.5: Boundary conditions.

Variable	Initial B.C.	Final B.C.
V	55 kph	free
β	0	0
Ω	0	0
ω_R	trim	free
ω_F	trim	free
f_R	0	free
f_F	0	free
s_R	0	free
s_F	0	free
n_R	trim	free
n_F	trim	free
s_s	0	10π+60 m
s_n	0	free
α	0	0

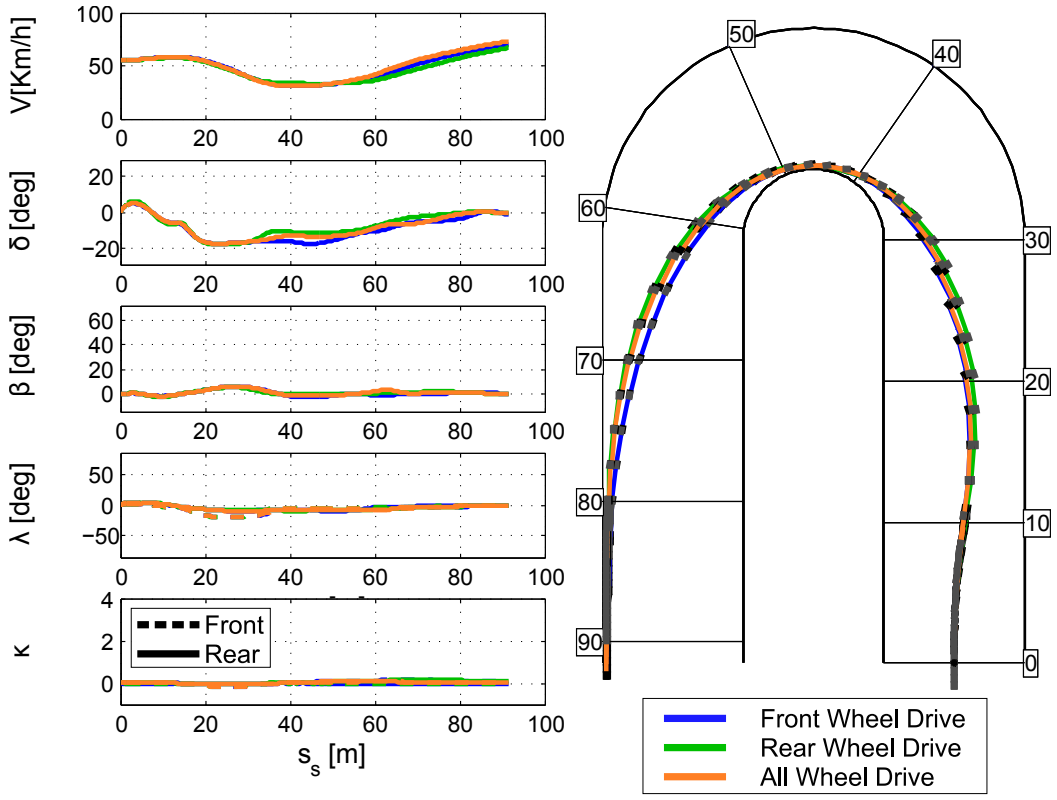

Figure 3.20: Simulations with tire1, high-adherence (paved dry). From [16].

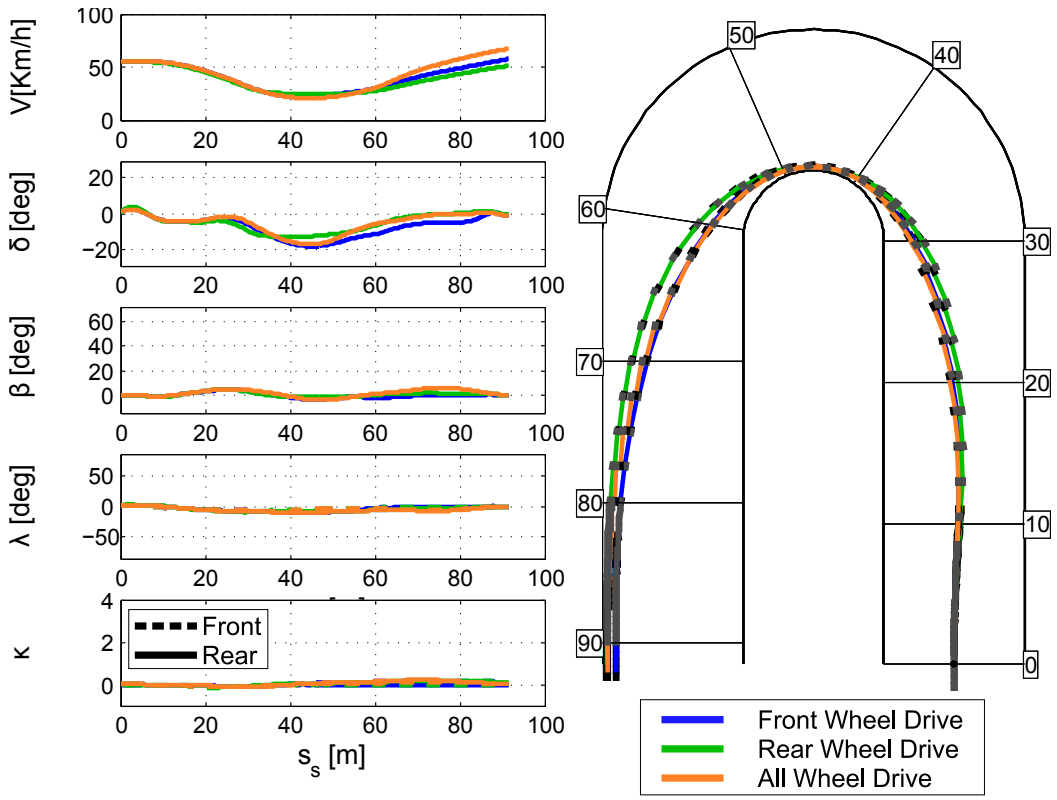

Figure 3.21: Simulations with tire2, low-adherence (paved wet). From [16].

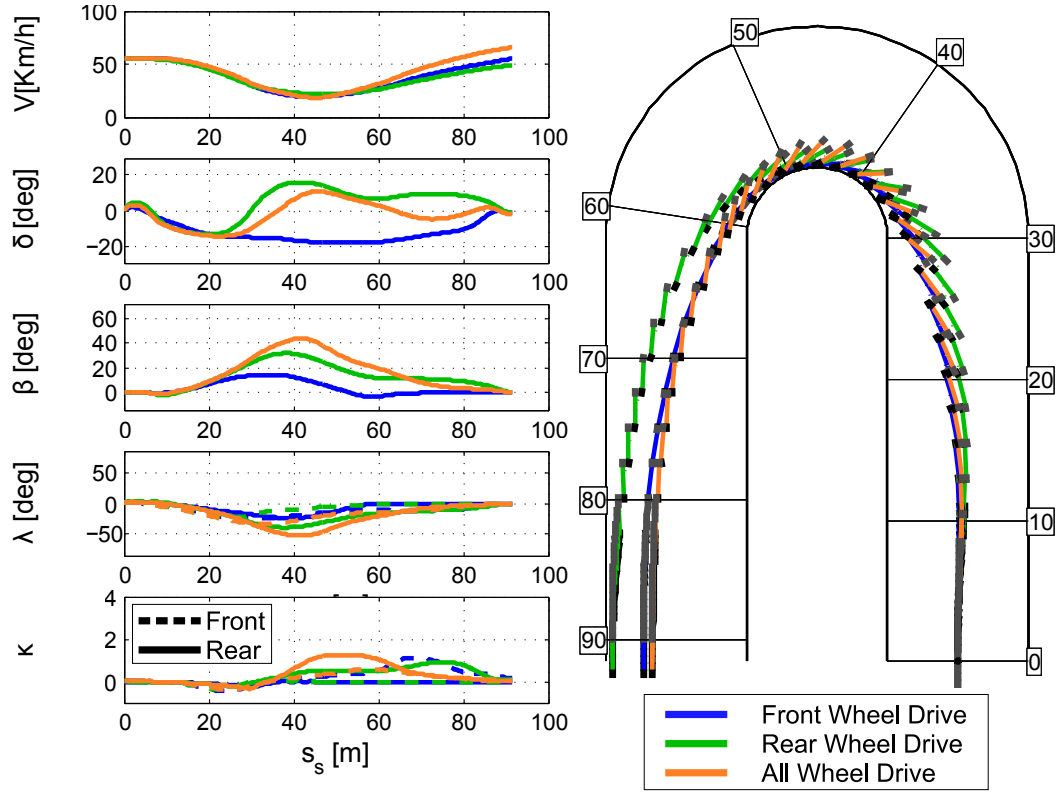

Figure 3.22: Simulations with tire3, off-road (dirt). From [16].

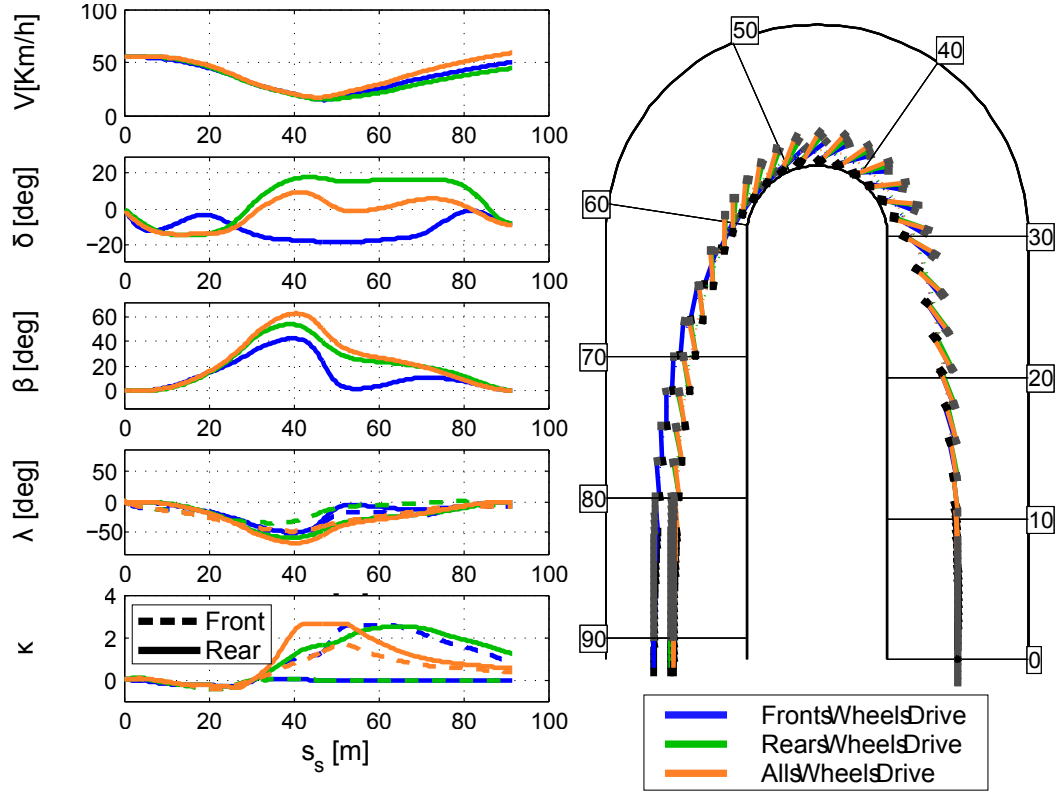

Figure 3.23: Simulations with tire4, extreme off-road (gravel). From [16].

exiting the curve close to the outer border.
The RWD vehicle travels on a wider path when comparing with the FWD, both when entering and exiting of the turn. The AWD trajectory is in between the two.
Under this road condition all the vehicles perform a sort of pendulum maneuver while entering the turn, to exploit the road width and reduce the vehicle trajectory curvature. After the pendulum the steer is always inward the curve (no counter-steering) and the tire slips remain on low values, close to the friction peak (no skidding).
The AWD has the minimum time of travel ($6.140s$), followed by the FWD ($6.223s$) and RWD ($6.510s$). It is expected that the AWD is the fastest (indeed the traction effort is distributed over the two axles), while the reason the FWD is faster than the RWD is mainly related to the fact that in the current vehicle the center of mass is shifted toward the front axle (static load distribution front to rear is $61/39$), thus giving a traction advantage to the FWD layout over the RWD. Also when comparing exit speeds, AWD ranks first ($73kph$), followed by FWD ($70kph$) and RWD ($67kph$).
Minimum time maneuvers for tire2 (paved wet) are depicted in Fig.3.21. Again they are characterized by low vehicle drift β, low tire slips κ, λ and resemble again the trajectories typical of racing cars on paved track. There are no relevant differences among different traction layout until the exit of the turn, where the RWD vehicle travels again on a wider path. The initial pendulum which characterized tire1 is significantly less pronounced. The steer is once again always inward the curve. The quickest maneuver is performed by the AWD ($7.375s$). Higher travel times are recorded for the FWD ($7.601s$) and RWD ($8.094s$). The same ranking holds for final speeds (AWD: $67kph$, FWD: $57kph$, RWD: $51kph$). As expected in all the cases with tire2 the traveling times are higher than those obtained with tire1 and the final speeds lower, due to the reduced friction peak coefficient.
When considering tire3 (loose off-road) some novelties appear. The minimum time maneuvers depicted in Fig.3.22 can be considered aggressive, with vehicle drift β up to $45deg$ for the AWD, $30deg$ for the RWD and $15deg$ for the FWD. The side-slip λ_R of the rear axle follows the same trend of the vehicle drift β. On the other hand the highest front axle slip λ_F is reached by the AWD, followed by the FWD and RWD. In particular, the front axle side-slip of the RWD is almost null during the whole curve ($s_s > 30m$).
It can be observed that in all three cases the trigger to the drift is the driver's steering action inward the curve while braking. This is consistent with the observations reported in [6] on the Trail-Braking technique used by rally drivers. In Trail-Braking the driver takes advantage of the forward weight shift during braking, which increases the over-steering behavior of the vehicle. In all cases the steer angle reaches a peak value close to $15deg$ inward the curve at $s_s = 25m$. Then, depending on transmission layout different strategies are adopted.
In the case of RWD and AWD the steer angle is reduced to zero (at $s_s = 30m$ and $s_s = 35m$ respectively) while the vehicle is still braking. When passing through the null steer angle condition the driver throttles on to enter a counter-steering power-slide drifting. In the case of FWD instead, the driver slightly increases the steer angle inward the turn and throttles on shortly after ($s_s = 38m$). No pendulum is present on the initial straight. Similarly to the previous cases, RWD exploits the whole road width while exiting the turn, although with significant drift values. On the contrary, AWD and FWD still exit the turn on similar trajectories, but this time they keep close to the road center line, even though with very different vehicle drift β (AWD is much more drifting then the FWD) throughout most of the maneuver ($25m < s_s < 75m$).
The inspection of the steer angle is even more interesting. While the FWD is consistently inward the curve (almost steady $17deg$ along the turn), the AWD is slightly outward the curve ($35 < s_s < 65m$) and the RWD is consistently outward the turn (counter-steering). The considerations on time of travel and finish speeds remain those of tire1 and tire2: the AWD is the

fastest with a travel time of $7.400s$ and speed of $66kph$, followed by the FWD ($7.860s$ and $55kph$) and RWD ($8.369s$ and $49kph$).
The last case corresponding to tire4 (extreme off-road) is reported in Fig. 3.23. The vehicle drift angles β denote aggressive maneuvers, and reaches values higher than $60deg$ for the AWD, above $50deg$ for the RWD and $40deg$ for the FWD, slightly before the middle of the turn ($s_s = 40m$). The maneuvers are somehow close to those reported for the loose off-road tire with the differences among different layouts amplified. The inspection of the steer angle reveals three markedly different behaviors: steer inward the curve for the FWD (almost steady $18deg$ for most of the turn), counter-steering for RWD (almost steady $16deg$ for most of the turn) and almost null/slightly counter-steering angle for the AWD (mean value $3deg$). In the case of RWD and AWD the drifting is again triggered by a steering action inward the curve while braking, and then reduced (null close to $s_s = 30m$) while throttling to a power-slide condition (markedly counter-steering for RWD and slightly counter-steering/null steer for AWD). FWD uses a slightly different strategy: it initially steers inward the turn, then temporary reduces the steer at $s_s = 20m$, then steers again inward the curve and accelerates like RWD and AWD from $s_s = 30m$ to reach an almost steady turning condition. This time, all three vehicles have exit trajectories far from the outer limit of the road and a kind of late-apex cornering strategy.
The late apex line corresponds to exiting the corner near the inner limit of the road. Rally driving involves limited knowledge of the road geometry and optimal braking points compared to the highly rehearsed closed circuit driving. The late apex trajectory is favored by rally drivers [26] as a safer approach to corners, to account for cases where they have miss-judged the braking point before the corner. If the driver is late in braking before the corner a wider trajectory through the corner is necessary to accommodate the higher entry speed. A driver aiming for a late apex line can afford a wider trajectory (still within the limits of the road) when carrying higher speed in the corner entry. It turns out that this approach is not only safer, but corresponds also to the minimum travel time strategy when the road is low friction and soft (with respect to the tire).
Summarizing, the minimum time optimal cornering maneuver is characterized by small vehicle drift and tire slip angles (paved track-like strategy) when the tire-road curve is characterized by a marked peak of the friction coefficient at low slip values, while is characterized by high drift and tire slip angles (rally-like strategy) when the tire-road curve is characterized by a monotonic friction vs slips curve (e.g. friction peak at very high slip values). The maximum friction coefficient itself is not sufficient to change the minimum time optimal maneuver from the low vehicle drift pattern to the high vehicle drift one.
In other words, aggressive maneuvers with high vehicle drift angles are minimum time optimal on off-road conditions, where the friction curve is monotonic or with the friction peak placed at very high tire slips, even outside the range of slips actually engaged. The effect of cornering stiffness is not as important as the position of the friction peak. In other words a reduction in the cornering stiffness amplifies the drifting behavior introduced by tire-road monotonic interaction typical of off-road condition.

3.3.4 Conclusions

A simple yet effective vehicle model has been described and used to investigate minimum time cornering strategies on different road surfaces with different transmission layout. The minimum time maneuver on asphalt surfaces is characterized by low vehicle drift angles and trajectories that resemble those of racing cars on paved track circuits, where the whole road width is exploited. When moving to off-road conditions, the minimum time maneuver is characterized by aggressive, high drift, even counter-steering (RWD,AWD) maneuvers and rally-like trajectories which keep the vehicle far from the outer border of the road.

3.4 The Optimality of the Handbrake Cornering Technique

3.4.1 Introduction

As explained in the previous section the investigation of operations in the nonlinear region of tires (sometimes referred as "aggressive maneuvering") is based on the idea that the related maneuvers may be more efficient than standard maneuvers under particular road geometry and adhesion conditions. A better understanding of such conditions could lead to advanced Electronic Stability Control (ESC) systems as well as autonomous vehicle able to exploit the nonlinear region of the tire [15].
Several papers on the topic appeared recently. In [27] the drifting of a Rear Wheel Drive (RWD) car is investigated through the analysis of experimental data and in [14] a stabilization control for drifting maneuvers of RWD cars is discussed. Trail braking cornering and pendulum-turn (other typical rally driving techniques) of All Wheel Drive (AWD) vehicles are studied in [6, 28] where nonlinear optimal control is used to reproduce such maneuvers as special cases of the minimum time cornering problem with specific boundary conditions. In [11] the handbrake cornering of a Front Wheel Drive (FWD) car is analyzed through experimental data and a stabilization control is devised. In [16] the minimum time cornering is investigated for different car transmission layout (RWD,FWD,AWD) and road surfaces (paved road, off road): it is shown that high-drift and even counter-steering maneuvers are optimal in off-road conditions.
Generally speaking, aggressive maneuvers like drifting, trail braking cornering pendulum turn and handbrake cornering are not a peculiarity of a particular type of vehicle: indeed they are widely used in rally races by different drivers driving different cars, with different transmission layout (i.e. FWD, RWD, AWD) and in different road conditions [26].
The present work aims at investigating the optimality of the handbrake cornering technique.

Figure 3.24: FWD test vehicle driven by a professional driver during data collection on a loose off-road surface.

This maneuver basically consists of braking (even locking) the rear axle in order to reduce the available lateral force (due to the tire lateral-longitudinal coupling [10]), thus exacerbating the

over-steering behavior of the vehicle, or inducing an over-steering behavior in a vehicle which is under-steering in normal driving. The subsequent rotation of the steering wheel provokes the skidding of the rear axle. Experimental observations shows that this technique is widely used to approach very tight low speed corners, e.g. low radius 'hairpin' turns, on different types of road surfaces (both paved and off-road).
Nonlinear optimal control techniques are used to reproduce handbrake maneuvers. As in the previous work in section 3.3 the control problem is defined as finding the "optimal" maneuver (i.e. the maneuver that minimizes the given performance criterion) in terms of vehicle states, trajectory and control inputs given the car characteristics, tire-road characteristics, road geometry and driver limitations (control bandwidth and magnitude). The resulting nonlinear optimal control problem is once more solved using the indirect method detailed in [9]. Driver's input are limited in frequency and magnitude to reproduce real drivers limitations [17].Similar approaches on minimum time maneuvering are reported in [5, 7] (based on direct methods) and [18, 29] (based on proper linearisation of the plant). However none of these works address highly nonlinear aggressive maneuvers.
The present work is organized as follows. In section 3.4.2 a typical handbrake cornering maneuver is described based on experimental data collected on a FWD car driven by a professional driver on an off-road surface. In section 3.4.3 the car model employed for simulations is described together with some details of the nonlinear optimal control formulation. In section 3.4.4 the characteristics of the tire-ground forces used for simulations are discussed. Section 3.4.5 contains the nonlinear optimal control simulations in off-road and paved asphalt road conditions and includes the comparison with the experimental data presented in section 3.4.2. Finally in section 3.4.7 a sensitivity analysis on some fundamental vehicle parameters, namely yaw inertia, center of mass position and friction properties, is presented. The analysis of the effect a variation in the inputs limits is also included.

3.4.2 Experimental data

This section contains the experimental data of a typical handbrake cornering maneuver. The same data will be compared with simulation results in section 3.4.5.
The data were collected at the Bill Gwynne Rally School in Brackley (UK) using the FWD car depicted in Fig.3.24. The vehicle velocity and drift (or vehicle slip) angle were measured using a Racelogic VBox twin GPS antenna sensor. An Inertial Measurement Unit (IMU) was used to measure 3-axis body accelerations and 3-axis body rotation rates. The rotational speed of each individual wheel and the throttle position were measured using the standard vehicle sensors and a CAN-bus interface to collect the data from the vehicle's Engine Central Unit (ECU). The vehicle was also fitted with a potentiometer to measure the steering angle and two brake pressure sensors to measure the brake pressure at the front and rear wheels. The handbrake was integrated in the hydraulic brakes circuit and engage the rear brakes only. Hence, the inspection of the two brake sensors allowed to distinguish between application of foot brake and handbrake. Additional details on the data logging procedure and instrumentation are available in [30].
Fig.3.25 and Fig.3.26 report the data of a counter-clockwise handbrake cornering maneuver. At $t = 0$ the car is traveling at $37kph$ in straight motion. The driver immediately starts rotating the steering wheel inward the curve (blue dashed line in Fig.3.25b) and applies the handbrake at 0.7 s thus engaging only the rear axle wheels, see Fig.3.25c which shows that only the rear brake pressure increases (solid blue line) while the front brake pressure (dashed red line) remains null. The handbrake is kept until 2.1 s. As a consequence the spin velocities of the rear tires reduce abruptly. In particular the rear-left (i.e. inner) tire ω_{RL} (solid blue line in 3.25a)

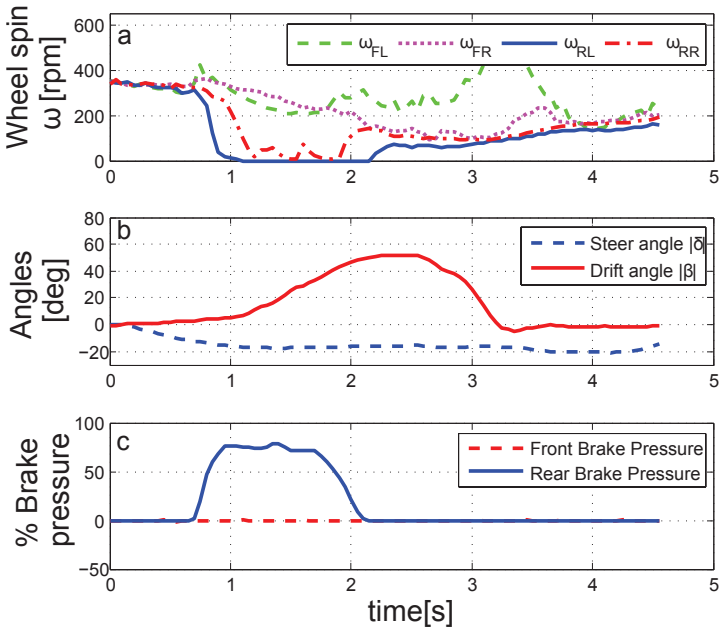

Figure 3.25: Experimental handbrake cornering data of the FWD test vehicle on a loose off-road surface. (a) Wheel spin signals ω are from the vehicle standard sensors, (b) steering angle δ is from an additional potentiometer, vehicle slip/drift angle β is from Racelogic VBox twin GPS antenna sensor, (c) brake pressures are from two additional pressure sensors.

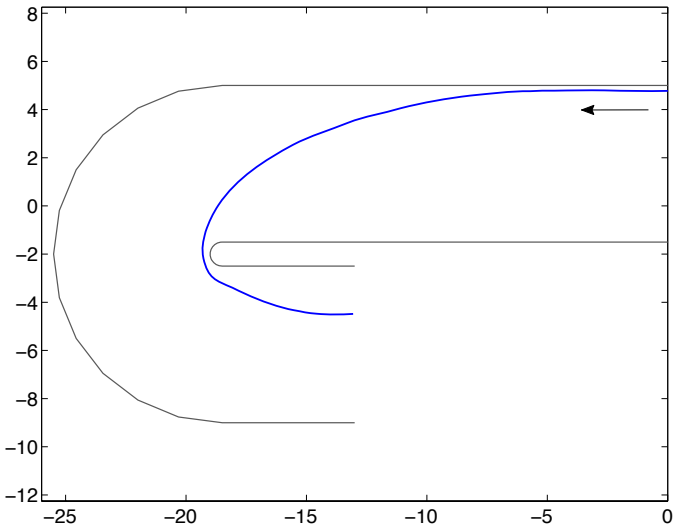

Figure 3.26: Experimental handbrake cornering data of the FWD test vehicle on a loose off-road surface. Trajectory is from Racelogic VBox twin GPS antenna sensor.

locks at $t = 1\,\mathrm{s}$ while the rear-right (i.e. the outer) tire ω_{RR} (dash-dotted red line in 3.25a) approaches locking. A reduction on the spin velocities of the front axle tires ω_{FL}, ω_{FR} is observed, as a consequence of the reduction in the car speed induced by rear axle braking forces. The handbrake reduces the available lateral forces on the rear tire and induces an over-steering behavior in the vehicle. The steering command of the driver triggers the skidding of the rear axle confirmed by the quick increase of the vehicle drift angle which reaches a peak value

of 50 deg at 2.5 s (solid red line in 3.25b). Note that the steering angle is inward the curve all along the maneuver (no counter-steering) and is almost constant and close to 20 deg for $t > 1$ s. Furthermore the foot brake is never applied by the driver.

3.4.3 Mathematical formulation

Vehicle model

The car model employed herein is the single-track vehicle model with nonlinear tires characteristics and fore/aft load transfer shown in Fig. 3.18. For each axle the wheel includes the contribution of the left and the right wheel of the real vehicle. Pitch and roll rotations are neglected. Recent papers [6, 11] have shown the capability of this simple model to reproduce complex and aggressive maneuvers while matching experimental data logged on real vehicles. The present formulation is essentially the extension of the one employed in section 3.3 to the case where also the handbrake command is among the inputs available to the driver.

Optimal control

Additional inequality constraints (e.g. those on inputs) are added into the performance index J Eq.(1.47) using penalty function (soft constraints), thus not changing the problem formulation described above.
The resulting algebraic-differential system is discretized in order to obtain a finite dimensional algebraic problem. The simulation interval is splitted into N intervals. The resulting system can be solved using a solver for nonlinear algebraic equations. In this case the solver described in [9] is employed. The size of the system for the simulations presented in the current work is in the order of 2000 equations and as many variables. The computation time is 10 to $15s$ (simulated maneuvers of about $5s$) on a laptop with Intel Core 2 Duo 2.8GHz, 4GB RAM and running windows 7.
In the specific case, the model equations $\mathbf{f}$ consists of Eq.(3.59-3.63,3.66-3.67,3.77-3.80,1.62-1.64), $\mathbf{x}$ is the state vector reported in Eq. (3.141) and $\mathbf{u}$ are the driver controls of Eq.(3.145), while the cost function J is a combination of the total maneuver time T and the lateral deviation from the road inner limit. Indeed, empirical guidelines from expert drivers suggest that handbrake cornering technique is used to negotiate very tight corners as fast as possible in limited space. More precisely, the performance index (or cost function) is:

$$J = \begin{cases} \int dt & s \leq s_F \\ \int 1 \pm C_s s_n dt & s > s_F \end{cases} \tag{3.96}$$

where the upper cost function is a pure minimum time criterion, while the lower combine minimum time with a lateral deviation criterion. In particular C_s is the weight for the lateral deviation, s_F is the value of the curvilinear abscissa where the cost on the lateral distance starts to be applied, s_n is the lateral displacement from the road center lane. Note that φ contains a $\pm$ term: $+$ holds in the case of left corner (where minimum deviation from the road inner limit means minimum s_n) while $-$ in case of right corner (where minimum deviation from the road inner limit means maximum s_n). Summarizing, the virtual optimal driver has to perform the maneuver in the minimum time while trying to stay as close as possible to the road inner limit for $s > s_F$. In practice the additional cost on the lateral deviation is applied only near the corner see Fig.3.27 (while the minimum time term is obviously applied all along the maneuver).

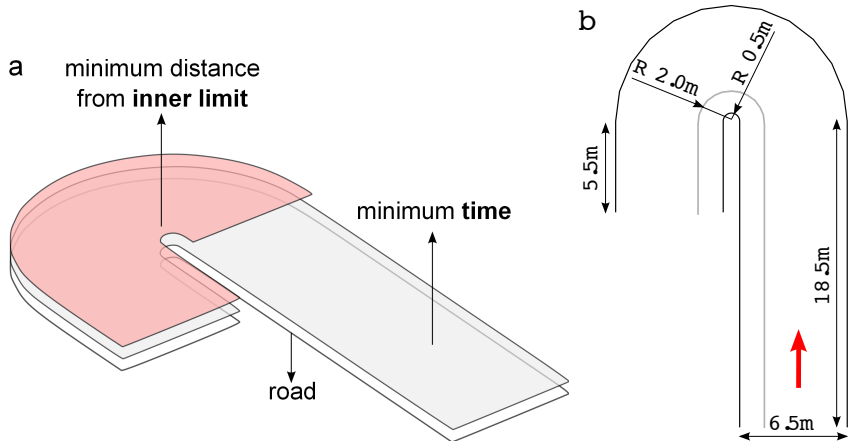

Figure 3.27: (a) Distribution of the two terms of the cost function on the hairpin: the lateral deviation cost is applied from the beginning of the corner till the finish line, while the minimum time cost is applied all along the maneuver. (b) Geometry of the hairpin.

Additional inequality constraints are introduced in the performance index in the form of penalty functions (see Tab.(3.7) for values).
More precisely, since the maximum steering angle on vehicles is limited to a certain $\delta_{\max}$, a corresponding inequality constraint is added as follows:

$$\delta \leq |\delta_{\max}| \tag{3.97}$$

To include the limited capabilities of real drivers, also the maximum steer angle rate is limited to $\dot{\delta}_{\max}$:

$$\dot{\delta} \leq \left|\dot{\delta}_{\max}\right| \tag{3.98}$$

A similar limitation is added to the whole propulsive/braking torque, i.e. to the driver throttling/braking actions:

$$\dot{\gamma}_t \leq |\dot{\gamma}_{t_{\max}}| \tag{3.99}$$

and to the handbrake torque:

$$\dot{h}_b \leq \left|\dot{h}_{b_{\max}}\right| \tag{3.100}$$

To account for the limited engine power, another inequality constraint is added, stating that the whole propulsive torque (rear axle plus front axle) is limited:

$$\left(\gamma_t k_t \omega_R + \gamma_t \left(1 - k_t\right) \omega_F\right) Mg \leq P_{\max} \tag{3.101}$$

In order to constraint the vehicle trajectory within the road boundaries the following inequality constraints are added:

$$-L_w \leq s_n - b \sin\alpha \leq R_w \tag{3.102a}$$
$$-L_w \leq s_n + a \sin\alpha \leq R_w \tag{3.102b}$$

Table 3.6: Pacejka tire parameters.

Off-road			
B	1.5071	D	0.7000
C	1.0901	E	-1.5840
Asphalt			
B	7.0000	D	1.0000
C	1.8000	E	0.0000

where R_w and L_w are right and left road widths respectively.
Initial and final conditions, e.g. vehicle velocities and positions on the road at the start and finish line given by:

$$\mathbf{b}_1\left(\mathbf{x}\left(0\right),\mathbf{u}\left(0\right)\right)=0 \qquad \mathbf{b}_2\left(\mathbf{x}\left(T\right),\mathbf{u}\left(T\right)\right)=0 \tag{3.103}$$

The result of the optimal control problem completely describes both the dynamics of the vehicle system during the maneuver and the driver inputs that produce it.

3.4.4 Road-tire interaction

When measuring in test rigs tire properties in terms of forces/torques as a function of slips, the response of the specific tire on the specific test surface is identified. In other words the same tire behaves differently on different road surfaces. However, experience highlighted some general patterns, see e.g. [20, 22]. In particular, the same tire on different road asphalts exhibits an almost unchanged cornering stiffness, while significant variation occurs on the friction peak coefficient. Even when moving to wet asphalt (in non hydroplaning condition) the cornering stiffness does not change significantly while the friction peak is greatly reduced.
Practically speaking, as long as the ground surface can be considered rigid with respect to the tire carcass, the tire exhibits basically the same cornering stiffness (as predicted by theoretical brush and string models in [10] Ch.3,5). On the contrary, when off-road surfaces are considered (e.g. gravel), the ground cannot be considered rigid with respect to the tire, and a reduction on the effective cornering stiffness is therefore expected. In [23, 24] it is shown that the changes in the tire force vs slip curve are in the direction of a reduction of the cornering stiffness, while in [25] it is reported that the peak of the lateral force moves towards high slips and even disappears (in very soft surfaces a bulldozing effect related to the plowing of the soil may even take place). The same adjustments characterize the curve of longitudinal forces vs longitudinal slip [24].
In the current work, two types of tire-road interaction curves are considered and simulated to evaluate the effect of the change in the road surface on the optimal driving strategy. The corresponding Pacejka coefficients B, C, D, E are reported in Tab.3.6 (same values are used for the lateral and longitudinal forces).
In practice the first set of parameters is representative of a tire on an off-road surface (dashed red curve in Fig. 3.28) while the second is representative of a tire on a paved asphalt road (blue solid curve in Fig. 3.28). When comparing the two curves, the off-road curve has a reduced friction coefficient, reduced slope and absence of a visible peak, as reported in the literature.

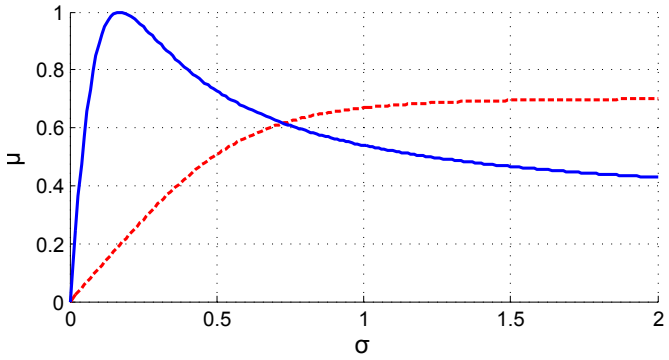

Figure 3.28: Tire-road friction coefficient μ as a function of the slip σ: blue solid line is for paved asphalt road and dashed red line is for off-road.

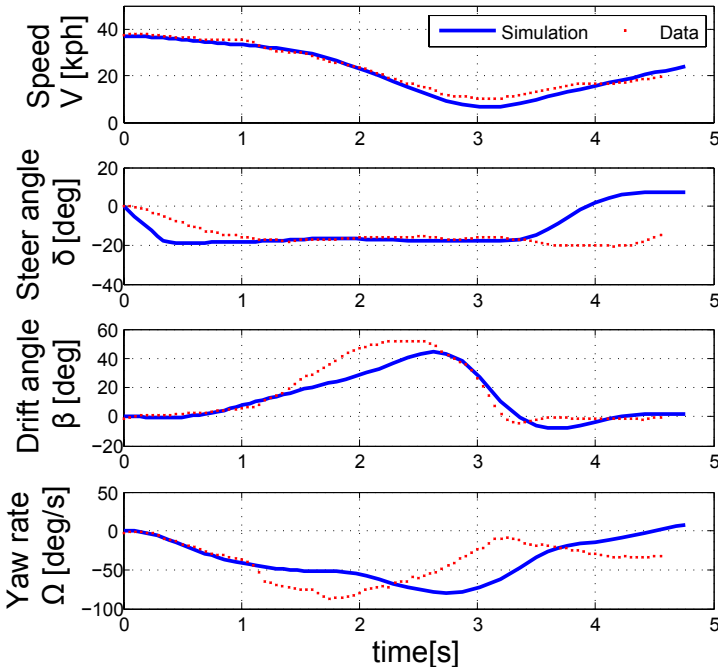

Figure 3.29: Comparison between numerical simulation (solid blue line) and experimental data (dotted red line) of the FWD test vehicle.

3.4.5 Optimal handbrake cornering on off-road

Simulation vs Road Test

In this section nonlinear simulations are analyzed and compared with the road data presented in section 3.4.2. The vehicle data are reported in Tab.3.7 and the boundary condition of the control problem are summarized in Tab.3.8. In practice the simulation starts with the vehicle aligned with the road center line, at a speed of 37 kph and laterally shifted by 4.8 m with respect to the road center line, in agreement with the experimental conditions. The simulations and the road data are compared in Fig.3.29 in terms of velocity, steer angle, vehicle drift and yaw rate. The agreement is rather good. The optimal speed profile identified by the simulation almost perfectly tracks the experimental velocity. The steering command is applied in a more aggressive way in the simulation for $t < 1$ s then the agreement is perfect till $t = 3.5$ s, where the virtual driver chooses a slightly different exit strategy. It should be noted that there is no

Table 3.7: Parameters of the vehicle model.

Parameter	Symbol	Value	Unit
Gravity	g	9.81	m/s^2
Mass	M	1300	kg
Total yaw inertia	I_G	2000	$kg\,m^2$
Height of CoM	h	0.50	m
Distance of CoM from rear	b	1.53	m
Distance of CoM from front	a	0.96	m
Axle inertia	I_M	1.8	$kg\,m^2$
Wheel radius	r	0.28	m
Drag coefficient ($\frac{1}{2}\rho C_x A$)	K_D	0.2107	kg/m
Tire relaxation lenght	σ_r	0.50	m
Suspensions time-lag	τ_N	0.25	s
Propulsive torque ratio (FWD)	k_t	0	
Braking torque ratio	k_t	0.4	
Braking torque saturation	$\gamma_{R_{\min}}$	-0.028	
Engine power	$P_{\max}$	110	kW
Max torque rate	$\dot{\gamma}_t Mg$	3500	Nm/s
Max handbrake torque rate	$\dot{h}_b Mg$	3500	Nm/s
Max wheel steer angle	$\delta_{\max}$	20	deg
Max wheel steer rate	$\dot{\delta}_{\max}$	60	deg/s

counter-steering all along the curve (i.e. for time up to 4 s). The steer inward the curve is in accordance also with [11] which shows that for small turning radius the equilibrium steer of a FWD vehicle is inward the curve (no counter-steering). Also the simulated and experimental vehicle drift are close each other, the simulated one remaining slightly lower than the experimental when it comes to the peak value (45 deg vs 52 deg). The matching of vehicle drift on the time scale is relevant. The yaw rates exhibit the same maximum values, but the experimental peak is reached slightly before the simulated peak. The comparison can be further appreciated in terms of trajectory in Fig.3.32, where a) represents the simulated maneuver, b) represents the experimental data and in d) the simulated and experimental trajectories are superimposed. The agreement between the two is almost perfect until the exit of the curve ($3 - 3.5$ s). Afterward, the virtual rider (a) keeps close to the inner road limit while the real driver (b) moves towards the center line while approaching the next turn.

Another relevant observation is based on the inspection of Fig.3.30, which allows to appreciate the main difference between the virtual driver (Fig.3.30a) and the real driver (Fig.3.30b) for this particular technique in terms of control input. The real driver applies the handbrake command (DATA Rear braking pressure in Fig.3.30b) essentially as an on-off input, to lock the rear wheel (DATA Rear left wheel speed in Fig.3.30b) for the whole first part of the maneuver. The virtual driver modulates the handbrake command, which corresponds to a rear wheel braking torque (SIM Rear wheel torque in Fig.3.30a), to achieve the optimal performance. In practice this would correspond to modulating the handbrake lever position during the curve, which is out of the capabilities of real drivers. Nevertheless the virtual rider locks the rear axle

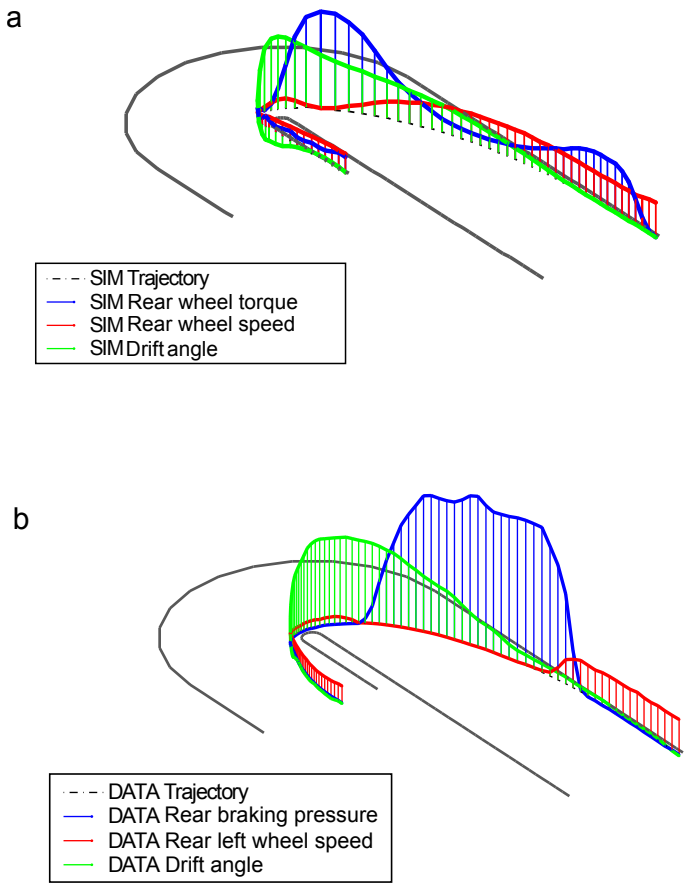

Figure 3.30: (a) 3D representation of the comparison between simulations results and (b) experimental data of the FWD test vehicle.

Table 3.8: Boundary conditions.

Variable	Initial B.C.	Final B.C.
V	37 kph	free
β	0	free
Ω	0	free
ω_R	trim	free
ω_F	trim	free
f_R	0	free
f_F	0	free
s_R	0	free
s_F	0	free
n_R	trim	free
n_F	trim	free
s_s	0	2π+24 m
s_n	4.8 m/free	free
α	0	free

(SIM Rear wheel speed in Fig.3.30a). Also in this figure the agreement between the simulated and experimental vehicle drift angle can be appreciated (SIM Drift Angle in Fig.3.30). Going deeper into the detail of the simulation, Fig.3.31 highlights that the virtual driver applies the handbrake command two times at $t = 0.3$ s (minor, not present in road test) and $t = 2.0$ s (major, consistent with road test). During the first application the rear wheel spin velocity slightly decreases (Fig.3.31a), whereas during the second handbrake the velocity decreases abruptly and the wheel locks at $t = 2.1$ s. The inspection of the steering angle reveals that it is used in an aggressive manner and kept inward the curve to its maximum value for most of maneuver. The axle normal load exhibit minor fluctuations (Fig.3.31c) and the over-steering behavior is therefore induced through the handbrake which saturates the rear tire friction. Note that the pedal brake is not applied at all (Fig.3.31d) according to experimental evidence.

Effect of Initial Lateral Position

In the previous section the optimal handbrake maneuver has been compared with road tests in off-road condition. In particular the initial lateral position of the vehicle on the road s_n was fixed to match the experimental data for a proper comparison. In this section the aim is to evaluate the effect of a free initial lateral position s_n on the road (i.e. the virtual rider can choose the optimal initial lateral position).
Therefore the same vehicle is simulated with the same boundary conditions with the exception that the initial lateral position of the vehicle on the road s_n is now free. Results are reported in Fig.3.32c and Fig.3.33. When comparing with the case of fixed initial position Fig.3.32a and Fig.3.31 similar steer δ and drift β profiles are observed. The load transfer (see axle loads n_R and n_F) is higher in the case with free initial lateral position, due to the combination of pedal brake with handbrake, while there is only handbrake when the initial lateral position is set on the outer limit. Also in this case there is locking of the rear wheel but it occurs slightly afterward (2.5 s in Fig.3.33a instead of 2 s in Fig.3.31a). In practice with the free initial lateral

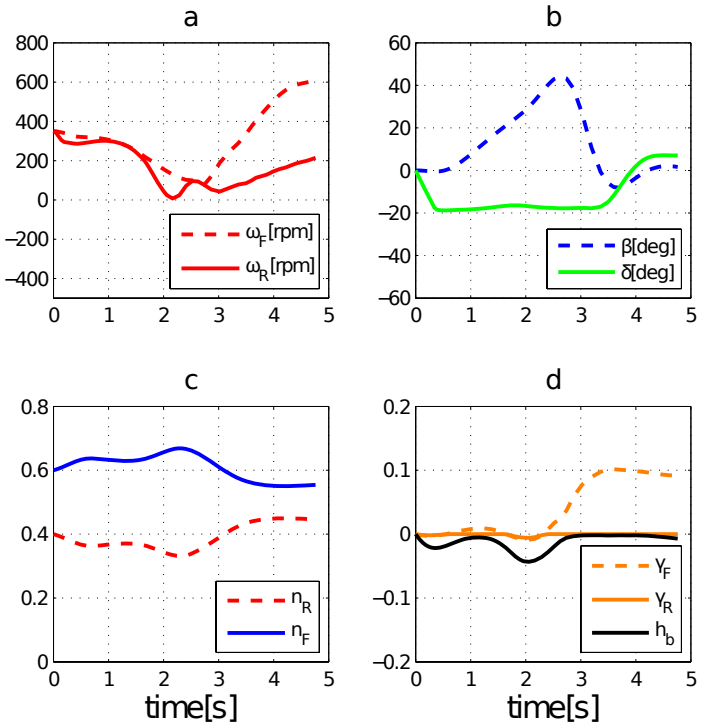

Figure 3.31: Handbrake cornering simulation results of the FWD test vehicle: off-road and fixed initial lateral position s_n. (a) front and rear wheel spin $\omega_{F,R}$, (b) drift angle β and steer angle δ, (c) front and rear normalized tire load $n_{F,R}$, (d) front and rear normalized torque $\gamma_{F,R}$ and handbrake h_b.

position the virtual driver chooses a slightly different strategy to enter the curve. Indeed when starting almost in the middle of the road there is time to accelerate the vehicle before braking into the turn to exploit the trail-braking technique (i.e. load transfer to induce over-steering and rear axle skidding). In this case handbrake is used in addition to amplify the standard ratio between the rear brake and the front brake.

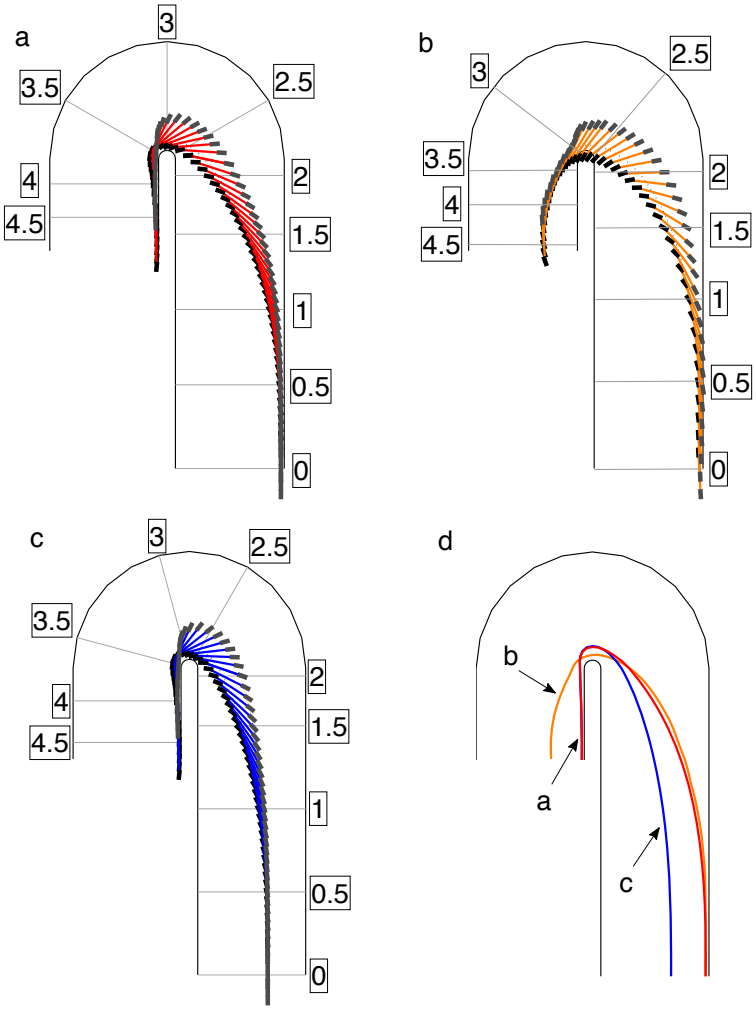

Figure 3.32: Comparison between numerical simulations and experimental data of the FWD test vehicle: (a) numerical simulation with fixed initial position matching experimental initial position; (b) experimental data; (c) numerical simulation with free initial position; (d) superimposition of trajectories of simulations and experimental data reported in (a),(b),(c). Number in squares are the numerical simulation time and experimental logging time.

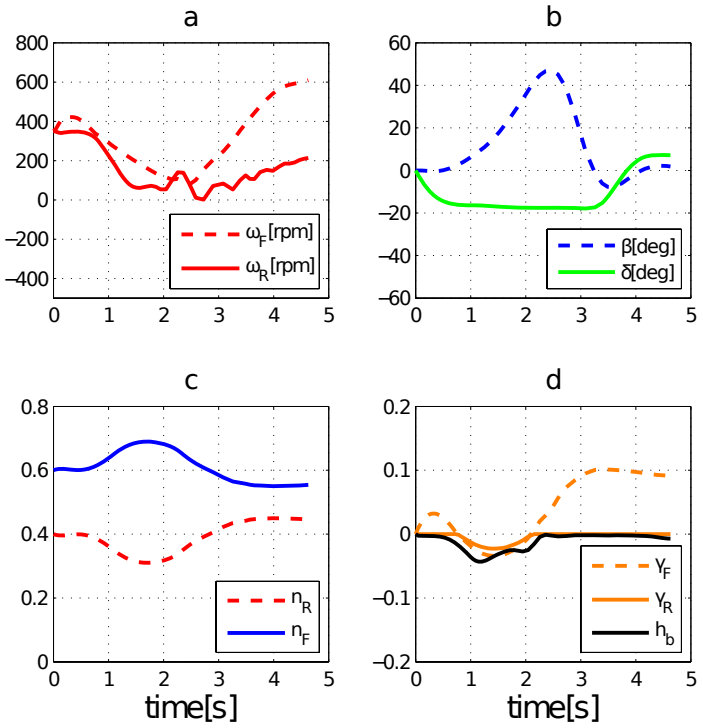

Figure 3.33: Handbrake cornering simulation results of the FWD test vehicle: off-road and free initial lateral position s_n. (a) front and rear wheel spin $\omega_{F,R}$, (b) drift angle β and steer angle δ, (c) front and rear normalized tire load $n_{F,R}$, (d) front and rear normalized torque $\gamma_{F,R}$ and handbrake h_b.

3.4.6 Optimal handbrake cornering on paved road

In the previous section the optimal handbrake maneuver on off-road conditions has been considered and compared with road tests. Both fixed and free initial lateral position of the vehicle on the road s_n have been considered. In this section we aim at investigating the optimal handbrake maneuvering on paved road, to examine whether the road surface condition is essential to make the handbrake technique the optimal cornering strategy.
Therefore the same vehicle is simulated with a different road-tire curve (asphalt parameters instead of the off-road parameters of Tab.3.6, see Fig.3.28 for force vs slip curve) and same boundary conditions. The initial lateral position of the vehicle on the road s_n is kept free.
There is a main handbrake actuation between $0.5 < t < 2.0\,\text{s}$ (Fig.3.34d) and the deceleration of the rear wheel with respect to the front wheel is evident for $t > 1\,\text{s}$ and with locking at $t = 2.2\,\text{s}$ (Fig.3.34a). The vehicle drift has a peak of $40\,\text{deg}$ in the range $t = 2.5 - 3\,\text{s}$ (Fig.3.34b), growing from $1.5\,\text{s}$ to the middle of the turn $t = 3\,\text{s}$. The steering is kept inward the curve and reaches the limit value for $t = 2.5 - 4\,\text{s}$. The friction allows for a significant load transfer which is exploited to induce the over-steering behavior in addition to the handbrake effect. Pedal braking is employed by the virtual driver for $0.5 < t < 2.5\,\text{s}$ in Fig.3.34d. However, also in the paved road handbrake is used and added to the pedal braking to increase the ratio between the rear brake and the front brake efforts. On the contrary, in off-road conditions the tires have not sufficient friction to produce a significant braking load transfer that would give the necessary over-steering behavior, and thus the driver has to rely only on the handbrake. Note that the over-steering behavior is essential to complete the tight hair-pin in the minimum

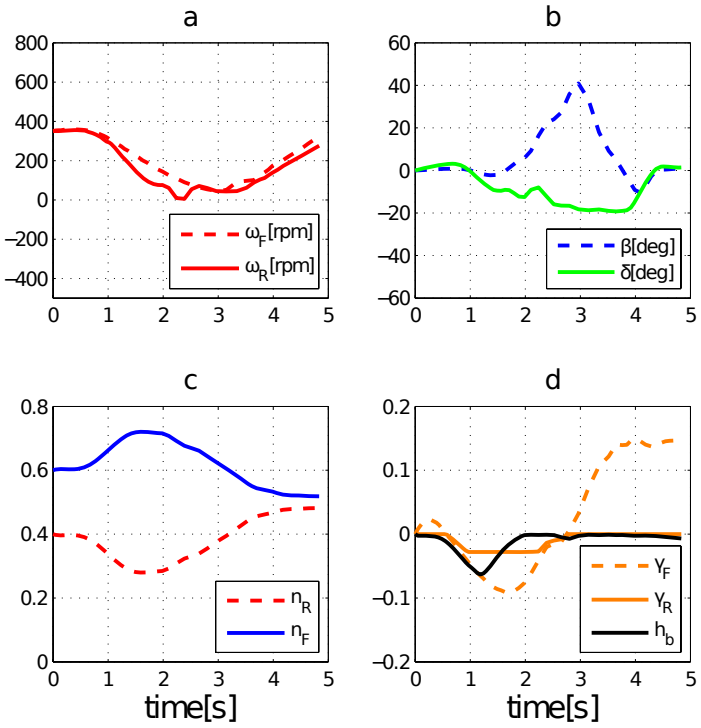

Figure 3.34: Handbrake cornering simulation results of the FWD test vehicle: asphalt road and free initial lateral position s_n. (a) front and rear wheel spin $\omega_{F,R}$, (b) drift angle β and steer angle δ, (c) front and rear normalized tire load $n_{F,R}$, (d) front and rear normalized torque $\gamma_{F,R}$ and handbrake h_b.

time while keeping the vehicle close to the inner limit of the road.

Effect of Availability of the Handbrake Input

In this section we investigate the effect of the handbrake on the optimal maneuver trajectory. Fig.3.35a shows the trajectory of the optimal handbrake maneuver discussed in section 3.4.6, i.e. asphalt road with free vehicle initial lateral position s_n. It is worth observing that the maneuver is coupled with another typical rally driving technique: the pendulum-turn, where the driver moves from the inner limit of the road to the outer limit before moving back to the inner limit while entering the curve. Note that the initial lateral position of the vehicle on the road is free and therefore the pendulum strategy is a result of the optimization, and not induced by a fixed starting point close to the inner limit of the road. In other words, the pendulum is an optimal strategy, otherwise the driver would have chosen to start from the outer limit of the road.
Fig.3.35b shows the case when the handbrake is inhibited. In this case the initial pendulum is amplified and more lateral space is required in order to achieve the maximum yaw rate at the apex of the turn. This fact highlights once more the optimality of handbrake with respect to the lateral deviation from the inner limit.
Finally, Fig.3.35c reports the optimal maneuver in the case the cost on the lateral deviation from the inner road limit is neglected, i.e. $C_s = 0$ in Eq.3.96. With the sole cost on the time maneuver, the typical circuit-like maneuver is found, with the vehicle starting from the outer

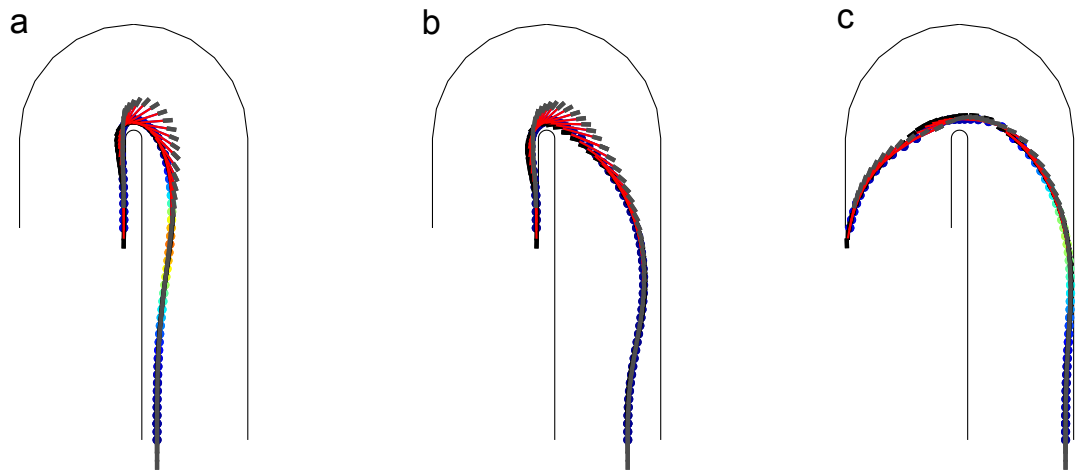

Figure 3.35: Effect of the handbrake on the cornering simulation with free initial lateral position s_n for the FWD test vehicle: (a) asphalt road with handbrake , (b) asphalt road with handbrake inhibited , (c) asphalt road with no cost on the lateral deviation from the inner road limit (pure minimum time).

limit of the road, reaching the apex of the turn on the inner boundary and then exiting the curve on the outer limit using the whole available width of the road.
When comparing total maneuver time, the pure minimum time simulation c) ranks first, followed by b) and c) which have similar times.
Summarizing, this section highlights that the cost on the lateral deviation from the road inner limit is essential to induce the pendulum strategy on asphalt road and keep the vehicle exiting the curve far from the outer limit of the road (typical rally driving strategy observed in races).
In addition, handbrake allows for reducing the lateral space necessary for turning while keeping the maneuver time almost unchanged.

3.4.7 Sensitivity Analysis

In this section the effect of the variation of some fundamental parameters on the optimal driving strategy is considered. Namely the effect of the yaw inertia, center of mass position, tire-road maximum friction are analyzed below. In addition, the effect of a variation in the input limits, namely maximum steering angle, maximum steering rate, maximum propulsive/brake and handbrake torque rate is included.

Effect of Yaw inertia

The total yaw inertia of the car is $I_G = 2000\,\mathrm{kgm}^2$. Simulations are carried out with the inertia reduced to $I_G = 1500\,\mathrm{kgm}^2$ and $I_G = 1000\,\mathrm{kgm}^2$. Results are reported in Fig.3.36. All three maneuvers are high-drift and include handbrake. It can be observed that as the yaw inertia decreases the pendulum is less pronounced. In particular the vehicle travels almost straight and parallel to the road boundaries when the inertia is minimum. Indeed, with a lower inertia the vehicle is more reactive with respect to the driver inputs and is no more necessary to perform the pendulum to attain the maximum yaw rate while into the curve. In practice, reduced inertia implies a reduced yaw momentum has to be achieved entering the curve. Limited variation on the handbrake usage are present.
It can be concluded that the yaw inertia has a minor effect on the handbrake strategy, although it has some effect on the optimal trajectory to enter the turn.

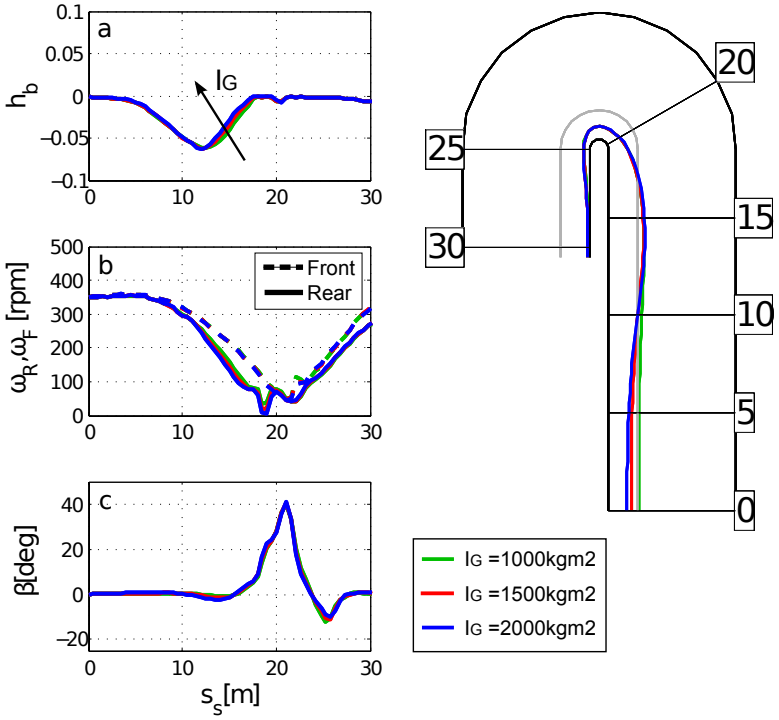

Figure 3.36: Effect of yaw vehicle inertia on handbrake cornering simulation for the FWD test vehicle. Number in squares are the road curvilinear abscissa s_s. (a) normalized handbrake torque h_b, (b) front and rear wheel spin $\omega_{F,R}$, (c) drift angle β.

Effect of Center of Mass Position

The longitudinal position of the center of mass is b=1.530 m from the rear axle in the baseline configuration. Simulations are carried out with the center of mass moved rearward to the mid wheelbase, b=1.245 m, and further back to b=0.960 m. Results are reported in Fig.3.37. The three maneuvers are very similar in trajectory while significant changes in the usage of the handbrake appears. As the center of mass is moved rearward, a corresponding increase in the handbrake effort is necessary, as a consequence of the higher normal load on the rear axle.
Furthermore the peak of the braking force is moved towards the turn, so even if the trajectory does not change the handbrake phase is longer.

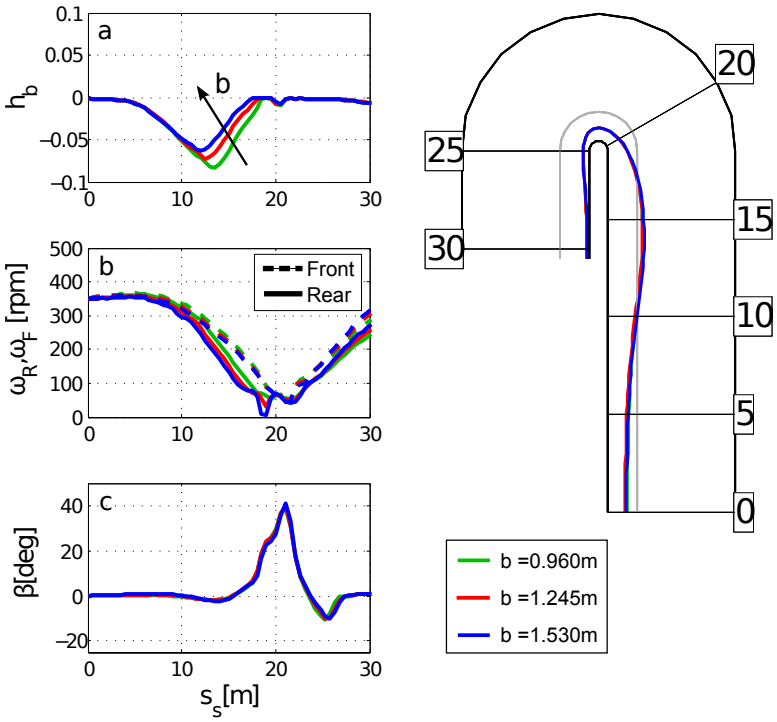

Figure 3.37: Effect of position of the center of mass on handbrake cornering simulation for the FWD test vehicle. Number in squares are the road curvilinear abscissa s_s. (a) normalized handbrake torque h_b, (b) front and rear wheel spin $\omega_{F,R}$, (c) drift angle β.

Effect of Tires Friction

The friction peak is $\mu = 1$ in the baseline configuration on paved asphalt road. Simulations are carried out with $\mu = 1.25$ and $\mu = 1.50$, corresponding to higher performance tire on a paved road. The same cornering stiffness is kept. Results are reported in Fig.3.38.
The results highlights that with higher road-tire friction higher handbrake torque are necessary to obtain the same results in terms of vehicle drift and trajectory.

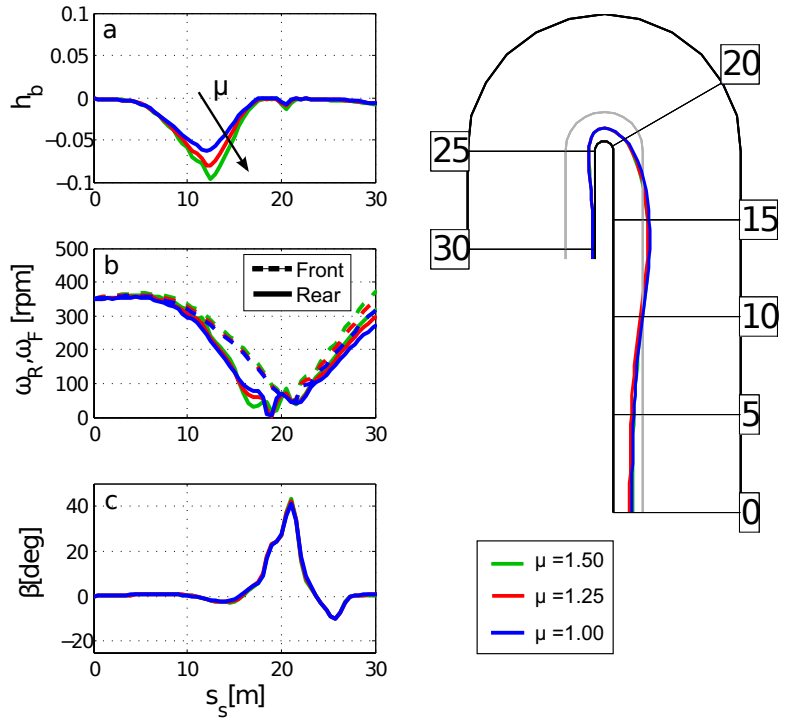

Figure 3.38: Effect of friction coefficient on handbrake cornering simulation for the FWD test vehicle. Number in squares are the road curvilinear abscissa s_s. (a) normalized handbrake torque h_b, (b) front and rear wheel spin $\omega_{F,R}$, (c) drift angle β.

Effect of Steering Limits

All optimizations discussed so far have been carried out with a steering angle limit $\delta_{\max} = 20deg$ and a steering rate limit $\dot{\delta}_{\max} = 60deg/s$. The former limit is a physical limit of the car while the latter is a physiological limit of the driver.
In order to verify that the handbrake technique is not triggered by the specific values of the constraints used for the steering input, additional simulations with greater steering limits have been carried out.
Fig.3.39 shows minor changes in the trajectory and handbrake usage when increasing the maximum steering angle to 25 and $30deg$, while Fig.3.40 shows minor changes when increasing the steering rate to 90 and $120deg/s$. Also, the pendulum strategy is present in all cases.

Effect of Torque Limits

All optimizations discussed so far have been carried out with a torque rate limit $\dot{T}_{\max} = \dot{\gamma}_{t_{\max}} Mg = \dot{h}_{b_{\max}} Mg = 3500Nm/s$. In order to verify that the handbrake technique is not triggered by the specific values of the constraints used for the variation of the torque input, additional simulations have been carried out with greater limits. Fig.3.41 confirms minor changes in the trajectory and handbrake usage when increasing the torque rate to 4000 and $4500Nm/s$. Also, the pendulum strategy is present in all cases.

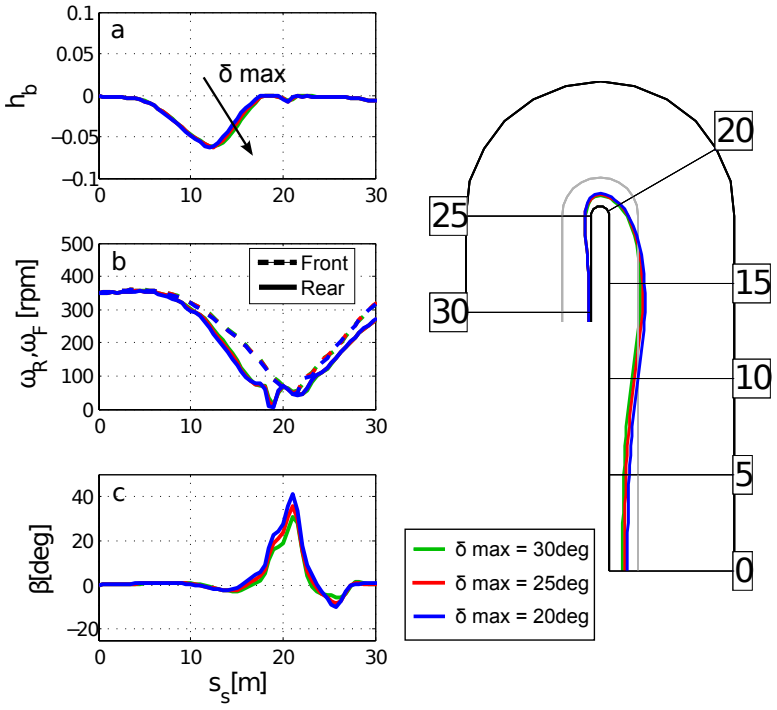

Figure 3.39: Effect of maximum steering angle $\delta_{\max}$ on handbrake cornering simulation for the FWD test vehicle. (a) normalized handbrake torque h_b, (b) front and rear wheel spin $\omega_{F,R}$, (c) drift angle β.

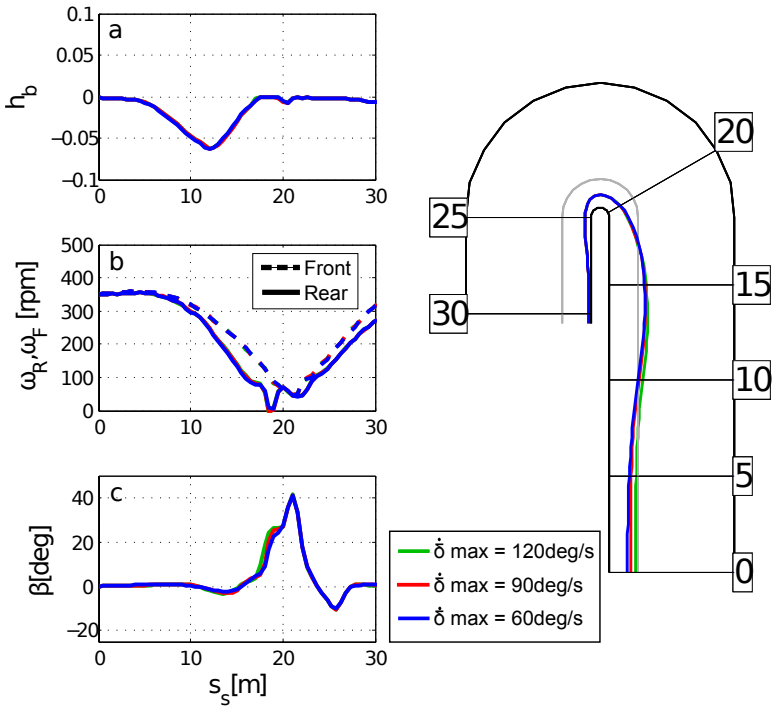

Figure 3.40: Effect of maximum steering rate $\dot{\delta}_{\max}$ on handbrake cornering simulation for the FWD test vehicle. (a) normalized handbrake torque h_b, (b) front and rear wheel spin $\omega_{F,R}$, (c) drift angle β.

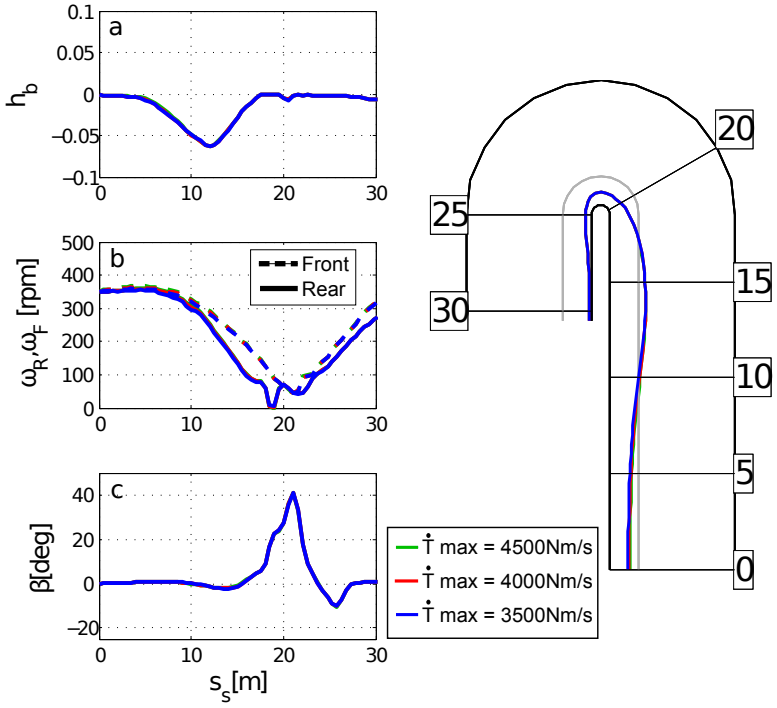

Figure 3.41: Effect of maximum torque rate $\dot{T}_{\max} = \dot{\gamma}_{t_{\max}} Mg = \dot{h}_{b_{\max}} Mg$ on handbrake cornering simulation for the FWD test vehicle. (a) normalized handbrake torque h_b, (b) front and rear wheel spin $\omega_{F,R}$, (c) drift angle β.

3.4.8 Conclusions

The handbrake cornering technique has been analyzed and simulated to investigate the optimality of a strategy which is widely used with different vehicles and under different surface conditions in rally races. Nonlinear optimal control techniques have been used to model the driver behavior. The capability of the model to reproduce very demanding experimental maneuvers involving the handbrake has been demonstrated through the comparison of simulation results with real data from a professional rally driver. It turned out that the optimal virtual driver mimics the real rally driver behavior when the cost function to be minimized includes the lateral deviation from the road inner limit in addition to the total maneuver time. In practice the handbrake technique allows for minimum (lateral) space and minimum time cornering on tight hairpins.
Comparison with pure minimum time maneuvering has been included to highlight the fundamental role of the cost related to the lateral deviation of the vehicle from the road inner limit. Numerical optimization showed that, on asphalt road, the handbrake can be coupled with another typical rally driving technique: the pendulum turn. Finally, a sensitivity analysis on some important vehicle parameters has been performed to demonstrate that the handbrake and the pendulum strategies are consistently present in numerical results and therefore are not related to a particular set of vehicle/tire parameters, boundary conditions and inputs limits.
The work shed a light on the understanding of an aggressive maneuvering technique that could help in the development of advanced vehicle control systems and/or autonomous vehicle able to exploit the full potential of tire non-linearities, e.g. minimum time evasive maneuvers in limited/constrained space scenarios.

3.5 SuperKart: racing kart model

The vehicle model described in this section deals with the modeling of the dynamics of racing go-karts.
It includes a single rigid body comprising the inertial properties related to all the bodies of the real vehicle, such as wheels, engine and the rider, that for light vehicles as go-karts contributes to the total weight and inertia in a not negligible way.
Lateral and longitudinal forces as well as vertical loads are applied in four contact points to model tire-ground interactions. The overall motion in not planar like for the single-track model shown before, but it includes roll as well as pitch motion.
With respect to the scheme presented in figure 3.42 the overall dynamics of the vehicle can be

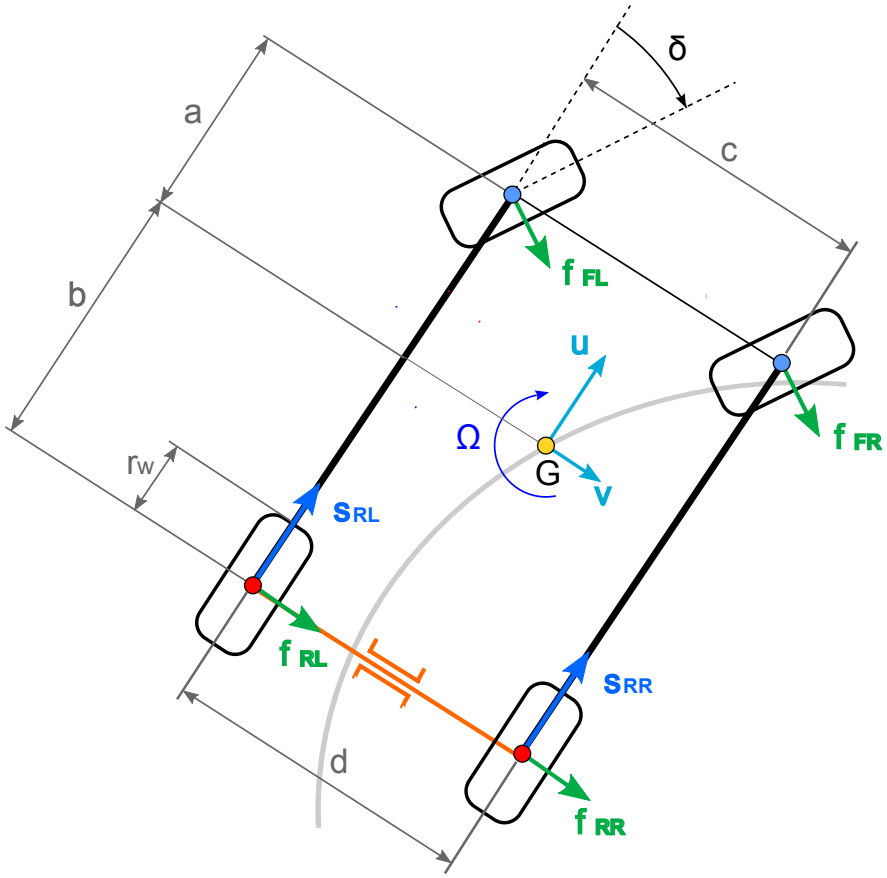

Figure 3.42: SuperKart model scheme

expressed by the following equations of motion:

$$\dot{u} = g[s_{RR} + s_{RL} - (f_{FR} + f_{FL})\,\delta] - \frac{k_D\,u^2}{M} \tag{3.104}$$

$$\begin{aligned}\dot{v} =& \frac{1}{2\,I_Z}\Big\{2g\,f_{FL}\Big[\frac{1}{2}Mc(b-b_1)\delta + (b-b_1)(b-b_1-a_1)M + I_Z\Big] + \\ &+ 2g\,f_{FR}\Big[-\frac{1}{2}Mc(b-b_1)\delta + (b-b_1)(b-b_1-a_1)M + I_Z\Big] + \\ &+ 2g(f_{RL}+f_{RR})[M\,b(b-b_1) + I_Z] + (s_{RR}-s_{RL})[Mg\,d(b-b_1)] - 2\,\Omega\,u\,I_Z\Big\}\end{aligned} \tag{3.105}$$

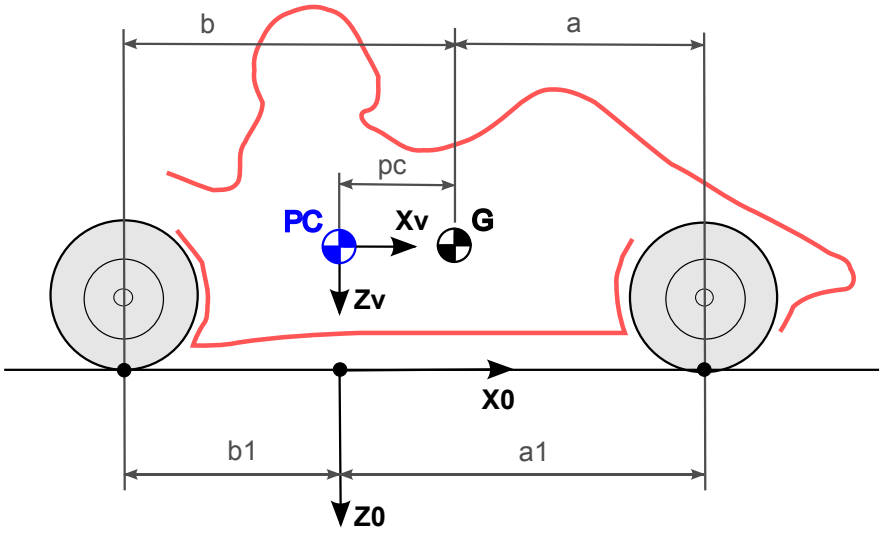

Figure 3.43: SuperKart model scheme

$$\dot{\Omega} = -\frac{Mg}{I_Z}\Big[f_{FL}(\frac{1}{2}\,c\,\delta - a_1 - b_1 + b) + f_{FR}(-\frac{1}{2}\,c\,\delta - a_1 - b_1 + b) + \\ + b\,(f_{RR} + f_{RL}) - \frac{1}{2}\,d(s_{RL} - s_{RR})\Big] \tag{3.106}$$

$$\dot{\phi}_{dot} = \frac{1}{2}\frac{Mg}{I_X}\Big[-2\,h(f_{RR} + f_{RL} + f_{FR} + f_{FL}) + c(n_{FL} - n_{FR}) + d(n_{RL} - n_{RR})\Big] \tag{3.107}$$

$$\dot{\mu}_{dot} = -\frac{Mg}{I_Y + M\,b^2 - 2M\,b\,b_1 + M\,b_1^2}\Big\{\mu(b - b_1)[(f_{FL} + f_{FR})\delta - s_{RL} - s_{RR}] + \\ + \delta\,h(f_{FL} + f_{FR}) - b_1 + b + b_1(n_{RR} + n_{RL}) - a_1(n_{FR} + n_{FL}) - h(s_{RR} + s_{RL})\Big\} \tag{3.108}$$

where u and v are longitudinal and lateral velocities with respect to vehicle axes, Ω is the yaw rate, ϕ is the chassis roll angle, μ is the chassis pitch angle, f_i and s_i are lateral and longitudinal forces respectively with $i = \{FL, FR, RR, RL\}$ and δ is the steer angle (that has been assumed to be equal for both the front wheels), ϕ_{dot} and μ_{dot} being first time derivative of ϕ and μ respectively. These last are introduced for a first order formulation through the following first order equations:

$$\dot{\phi} = \phi_{dot} \tag{3.109}$$

$$\dot{\mu} = \mu_{dot} \tag{3.110}$$

Because the current model has been thought only for kart simulations, a particular power-train system based on a rigid rear axle is modeled herein.
The equation that governs the ripartion of the torque within the driven axle is basically:

$$\dot{\omega}_A = \gamma_t\,Mg - r_w(s_{RR} + s_{RL})\,Mg \tag{3.111}$$

where ω_A is the average axle spin velocity.
From this it is possible to extract an average longitudinal slip quantity κ:

$$\kappa = \frac{\omega_A\,r_w}{u} - 1 \tag{3.112}$$

where r_w is the wheel radius.
In this particular model both thrust and braking forces are only applied to the rear wheels thus longitudinal slip quantities are basically calculated for the rear axle whereas front axle wheels are always in pure rolling condition.
Longitudinal slips for each of the rear wheels are expressed by:

$$\kappa_R = \kappa + \frac{1}{2}\frac{\Omega\, d}{u} \tag{3.113}$$

$$\kappa_L = \kappa - \frac{1}{2}\frac{\Omega\, d}{u} \tag{3.114}$$

where d is the rear track of the vehicle.
Due to fact that no-differential is present at the rear axle, driving into a turn the internal rear wheel, that must have a lower spin velocity than the external one, have to lift from the ground to allow the vehicle performing the turn without triggering a critical longitudinal slip that couldn't be acceptable for tire wearing and without inducing a strong under-steer behavior. To do this modern karts chassis are designed to allow a torsional deformation to permit the internal wheel to lift while carrying out a curve.
Lower is the radius of the turn, bigger is the ideal difference between spin rate of the wheels on the same axle and bigger is the negative effect of the absence of the differential on handling.
Moreover racing go-kart are suspension-less vehicles, but to model the overall stiffness of the chassis mentioned above virtual-suspension systems are included in the formulation and modeled as a standard spring-damper system for each wheel.
As shown in Fig.3.43 a pitch center P_C is defined and its position with respect to the rigid body center of mass p_c is calculated as a function of the stiffness of these virtual-suspensions that represent the deflection of the chassis upon each wheel.

$$a_1 = \frac{(a+b)\, k_R}{k_F + k_R} \tag{3.115}$$

$$b_1 = \frac{(a+b)\, k_F}{k_F + k_R} \tag{3.116}$$

where k_F and k_R are front and rear suspension stiffness respectively.
Vertical loads are calculated as the sum of the static load on each tire and of a quantity depending on the virtual-suspension load. This last is obtain as a particular function of the stroke and the rate of each suspension as formulated in the libraries described in section 2.
Static loads for rear and front wheels are:

$$n_{R_0} = \frac{1}{2}\frac{a_1 + b_1 - b}{a_1 + b_1} \tag{3.117}$$

$$n_{F_0} = \frac{1}{2}\frac{b}{a_1 + b_1} \tag{3.118}$$

The displacement and vertical rate of each point of the chassis (i.e. virtual-suspension stroke and rate) are calculated as follows:

$$z_{C_{RR}} = \mu\, b_1 + \frac{1}{2}\phi\, d \qquad \dot{z}_{C_{RR}} = \dot{\mu}\, b_1 + \frac{1}{2}\dot{\phi}\, d \tag{3.119}$$

$$z_{C_{RL}} = \mu\, b_1 - \frac{1}{2}\phi\, d \qquad \dot{z}_{C_{RL}} = \dot{\mu}\, b_1 - \frac{1}{2}\dot{\phi}\, d \tag{3.120}$$

$$z_{C_{FR}} = -\mu\, a_1 + \frac{1}{2}\phi\, c \qquad \dot{z}_{C_{FR}} = -\dot{\mu}\, a_1 + \frac{1}{2}\dot{\phi}\, c \tag{3.121}$$

$$z_{C_{FL}} = -\mu\, a_1 - \frac{1}{2}\phi\, c \qquad \dot{z}_{C_{FL}} = -\dot{\mu}\, a_1 - \frac{1}{2}\dot{\phi}\, c \tag{3.122}$$

c being the front track of the vehicle as shown in Fig.3.42.
Finally vertical loads are expressed as function of the static loads and suspension quantities z_C and $\dot{z}_C$, that becomes argument of the libraries functions. As mentioned before the user can choose both linear and non-linear description for the stiffness and the damping characteristics of the suspensions.

$$n_{RR} = n_{R_0} + \zeta(z_{C_{RR}}, \dot{z}_{C_{RR}}) \tag{3.123}$$
$$n_{RL} = n_{R_0} + \zeta(z_{C_{RL}}, \dot{z}_{C_{RL}}) \tag{3.124}$$
$$n_{FR} = n_{F_0} + \zeta(z_{C_{FR}}, \dot{z}_{C_{FR}}) \tag{3.125}$$
$$n_{FL} = n_{F_0} + \zeta(z_{C_{FL}}, \dot{z}_{C_{FL}}) \tag{3.126}$$

In order to allow the software to lift one of the inner wheel while approaching or exiting a curve, a special formulation to transfer the negative vertical load of the lifting wheel as positive vertical load on the other wheel of the same axle is employed herein.

$$n_{RR} = \mathrm{pos}(n_{RR}) + \mathrm{neg}(n_{RL}) \tag{3.127}$$
$$n_{RL} = \mathrm{pos}(n_{RL}) + \mathrm{neg}(n_{RR}) \tag{3.128}$$
$$n_{FR} = \mathrm{pos}(n_{FR}) + \mathrm{neg}(n_{FL}) \tag{3.129}$$
$$n_{FL} = \mathrm{pos}(n_{FL}) + \mathrm{neg}(n_{FR}) \tag{3.130}$$

where pos and neg are functions that return the positive and the negative part of the argument respectively.
Regarding lateral dynamics, side-slip angles are calculated for each wheel as follows:

$$\lambda_{RR} = \lambda_{RL} = \frac{k_F\,[v - (a+b)\Omega] + k_R\,v}{(k_F + k_R)\,u} \tag{3.131}$$
$$\lambda_{FR} = \lambda_{FL} = \frac{k_F\,[u\ \arctan(\delta) - v] + k_R\,[u\ \arctan(\delta) - v - (a+b)\Omega]}{(k_F + k_R)\,u} \tag{3.132}$$

Longitudinal forces are directly expressed as the vertical load times an adhesion coefficient that is function of both longitudinal slip and side-slip angle for each of the rear wheels. The corresponding formulation can be once more chosen by the user between the different possibilities for tire forces included in the specific library formulation. See section 2.

$$s_{RR} = n_{RR}\,\mu_{s_R}(\lambda_{RR}, \kappa_R) \tag{3.133}$$
$$s_{RL} = n_{RL}\,\mu_{s_R}(\lambda_{RL}, \kappa_L) \tag{3.134}$$

Same approach is applied to lateral forces for the four wheels, steady-state values are expressed as follows:

$$f_{RR_0} = n_{RR}\,\mu_{f_R}(\lambda_{RR}, \kappa_R) \qquad f_{RL_0} = n_{RL}\,\mu_{f_R}(\lambda_{RL}, \kappa_L) \tag{3.135}$$
$$f_{FR_0} = n_{FR}\,\mu_{f_F}(\lambda_{FR}, 0) \qquad f_{FL_0} = n_{FL}\,\mu_{f_F}(\lambda_{FL}, 0) \tag{3.136}$$

It has to be noticed how front lateral tire forces are functions only of side-slip angles as front wheels are considered in pure rolling conditions (i.e. without longitudinal slips). These forces

are then not directly applied at the contact points, but are computed from steady-state values using the widespread relaxation equations:

$$\frac{\sigma\ \dot{f}_{RR}}{u} + f_{RR} = f_{RR_0} \tag{3.137}$$

$$\frac{\sigma\ \dot{f}_{RL}}{u} + f_{RL} = f_{RL0} \tag{3.138}$$

$$\frac{\sigma\ \dot{f}_{FR}}{u} + f_{FR} = f_{FR_0} \tag{3.139}$$

$$\frac{\sigma\ \dot{f}_{FL}}{u} + f_{FL} = f_{FL_0} \tag{3.140}$$

σ being the relaxation length for lateral forces.
Summarizing, the vehicle model consists of 15 differential equations:
Eq. (3.104-3.108,3.111,3.110,3.137,1.62-1.64) and as many state variables:

$$\mathbf{x} = \{u, v, \Omega, \omega_A, \phi, \mu, \phi_{dot}, \mu_{dot}, f_{RR}, f_{RL}, f_{FR}, f_{FL}, s_s, s_n, \alpha\}^T \tag{3.141}$$

Road states and equations have been included in the formulation following the mathematical approach introduced in section 1.3.1.

$$\dot{s} = \frac{u\cos(\alpha) - v\sin(\alpha)}{1 - nK} \tag{3.142}$$

$$\dot{n} = u\sin(\alpha) + v\cos(\alpha) \tag{3.143}$$

$$\dot{\alpha} = \omega_\psi - K\frac{u\cos(\alpha) - v\sin(\alpha)}{1 - nK} \tag{3.144}$$

The control vector consists of two elements:

$$\mathbf{u} = \{\delta, \gamma_t\}^T \tag{3.145}$$

where δ is the steer angle and γ_t is the total driving or braking torque (normalized by the total weight Mg).

3.5.1 Superkart example

As an example of application, the same track used in section 3.1.2 is performed employing the kart model. Linear tire-ground interaction is set as well as proper suspension stiffness and damping in order to reproduce chassis stiffness for a vehicle that is usually suspension-less.

In Fig.3.45 states history is reported including longitudinal speed of the vehicle as well as pitch and roll angles for the chassis. Furthermore normalized (with the quantity $M\ g$) vertical and lateral loads are shown together with lateral acceleration.
Fig.3.45c confirms that the model formulation works in a proper way while approaching curves, with the vertical load for the rear inner wheel that is null (i.e. wheel lift) while braking entering in the turn and with front inner one that is null (i.e. wheel lift) while accelerating exiting the corner.

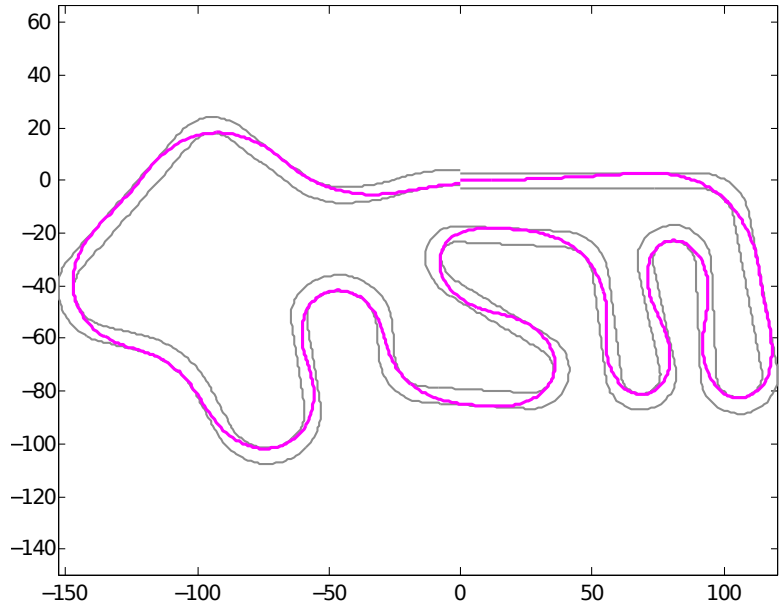

Figure 3.44: Trajectories calculated employing Superkart model on a whole closed track.

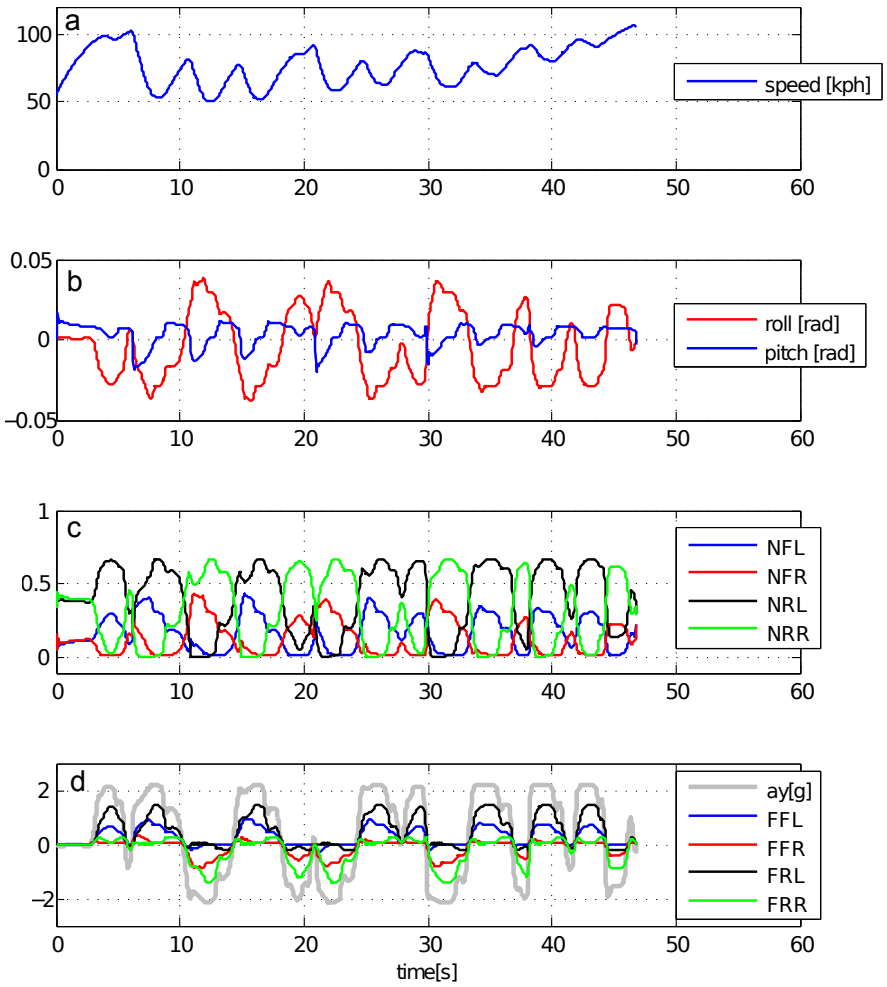

Figure 3.45: Simulation results employing Superkart model on a whole closed track.

3.6 SuperCarGP2: GP2 racing formula car model

In this section another four-wheeled vehicle model is described. This time the intent is to obtain a model to simulate racing formula cars behavior, that present different needs in modeling with respect to the previous vehicles.
The car model includes 5 rigid bodies: the chassis and the four wheels. The chassis has 6 dof (degrees of freedom), namely: longitudinal, lateral, vertical motion, yaw, roll and pitch rotations. Wheels (front and rear) have vertical displacement degree of freedom and steer rotation (front wheels only).
Tire-ground interaction forces are applied at four contact points.

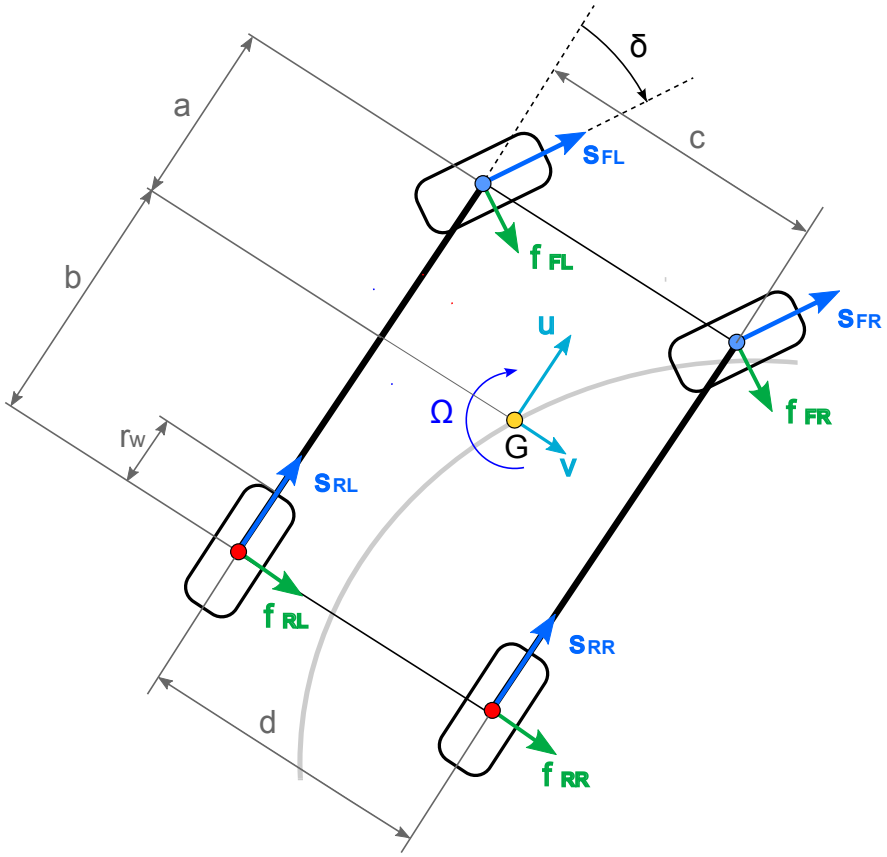

Figure 3.46: Formula GP2 model scheme

To limit degrees of freedom and dimension of the problem it has been chosen to avoid wheel axles dynamics description, in other words longitudinal forces are not computed from the equilibrium of each axle, unlike Superkart and Single-track model formulations, but are directly calculated as a function of an input total longitudinal force s_t (normalized with the weight Mg) and applied at the actual contact points.

$$s_{RR} = \frac{1}{2}\, k_t\, s_t \tag{3.146}$$

$$s_{RL} = \frac{1}{2}\, k_t\, s_t \tag{3.147}$$

$$s_{FR} = \frac{1}{2}(1 - k_t)\, s_t \tag{3.148}$$

$$s_{FL} = \frac{1}{2}(1 - k_t)\, s_t \tag{3.149}$$

s_t is split between the rear and front axle in braking condition according to the braking force distribution factor k_t. To simulate a RWD (i.e. Rear Wheel Drive) car $k_t = 1$ in driving conditions, thus longitudinal thrust forces are only applied at rear wheels. k_t is also changed according to the sign of longitudinal forces, indeed braking or driving conditions.
Current lateral forces are computed from steady-state values using the widespread relaxation equations:

$$\frac{\sigma \dot{F}_{RR}}{V_{RR}} + F_{RR} = F_{RR_0} \tag{3.150}$$

$$\frac{\sigma \dot{F}_{RL}}{V_{RL}} + F_{RL} = F_{RL_0} \tag{3.151}$$

$$\frac{\sigma \dot{F}_{FR}}{V_{FR}} + F_{FR} = F_{FR_0} \tag{3.152}$$

$$\frac{\sigma \dot{F}_{FL}}{V_{FL}} + F_{FL} = F_{FL_0} \tag{3.153}$$

where F_{i_0} with $i = \{RR, RL, FR, FL\}$ are steady-state values of the a-normalized lateral forces.

$$F_{RR_0} = N_{RR}\, \mu_{f_R}(\lambda_{RR}, 0) \tag{3.154}$$

$$F_{RL_0} = N_{RL}\, \mu_{f_R}(\lambda_{RL}, 0) \tag{3.155}$$

$$F_{FR_0} = N_{FR}\, \mu_{f_F}(\lambda_{FR}, 0) \tag{3.156}$$

$$F_{FL_0} = N_{FL}\, \mu_{f_F}(\lambda_{FL}, 0) \tag{3.157}$$

lateral μ_{f_i} with $i = \{R, F\}$ are function of side-slip angles only because no longitudinal slips have been computed. Coupling between lateral and longitudinal interactions cannot be taken into account.
V_i with $i = \{RR, RL, FR, FL\}$ are actual longitudinal velocities for each contact point.

$$V_{RR} = u - \frac{1}{2} d\, \Omega \tag{3.158}$$

$$V_{RL} = u + \frac{1}{2} d\, \Omega \tag{3.159}$$

$$V_{FR} = u - \frac{1}{2} c\, \Omega \tag{3.160}$$

$$V_{FL} = u + \frac{1}{2} c\, \Omega \tag{3.161}$$

where c and d are vehicle tracks as shown in Fig.3.46. Side-slip angles for each wheel are then expressed by:

$$\lambda_{RR} = \lambda_{RL} = \frac{b\, \Omega - v}{u} \tag{3.162}$$

$$\lambda_{FR} = \lambda_{FL} = \delta - \frac{a\, \Omega + v}{u} \tag{3.163}$$

Each wheel is connected to the chassis by means of spring-damper suspension systems. Even if wheels are considered rigid, a particular formulation accounts for tire stiffness and damping. Fig.3.47 presents wheels subsystem that has been computed separately for each wheel and then

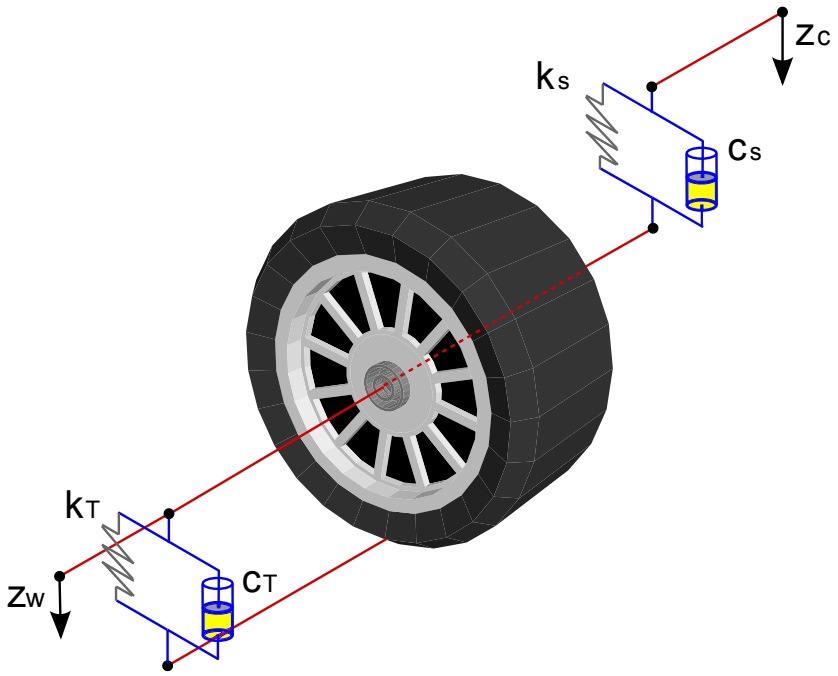

Figure 3.47: Quarter car model to describe the dynamics of each of the four wheel.

merged within the whole vehicle model at a later stage. As it is shown there are basically two main displacements: the first z_C represents vertical motion of the upper suspension point and depends on chassis body kinematics (i.e. vertical displacement, roll and pitch angles), the second z_W is wheel bodies vertical displacements and as explained above are proper degrees of freedom of the multibody system.
Each vertical movement z_i with $i = \{C, W\}$ represent the displacement for the equivalent springs includes in the two spring-damper systems (i.e. suspension and tire) for each wheel and generate spring forces. Vertical velocities (i.e. time derivatives of z_C and z_W) generate damping forces.
Regarding suspensions, z_C and its time derivative become arguments for library suspension functions described in section 2, so they can be both linear or non linear functions of suspensions stroke and velocity expressed as follows:

$$z_{C_{RR}} = -\mu\, b - \frac{1}{2}\phi\, d + z_{W_{RR}} - z \qquad \dot{z}_{C_{RR}} = -\dot{\mu}\, b - \frac{1}{2}\dot{\phi}\, d + \dot{z}_{W_{RR}} - \dot{z} \tag{3.164}$$

$$z_{C_{RL}} = -\mu\, b + \frac{1}{2}\phi\, d + z_{W_{RL}} - z \qquad \dot{z}_{C_{RL}} = -\dot{\mu}\, b + \frac{1}{2}\dot{\phi}\, d + \dot{z}_{W_{RL}} - \dot{z} \tag{3.165}$$

$$z_{C_{FR}} = \mu\, a - \frac{1}{2}\phi\, c + z_{W_{FR}} - z \qquad \dot{z}_{C_{FR}} = \dot{\mu}\, a - \frac{1}{2}\dot{\phi}\, c + \dot{z}_{W_{FR}} - \dot{z} \tag{3.166}$$

$$z_{C_{FL}} = \mu\, a + \frac{1}{2}\phi\, c + z_{W_{FL}} - z \qquad \dot{z}_{C_{FL}} = \dot{\mu}\, a + \frac{1}{2}\dot{\phi}\, c + \dot{z}_{W_{FL}} - \dot{z} \tag{3.167}$$

Vertical force due to tire compression can have different formulations as well. In this case a linear formulation with respect to vertical movement and velocity has been chosen.
Finally vertical load at each contact point is computed, and accounts for tire contribute, suspension contribute, static load due to chassis CoM (center of mass) position and wheel mass.

$$N_{RR} = g(M\, n_{R_0} + m_w R) + k_T\, z_{W_{RR}} + c_T\, \dot{z}_{W_{RR}} + \zeta(z_{C_{RR}}, \dot{z}_{C_{RR}}) \tag{3.168}$$
$$N_{RL} = g(M\, n_{R_0} + m_w R) + k_T\, z_{W_{RL}} + c_T\, \dot{z}_{W_{RL}} + \zeta(z_{C_{RL}}, \dot{z}_{C_{RL}}) \tag{3.169}$$
$$N_{FR} = g(M\, n_{F_0} + m_w F) + k_T\, z_{W_{FR}} + c_T\, \dot{z}_{W_{FR}} + \zeta(z_{C_{FR}}, \dot{z}_{C_{FR}}) \tag{3.170}$$
$$N_{FL} = g(M\, n_{F_0} + m_w F) + k_T\, z_{W_{FL}} + c_T\, \dot{z}_{W_{FL}} + \zeta(z_{C_{FL}}, \dot{z}_{C_{FL}}) \tag{3.171}$$

where N_i with $i = \{RR, RL, FR, FL\}$ are vertical load at contact points, k_T is tire stiffness, c_T is tire damping coefficient, m_{wR} and m_{wF} are rear and front wheel mass respectively, M is the chassis mass, n_{i_0} with $i = \{R, F\}$ are static normalized loads defined as follows:

$$n_{R_0} = \frac{1}{2}\frac{a}{a+b} \tag{3.172}$$
$$n_{F_0} = \frac{1}{2}\frac{b}{a+b} \tag{3.173}$$

Summarizing, the vehicle model consists of 24 differential equations: equations of motion both of the chassis and of the four wheels, first order equations, lateral forces relaxation equations(3.150-3.153), trajectory equations (1.62-1.64) and as many state variables:

$$\begin{aligned}\mathbf{x} =\{&u, v, z, \Omega, \phi, \mu, \dot{\phi}, \dot{\mu}, f_{RR}, f_{RL}, f_{FR}, f_{FL}, \dot{z},\\ &z_{W_{RR}}, z_{W_{RL}}, z_{W_{FR}}, z_{W_{FL}}, \dot{z}_{W_{RR}}, \dot{z}_{W_{RL}}, \dot{z}_{W_{FR}}, \dot{z}_{W_{FL}},\\ &s_s, s_n, \alpha\}^T\end{aligned} \tag{3.174}$$

Road states and equations have been included in the formulation following the mathematical approach introduced in section 1.3.1.

$$\dot{s} = \frac{u\cos(\alpha) - v\sin(\alpha)}{1 - nK} \tag{3.175}$$
$$\dot{n} = u\sin(\alpha) + v\cos(\alpha) \tag{3.176}$$
$$\dot{\alpha} = \omega_\psi - K\frac{u\cos(\alpha) - v\sin(\alpha)}{1 - nK} \tag{3.177}$$

The control vector consists of two elements:

$$\mathbf{u} = \{\delta, s_t\}^T \tag{3.178}$$

where δ is the steer angle and s_t is the total driving or braking force (normalized by the total weight Mg).

3.6.1 SuperCarGP2 example

To present an example of simulation for this model the same track used in section 3.1.2 is performed employing the formula car model. For the sake of simplicity same parameters of the kart model are employed herein, thus the same real kart vehicle is simulated with two different vehicle models.

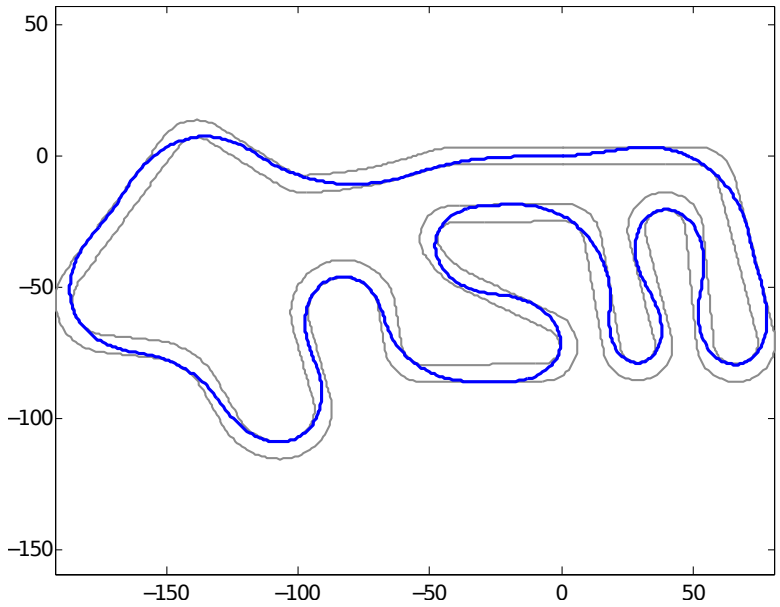

Figure 3.48: Trajectories calculated employing SuperCarGP2 model on a whole closed track.

Fig.3.49 and Fig.3.48 report results for the track lap performed by the SuperCarGP2 vehicle. Vertical displacement of the chassis together with roll and pitch motion is shown. Vertical and lateral loads are reported as well as vertical displacement of the four wheel bodies (i.e. z_W). In this case as Fig.3.49c underlines, wheels don't need to lift while cornering because of the model formulation that provides a sort of open-differential at the rear axle, thus inner and outer wheels can have different spin velocities. The second reason is because in this case wheels includes also tire deformation, thus even if one of the suspension is fully extended, tire could be still compressed and generates vertical load.

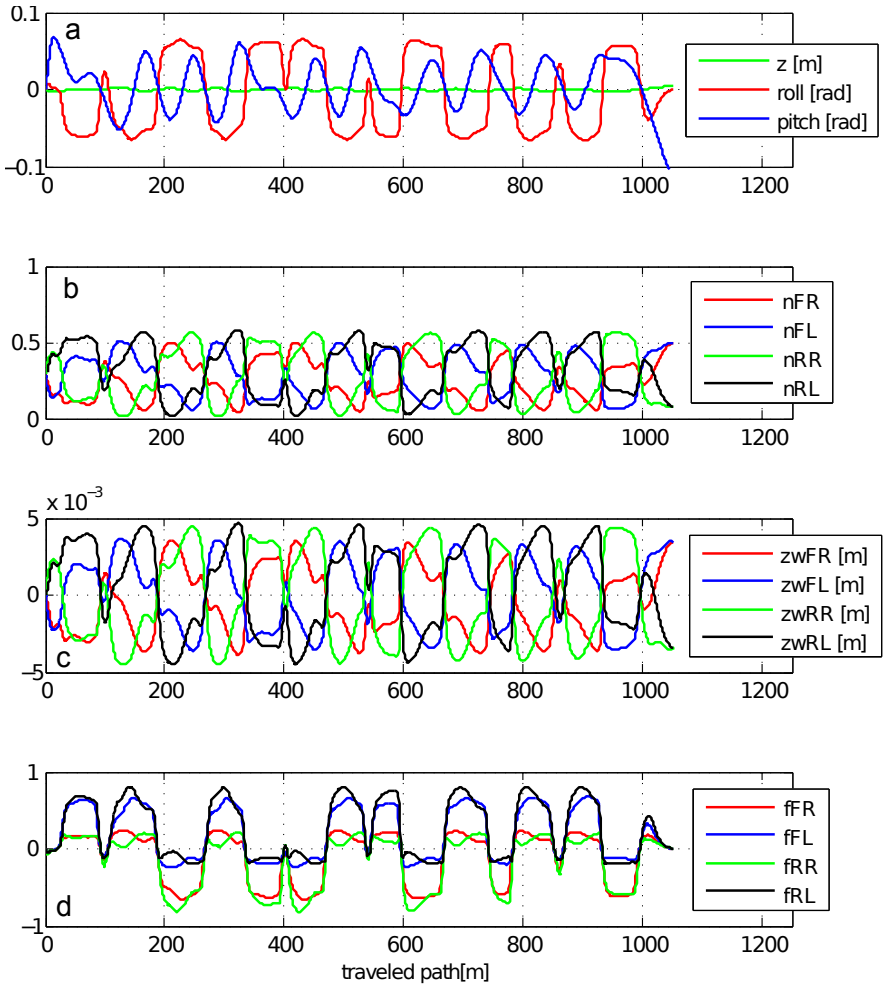

Figure 3.49: Simulation results employing SuperCarGP2 model on a whole closed track.

3.7 Superbike: full motorcycle model

The model of the motorcycle employed herein has been developed in the last years, and it's not aim of this thesis to go into details in modeling, only enhances (as aerodynamics features) will be presented afterwards. The motorcycle is represented in Fig.3.50 and includes six rigid bodies: the front and the rear frames, the front and the rear unsprung masses, the front and the rear wheels. Regarding the front frame, it includes the front suspended mass, i.e. the handlebar including different accessories connected to it, the triple clamps and the fork sprung parts. The rear frame is composed of the chassis, the engine, the tank and the rider body. Both the wheels are considered as pure moments of inertia about their spin axes, whereas their masses (tires, brake discs, etc.) are included in the unsprung masses.

The front unsprung mass includes the unsprung part of the forks and the front brake caliper, whereas the rear unsprung mass includes the swingarm and the rear brake caliper. The rear suspension is described as a non-linear torsion spring-damper system, whereas the front one as a non-linear traditional one. Suspension kinematics, elastic and damping properties are also included.

Ultimately, the motorcycle model has nine degrees of freedom: forward speed, lateral speed, yaw angle, roll angle, pitch angle, steering angle, center-of-mass vertical movement, front and rear suspension travels.

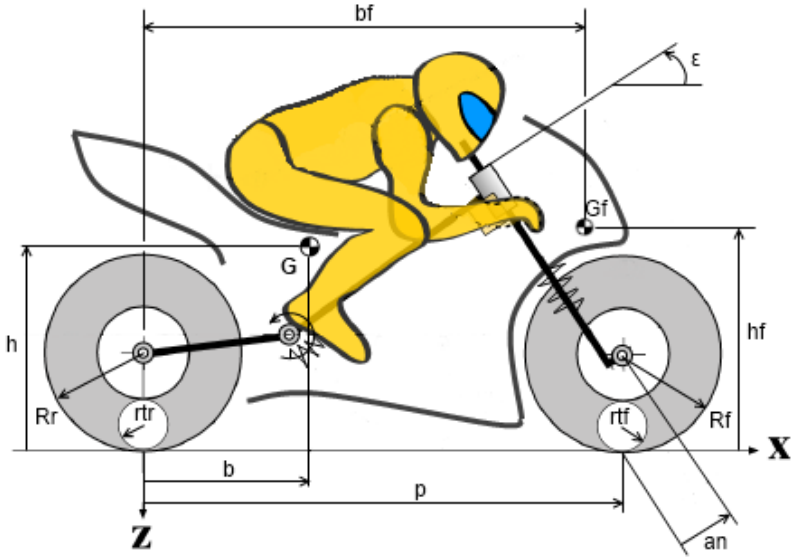

Figure 3.50: Motorcycle 9 degrees of freedom model main parameters. From [31].

Tires are modeled with a toroidal cross-section and generate three forces (i.e. longitudinal, lateral and normal forces) at the actual contact point. In particular, the lateral forces are expressed with a simplified version of the Pacejka formula as a function of the side-slip and the roll angle. Time lag is described using a first-order differential equation.

With regards to the aerodynamics, this model includes variable drag coefficient and height

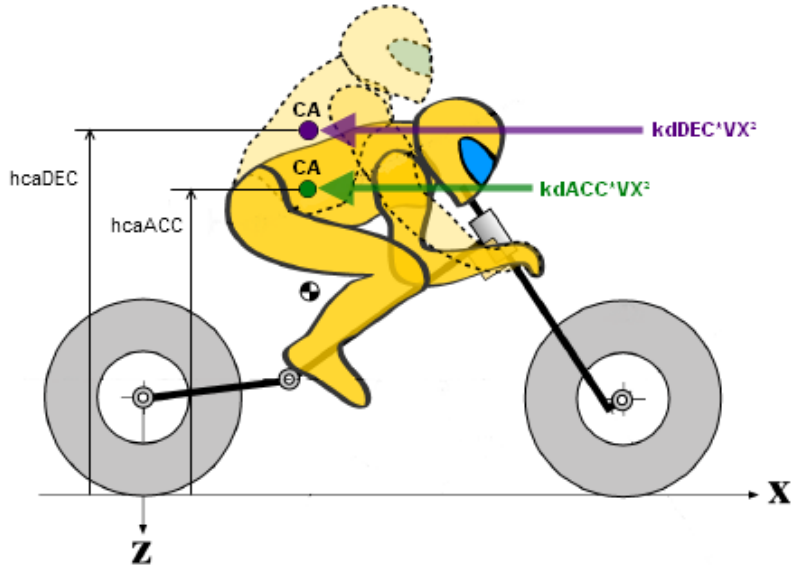

Figure 3.51: Aerodynamics parameters variation due the longitudinal acceleration: kd_{DEC} and hca_{DEC} for braking conditions and kd_{ACC} and hca_{ACC} for acceleration condition. From [31].

of the center of pressure, the point in which the aerodynamics forces are applied (Fig.3.52), described as particular functions of the longitudinal acceleration, and a fixed lift coefficient. Variable aerodynamics properties can strongly influence the different maneuvers that occur in a circuit lap, as shown by Bertolazzi, Biral [2]. In particular, they play an important role at the

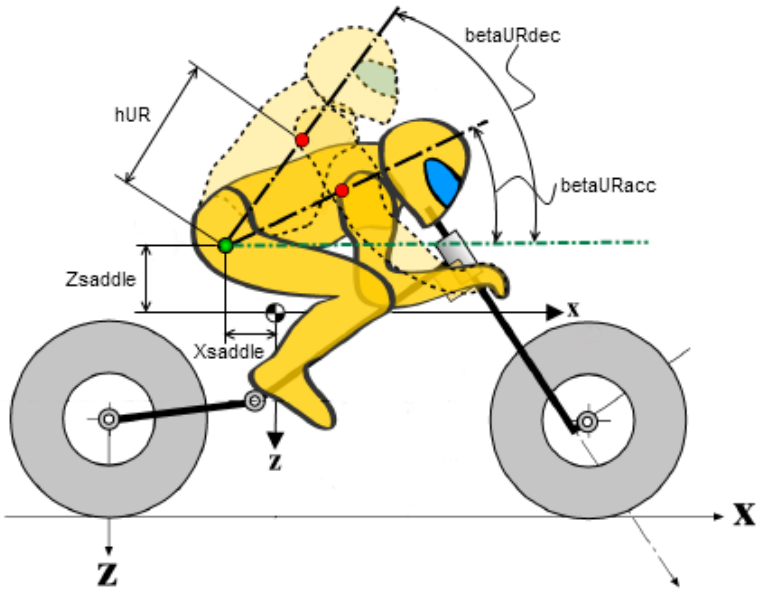

Figure 3.52: Rider movements parameters variation due the longitudinal acceleration.

entrance and at the exit of a curve in order to reach the maximum deceleration and acceleration, avoiding stoppies and wheelings.
The previous functionality do not include any movements of the rider body. To consider also the effects of mass that lifts when braking and lowers while accelerating, a moving body mass coinciding with the upper part of the rider body is included. The law of motion for this mass follows the same criteria used for drag coefficient and center of pressure height variation, and it is once more related to longitudinal acceleration.
The intention is to change the position of the CoM (i.e. center of mass) of the upper part of the rider and, as a consequence, the CoM of the whole system (i.e. rider + motorcycle). Starting from the angle $beta_{UR_{ini}}$ (i.e. corresponding to null longitudinal acceleration) the upper rider part rotates by an angle $beta_{UR}$, between two limit values (i.e. $beta_{UR_{acc}}$ and $beta_{UR_{dec}}$ with respect to a point that represents the seat point of the rider that has coordinates X_{saddle}, Z_{saddle}; the angle is measured from an horizontal axis that follows the pitch movement of the motorcycle. The upper rider mass is concentrate into a mass point at h_{UR} distance from the saddle along the rider back. For this moving body even inertia tensor is considered.
Finally the control inputs are the front and the rear longitudinal forces and the steering torque applied to the handlebar.
Regarding the road scenario, it is described in curvilinear coordinates as a list of segment of given lengths and curvatures and equations are explained in section 1.3.1.

3.8 Optimization of the center of mass position of a racing motorcycle in dry and wet track

3.8.1 Introduction

Real riders' performance is influenced by their experience and riding skills. On the contrary an 'ideal rider' [32] is able to ride a vehicle at its maximum potential, every time adapting riding style to different vehicles and different scenarios (dry and wet conditions, geometry of the path, etc.).
In a recent study Kelly and Sharp [7] support the approach of replacing the driver of a race car with inputs calculated solving an optimal control problem.
The purpose of this research is to perform an optimization based on the concept of maneuverability, i.e. the ability of a vehicle to complete a given maneuver as fast as possible without exceeding existing physical limitations, like tire adherence or road borders, but without considering the physical and mental pilot effort, that are concepts typical of handling. According to this, the choice of an ideal optimal rider is required. In this work the "Optimal Maneuver Method" is proposed as an advanced tool that can help engineers to optimize some relevant parameters of the vehicle geometry, without building prototypes, e.g. the optimization of the gearbox of a racing motorcycle proposed by Cossalter et al. [3].
This research deals with two important parameters for the behavior of a motorcycle: the height h and the longitudinal position b of the center of mass (CoM).
A study by Sakamoto et al. [33] has shown the existence of an optimal position of the center of mass, in order to reach the minimum maneuver time. It can vary with the properties of the analyzed course (i.e. corner radius, corner distance and straight length), because of the different acceleration limitations that occurs in a specific maneuver.
The importance of these two quantities h and b is essentially correlated to the concept of load transfer from the rear wheel to the front one during braking, and from the front to the rear one during acceleration and to the concept of static loads.
A higher CoM allows more load transfer to the rear wheel with an increased traction at the exit of a turn, but it can also cause wheelings (i.e. lifting of the front wheel) at lower longitudinal accelerations with respect to the standard position and the same for braking and stoppies (i.e. lifting of the rear wheel). Same considerations are also valid for the longitudinal position of the CoM which influences vertical loads on both the wheels.
The advantages or disadvantages of the choice of a particular position of the center of mass depend mainly on track geometry, engine available power and tires adherence due to wet or dry ground conditions. These can change many times during the race week-end.
This is the reason why it is very important for a racing team to have a starting point, optimized on the current conditions of the road, to submit to the rider during several round of testing.

Table 3.9: Parameters of the vehicle model.

Parameter	Symbol	Value	Unit
Gravity	g	9.81	m/s^2
Total mass (vehicle+rider)	M	136.191	kg
Center of mass height	h	0.6372	m
Center of mass longitudinal position	b	0.5925	m
Wheelbase	p	1.2318	m
Normal trail	a_n	0.0828	m
Caster angle	ϵ	0.4182	rad
Rolling moment of inertia	I_x	13.659	kgm^2
Yaw moment of inertia	I_z	19.533	kgm^2
Pitch moment of inertia	I_y	29.995	kgm^2
Mixed moment of inertia	I_{xz}	1.665	kgm^2
Front assembly yaw moment of inertia	I_δ	1.165	kgm^2
Aerodynamics center height acceleration phase	hca_{ACC}	0.5200	m
Aerodynamics center height braking phase	hca_{DEC}	0.6808	m
Aerodynamics drag coefficient acceleration phase $(0.5\rho C_x A)$	kd_{ACC}	0.116	kg/m
Aerodynamic drag coefficient braking phase $(0.5\rho C_x A)$	kd_{DEC}	0.215	kg/m
Angle of inclination of the upper rider during acceleration	$beta_{UR_{acc}}$	0.524	rad
Angle of inclination of the upper rider during braking	$beta_{UR_{dec}}$	1.310	rad
Distance between the saddle and the CoM of the upper rider	h_{UR}	0.400	m
Initial angle of inclination of the upper rider	$beta_{UR_{ini}}$	0.917	rad
X coordinate of the saddle with respect to the CoM of the system	X_{saddle}	-0.378	m
Z coordinate of the saddle with respect to the CoM of the system	Z_{saddle}	-0.188	m
Upper rider mass	m_{UR}	55.0	kg
Upper rider X inertia	IX_{UR}	2.440	kgm^2
Upper rider Y inertia	IY_{UR}	3.534	kgm^2
Upper rider Z inertia	IZ_{UR}	3.055	kgm^2

Table 3.10: Parameters of rear tire.

Parameter	Symbol	Value	Unit
Rolling radius	R_r	0.300	m
Toroid radius	t_r	0.035	m
Non-dimensional side slip stiffness		10.6267	
Non-dimensional roll stiffness		1.1174	
Relaxation length	σ	0.1348	m
Peak lateral coefficient of friction	μ_{lat}	1.375	
Peak longitudinal coefficient of friction	μ_{long}	0.950	
Vertical stiffness	K_{vert}	1.6e05	N/m

Table 3.11: Parameters of front tire.

Parameter	Symbol	Value	Unit
Rolling radius	R_r	0.285	m
Toroid radius	t_r	0.030	m
Non-dimensional side slip stiffness		10.032	
Non-dimensional roll stiffness		0.840	
Relaxation length	σ	0.1000	m
Peak lateral coefficient of friction	μ_{lat}	1.375	
Peak longitudinal coefficient of friction	μ_{long}	0.950	
Vertical stiffness	K_{vert}	1.6e05	N/m

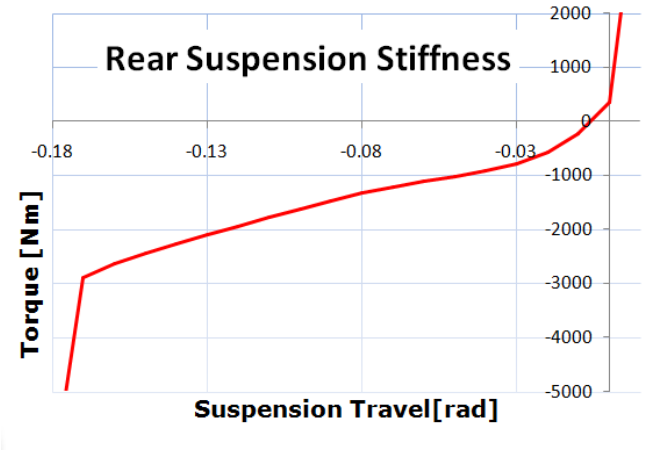

Figure 3.53: Rear suspension: torsion spring torque. From [31].

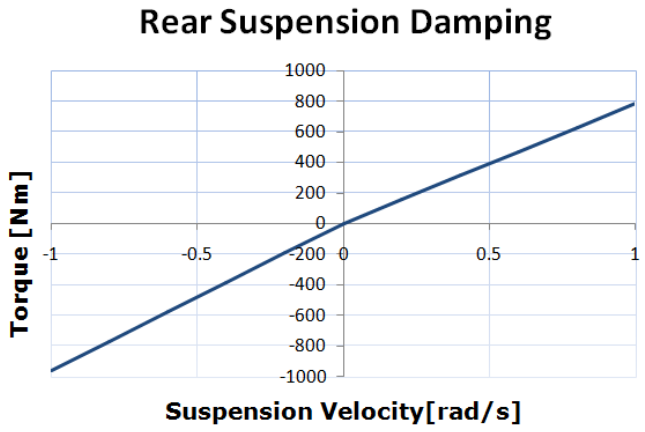

Figure 3.54: Rear suspension: torsion damper torque. From [31].

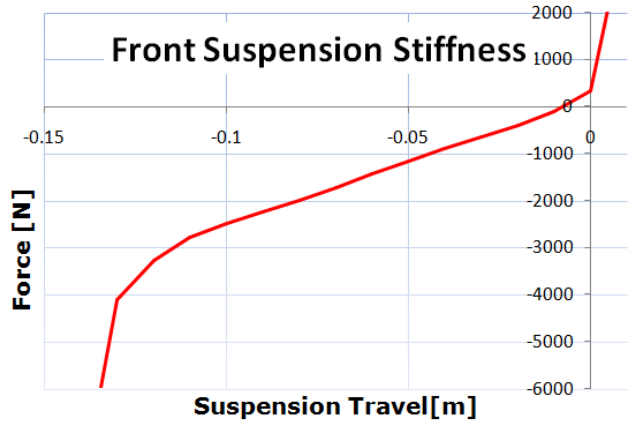

Figure 3.55: Front suspension: linear spring torque. From [31].

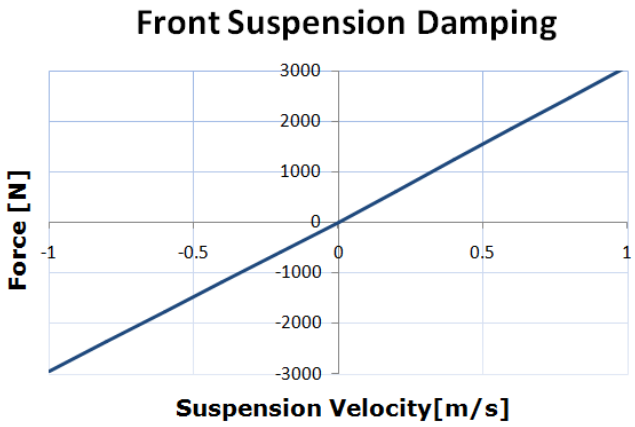

Figure 3.56: Front suspension: linear damper torque. From [31].

3.8.2 Dry and Wet riding

In this section a comparison between the "Optimal Maneuver Method" results and real telemetry data is presented. The results are referred to a test lap on the international circuit of Valencia (Comunitat Valenciana Ricardo Tormo Circuit), represented in Fig.3.59, 4005m of length and 12 m of width, performed by a 125 cc motorcycle and a professional rider in both dry and wet conditions. The same scenario is computed by means of the Optimal Maneuver Method using a motorcycle of the same category of the one used for tests. Regarding tire adherence, it does not exists any reliable method for an a priori estimation of the actual adherence limits of racing tires, and tuning adherence coefficients from g-g diagram is perhaps the only possibility available. However, g-g diagrams actually express a combination of tire adherence and rider skills and therefore the more skilled is the rider, the more reliable is the estimation of adherence.
The chosen longitudinal and lateral coefficients of adherence are reported below:

DRY conditions:
D_longitudinal = 0.950
D_lateral = 1.375

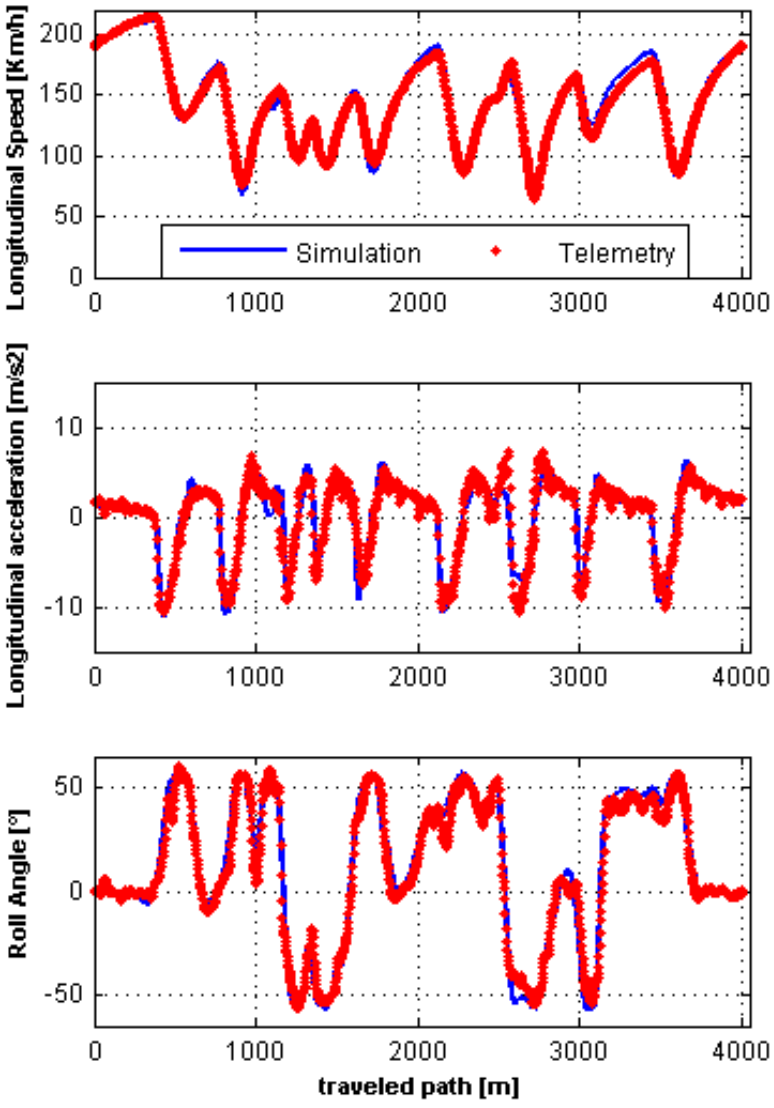

Figure 3.57: Comparison between simulations (Optimal Maneuver Method) and telemetry data. Longitudinal speed, Longitudinal Acceleration, Roll angle, in DRY conditions. From [31].

WET conditions:
D_longitudinal = 0.715
D_lateral = 0.900

Fig.3.57 and Fig.3.58 presents a comparison between the main observed variables of the sim-

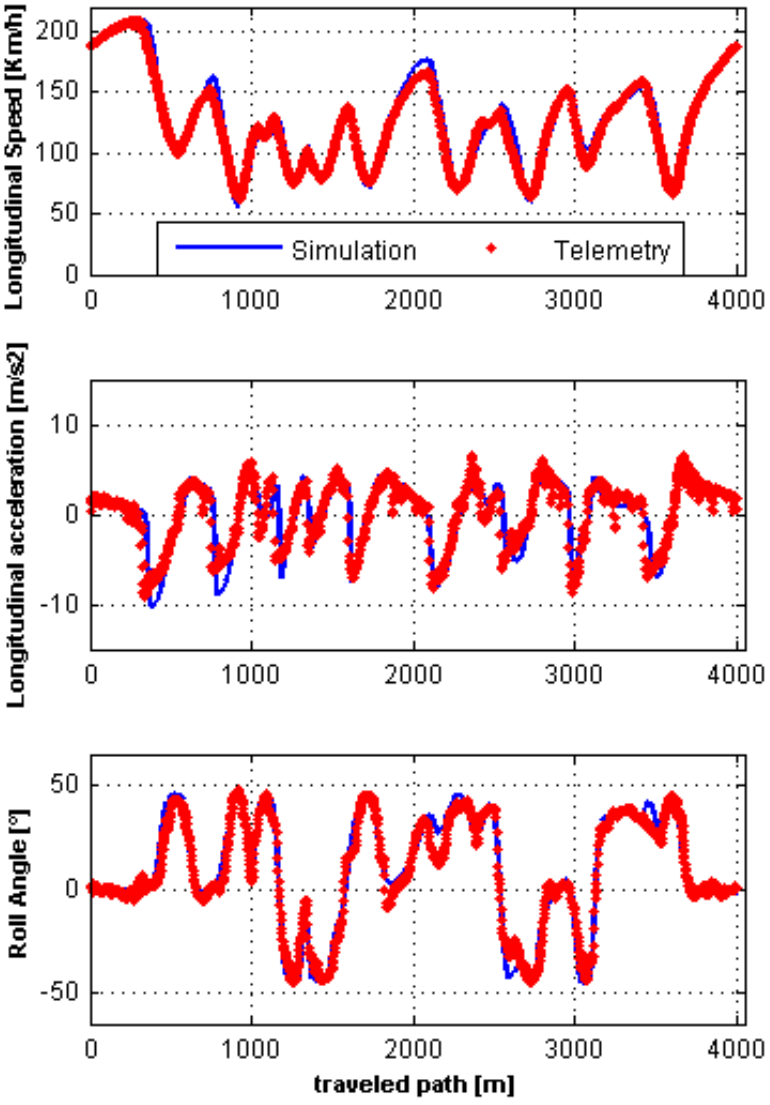

Figure 3.58: Comparison between simulations (Optimal Maneuver Method) and telemetry data. Longitudinal speed, Longitudinal Acceleration, Roll angle, in WET conditions. From [31].

ulation: the longitudinal speed, the longitudinal acceleration and the roll angle of the vehicle in both dry and wet track, and telemetry data.
The accordance between the telemetry and the simulations is quite evident for all the observed variables. Furthermore, if we compare the lap performed on the wet track with the one performed on the dry one it's possible to notice how: even though the roll angle of the vehicle

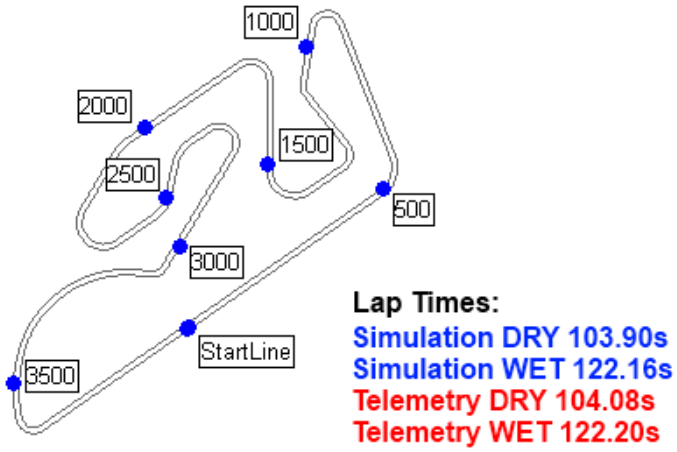

Figure 3.59: Valencia circuit track and lap times performed by Optimal Maneuver Method and real rider. From [31].

decreases drastically of about 10 degrees and the negative part of the longitudinal acceleration (i.e. braking condition) decreases too, the positive longitudinal acceleration (i.e. driving condition) do not presents particular differences for most of the parts of the track. This fact is ascribable to the low power of the considered motorcycle and has interesting effects on the longitudinal speed: although the positive longitudinal accelerations are comparable, the maximum speed reached in most of the part of the track is lower for the wet conditions. The reason of that is the less efficient braking that obliges the rider to start braking before with respect to the dry conditions.
Regarding the minimum speed in the center of each turn, it mostly depends on the roll angle, so for the wet conditions is always lower than for the dry ones.

3.8.3 Optimization of the CoM position

In order to perform an optimization of the position of the center of mass of the vehicle, in both dry and wet conditions of the road, a parametric analysis has been carried out.
The choice of this parameter is due to its paramount importance and to the possibility of adjusting it in real races. The height h and the lateral position b of the center of mass have been changed as follows:

h : 0.6172m : 0.0100 : 0.6572m
b : 0.5725m : 0.0100 : 0.6125m

Two maps of the resulted lap times for the different configurations are presented in Fig.3.60 and Fig.3.61. The first thing that can be notice is how the trend in the two maps is quite similar. The minimum lap time is performed in both cases by the motorcycle in which the center of mass is set on the highest and most backward position.
Since the whole track is considered, the reasons of such maps have to be studied in both acceleration and braking maneuvers.
With respect to acceleration, as Cossalter et al. [34] have shown, the limit between the two possible behavior of a motorcycle: the wheeling and the skidding of the rear tire, is mostly due to the longitudinal adherence tire coefficient and to the ratio b/h, between the longitudinal and

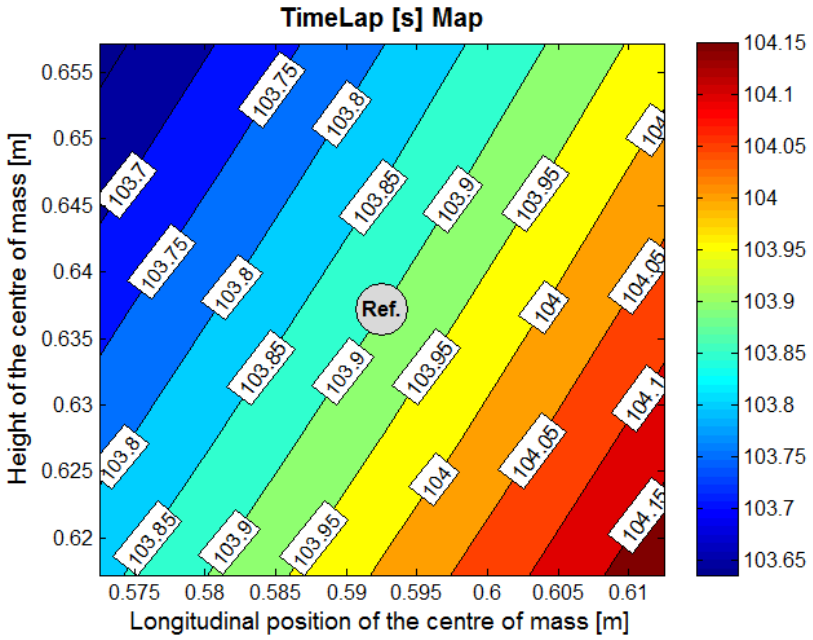

Figure 3.60: Map of the lap times due to the variation of the position of the center of mass of the vehicle in DRY conditions. From [31].

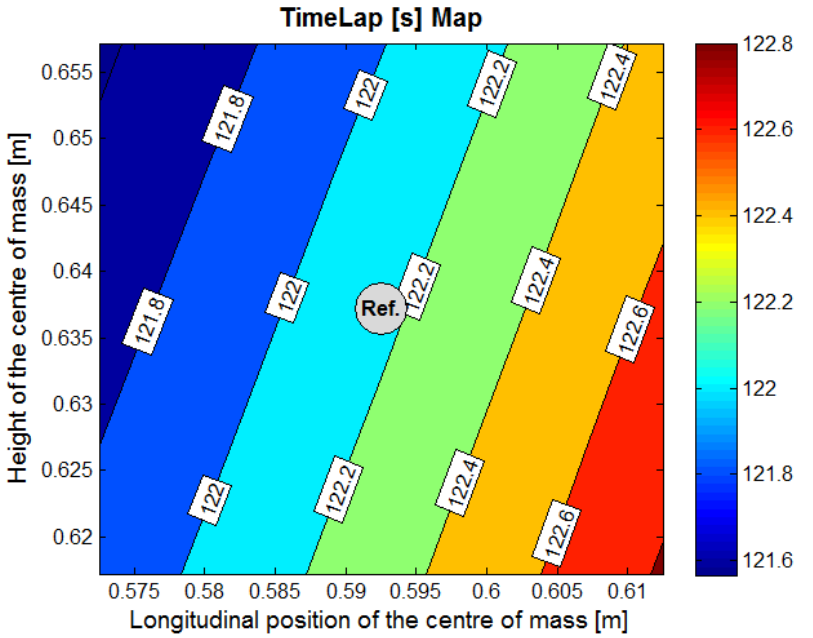

Figure 3.61: Map of the lap times due to the variation of the position of the center of mass of the vehicle in WET conditions. From [31].

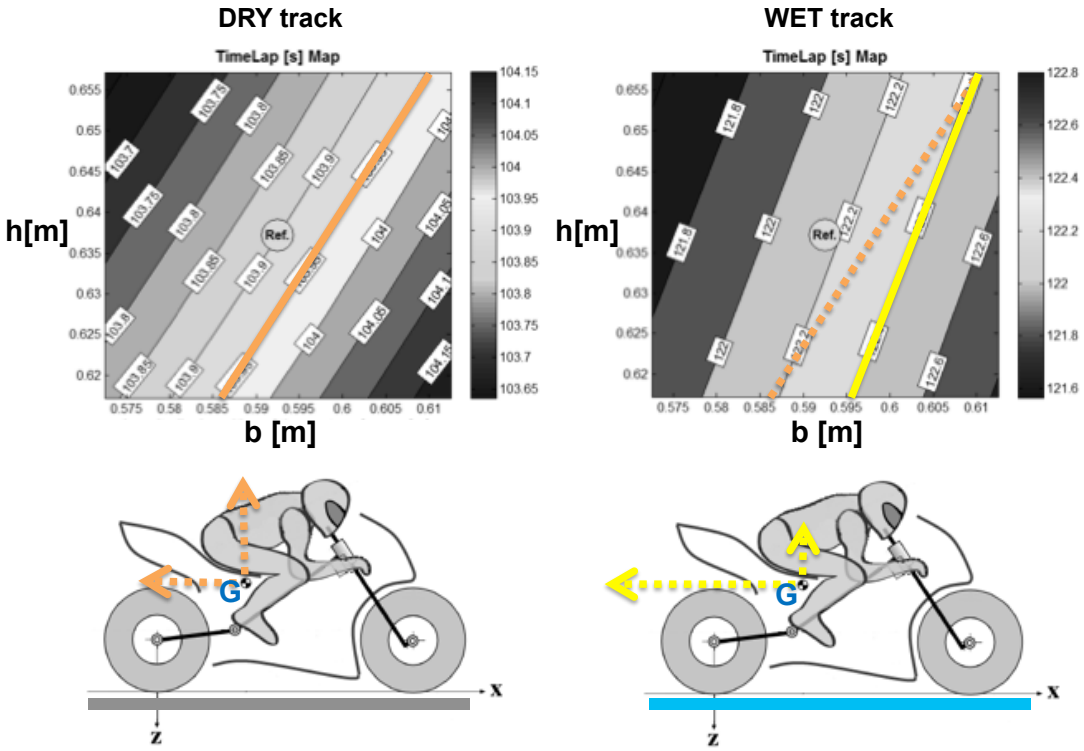

Figure 3.62: Comparison between maps of the lap times, orange and yellow yellow lines shows map areas inclination.

the vertical position of the center of mass. For the standard settings of the considered motorcycle the ratio $b/h = 0.930$ and compared with the peak of the adherence at the rear tire in both wet and dry conditions: $b/h < 0.950$ (dry), $b/h > 0.715$ (wet).
This means that for the standard settings the limit of the longitudinal acceleration is represented by the skidding of the tire for the wet track and by the wheeling for the dry one. It is important to notice that, if a motorcycle is not powerful enough the wheeling can't spontaneously occur. The limit of the acceleration for wheeling is given by:

$$x'' = g\frac{b}{h} \tag{3.179}$$

where g is the gravity acceleration.
That is $9.12\ m/s^2$ for the reference position of the center of mass and corresponds on $1242\ N$ of longitudinal force that is more than the engine can provide. Furthermore, if the worst situation for wheeling is considered (lowest b and highest h), the limit for the acceleration is $8.55\ m/s^2$ that corresponds on $1164\ N$ of longitudinal force that is once again more than the engine's possibilities. According to this, the movement of the center of mass upward and backward allows higher load transfers from the front wheel to the rear one and higher static loads on the rear wheel improving traction, without any problems of wheeling for both the conditions of the track. In addition, since in dry conditions there are not even problems of skidding of the rear wheel (in contrast to wet conditions), the optimal position of the CoM is mostly connected to the braking maneuvers.

Fig.3.62 underlines another important observation regarding the two maps is that the one which refers to the wet track presents more vertical lines than the other. This fact shows the

more importance of the longitudinal position of the center of mass for wet tracks with respect to the dry ones. The reasons of that can be found in the concept of optimal braking. In conditions of low adherence the repartition of the braking must change to perform the highest deceleration and to reach the skidding limit conditions on both the wheels at the same time as shown by Cossalter et al. [34]. Thus the use of the rear brake becomes more important than in standard conditions. The optimal repartition of the braking force due to the longitudinal adherence coefficient is shown by:

$$\frac{F_f}{F} = \frac{b + \mu\, h}{p} \tag{3.180}$$

$$\frac{F_r}{F} = \frac{(p - b) - \mu\, h}{p} \tag{3.181}$$

where:
F = total braking force
F_f = front braking force
F_r = rear braking force
p = wheelbase
μ = longitudinal adherence coefficient

For these reasons, on dry tracks the height and the longitudinal position of the CoM have about the same weight in order to reach the settings of minimum lap time, whereas on wet tracks the b parameter influences more the performance of the motorcycle because of a greater load on the rear wheel during breaking is requested.

3.8.4 Conclusions

In this work the optimal maneuver method has been applied to a $125\ cc$ motorcycle and whole track scenario by means of minimum lap time simulations. First of all, a comparison between the simulations results and real telemetry data, referring to a test lap performed by a professional rider and a motorcycle of the same category of the one used for the simulations, has been presented. The comparison has been applied on both dry and wet conditions of the track. This operation has allowed to validate the method once more. The comparison has shown good match between simulations and telemetry for all the observed variables, i.e. longitudinal speed, longitudinal acceleration, roll angle. The results of laps on dry track and of those on wet track have been analyzed and some differences and analogies have been discussed. The comparison has shown a similar trend in longitudinal positive acceleration (i.e. driving conditions), and differences in longitudinal deceleration (i.e. braking conditions), roll angle and speed profile. Furthermore, the "Optimal Maneuver Method" has been presented as a good tool for the optimization of some constants of the motorcycle geometry and inertial properties, i.e. the height and the longitudinal position of the center of mass, on different track conditions, dry and wet (i.e. varying the longitudinal and lateral tire adherence coefficients). The simulations have shown a similar trend with a minimum lap time reached in both the track conditions for a setting with the CoM placed in the most upward and backward position. In addition, a more influence of the longitudinal position of the center of mass, on the minimum lap time, has been detected in wet conditions rather than in dry ones. This has been explicated thinking to the optimal braking for low adherence conditions, in which the ratio between front and rear braking must vary in order to obtain the maximum deceleration.

Conclusions

The aim of the work presented in this thesis was to enhance a methodology for vehicle dynamics studies: the Optimal Maneuver Method.
This tool has been employed in the last ten years mainly with the intention of evaluate two motorcycle dynamic features of paramount importance: handling and maneuverability and to perform a sort of virtual prototyping of racing motorcycles employing an ideal tester capable of exploiting the vehicle at its maximum potential for each driving condition.
The intention herein was to provide a tool to perform studies for different vehicles, thus employing different vehicle models, mainly through lap time simulations but also exploring other possible optimization cost functions. In other words to extend the current methodology to other possible areas of research on vehicle dynamics. A whole chapter on dynamic optimization background has been presented with the intention of clarifying the theory on which the methodology is based on, starting from a very basic formulation and introducing one at a time conditions and constraints. The Optimal Maneuver Method applies this theory, but introduces also some peculiarities that make the difference while studying vehicle dynamics through these kind of simulations, such as the curvilinear abscissa as independent variable and a specific road description. Details have been analyzed, going deep into the mathematical formulation.
Because employing this method for different studies could lead to the formulation of a big number of models, libraries capable of managing the main components communal for different models, such as suspensions and tire-ground interactions have been developed and presented. The idea is that vehicle models and main components models could be developed separately, and just linked together after the generation of the problem equations. In this way on one side the probability of errors is drastically reduced and on the other side an important number of models are practically available, but they come from the combination of some parts that are just linked and thus a modification in one of these parts does not require a complete regeneration of every part of the model. In other words if one develops his own model for one of the communal components, then it can be shared with others for employing it on their specific vehicle model. These libraries have been widely used in most of the studies presented in the thesis and represent an important part of the Optimal Maneuver Method package that could be enriched with other formulations and models in the next years.
Regarding vehicle models, a quite complete set has been developed and presented. Starting from a fairly simple one (i.e. the single wheel running on a track) for which a complete formulation both of the model and of the optimal control problem for an example case have been presented. This last includes all the mathematical passages that lead to the set of equations

that must be solved. This model has been widely used during many of the studies to test different formulations of physical constraints, road geometry and cost functions, because of its capability of converging to the solution in almost every scenario and in a fast way. Afterwards a single-track model has been treated. Because the aim for this vehicle model was to mimic a full car behavior in very particular conditions (i.e. limit handling conditions), innovative features regarding braking system (i.e. proportioning valve) and tire-ground interaction (i.e. non-linear behavior and even off-road conditions) have been modeled. Moreover different steady states (even "aggressive") have been computed to introduce the following studies involving this model.
Two different four-wheeled car models, go-kart and formula car model, have been discussed. Whereas the first one is very specific for racing kart simulations, including rigid drive shaft and other formulation to enable lift of the wheels in curve, the second one represents a general car model, that has been thought for formula vehicles simulations aims. The multibody system (including also wheels bodies) as well as axles equations formulations are more general and thus employable for different case studies.
The last model is an update of the whole motorcycle model developed in the past, the aim of this model is basically the optimization of real racing motorcycles properties and thus the updates go in the direction of a better match of experimental data. Aerodynamics aspects and basic rider movements on the motorcycles have been treated.
For each of the mentioned case an example of application has been presented, furthermore three complete studies involving the single-track and the whole motorcycle models have been discussed in details.
Optimal control dynamic simulations involving vehicles is nowadays becoming a well-known procedure, but most of the example in literature employ fairly simple models and works in the linear region of tires as well.
The aim of the presented studies was on one side to continue with the work on virtual prototyping of racing motorcycles. On the other side to explore driving techniques for four-wheeled vehicles that are wide spread in the racing field, but whom details and aims are still uncertain.
To do this experimental evidence data recorded with professional rally drivers have been deeply analyzed, from these optimality criteria for the different techniques have been formulated, and different cost functions and tire-ground interactions conditions have been explored in order to replicate these specialized maneuvers through optimal control problem simulations. This last aspect (i.e. tire-ground interactions for different ground conditions) required an important bibliography research also on old papers published on agriculture and terramechanics field journals, including many experimental measurements of tire adhesion characteristics on different soils. Simulations involving these kind of analyses are quite new and can be considered innovative.
In conclusion at this stage the Optimal Maneuver Method can be considered a mature tool for vehicle dynamics applications and studies. On one hand its accuracy as a tool for motorcycle racing teams has been enhanced and on the other hand it is now enough flexible to be adapted to many different research applications and studies providing different vehicle models that can be simply personalized by means of the libraries.

Bibliography

[1] V. Cossalter, M. Da Lio, R. Lot, and L. Fabbri, "A general method for the evaluation of vehicle manoeuvrability with special emphasis on motorcycles," *Vehicle System Dynamics*, vol. 31, no. 2, pp. 113–135, 1999.

[2] E. Bertolazzi, F. , Biral, M. , Da Lio, and V. , Cossalter, "The influence of rider's upper body motion on motorcycle minimum time maneuvering," in *Multibody Dynamics 2007, ECCOMAS Thematic Conference, Milano, Italy*, June 2007.

[3] V. Cossalter, S. Bobbo, M. Massaro, and M. Peretto, "Application of the "optimal maneuver method" for enhancing racing motorcycle performance," *SAE International Journal of Passenger Cars - Electronic and Electrical Systems*, vol. 1, no. 1, pp. 1311–1318, 2009.

[4] D. Casanova, "On minimum time vehicle manoeuvring: the theoretical optimal lap," 2000, phD Thesis.

[5] D. Casanova, R. S. Sharp, and P. Symonds, "Minimum time manoeuvring: The significance of yaw inertia," *Vehicle System Dynamics*, vol. 34, no. 2, pp. 77–115, 2000.

[6] E. Velenis, P. Tsiotras, and J. Lu, "Optimality properties and driver input parameterization for trail-braking cornering," *European Journal of Control*, vol. 14, no. 4, pp. 308–320, 2008.

[7] D. P. Kelly and R. S. Sharp, "Time-optimal control of the race car: A numerical method to emulate the ideal driver," *Vehicle System Dynamics*, vol. 48, no. 12, pp. 1461–1474, 2010.

[8] A. Bryson, *Dynamic Optimization*. Menlo Park, CA: Addison Wesley Longman, 1999.

[9] E. Bertolazzi, F. Biral, and M. Da Lio, "Symbolic-numeric efficient solution of optimal control problems for multibody systems," *Journal of Computational and Applied Mathematics*, vol. 185, no. 2, pp. 404–421, 2006.

[10] H. Pacejka, *Tyre and Vehicle Dynamics*, 2nd ed. Butterworth-Heinemann,Oxford, 2006.

[11] E. Velenis, "Fwd vehicle drifting control: The handbrake-cornering technique," in *Proceedings of the IEEE Conference on Decision and Control*, 2011, pp. 3258–3263.

[12] Y. Khan, P. Kulkarni, and K. Youcef-Toumi, "Modelling experimentation and simulation of a brake apply system," in *American Control Conference, 1992*. IEEE, 1992, pp. 226–230.

[13] R. W. Allen and T. J. Rosenthal, "Requirements for vehicle dynamics simulation models," *SAE Technical Paper*, no. 940175, 1994.

[14] E. Velenis, D. Katzourakis, E. Frazzoli, P. Tsiotras, and R. Happee, "Steady-state drifting stabilization of rwd vehicles," *Control Engineering Practice*, vol. 19, no. 11, pp. 1363–1376, 2011.

[15] C. Voser, R. Y. Hindiyeh, and J. C. Gerdes, "Analysis and control of high sideslip manoeuvres," *Vehicle System Dynamics*, vol. 48, no. SUPPL. 1, pp. 317–336, 2010.

[16] D. Tavernini, M. Massaro, E. Velenis, D. Katzourakis, and R. Lot, "Minimum time cornering: the effect of road surface and car transmission layout," *Vehicle System Dynamics*, vol. 51, no. 10, pp. 1533–1547, 2013.

[17] M. Massaro and D. J. Cole, "Neuromuscular-steering dynamics: motorcycle riders vs car drivers," in *2012 ASME Dynamic Systems and Control Conference*, Fort Lauderdale, FL (US), 17-19 October 2012.

[18] J. P. Timings and D. J. Cole, "Vehicle trajectory linearisation to enable efficient optimisation of the constant speed racing line," *Vehicle System Dynamics*, vol. 50, no. 6, pp. 883–901, 2012.

[19] L. Segel, "Theoretical prediction and experimental substantiation of the response of the automobile to steering control," *Proceedings of the Institution of Mechanical Engineers: Automobile Division*, vol. 10, no. 1, pp. 310–330, 1956.

[20] T. D. Gillespie, *Fundamentals of Vehicle Dynamics*. SAE International, 1992.

[21] H. Dugoff, P. S. Fancher, and L. Segel, "An analysis of tire traction properties and their influence on vehicle dynamic performance," *SAE Technical Paper*, no. 700030, 1970.

[22] J. Y. Wong, *Theory of Ground Vehicles*. John Wiley and Sons, 2001.

[23] W. R. Allen, T. J. Rosenthal, and J. P. Chrstos, "Vehicle dynamics tire model for both pavement and off-road conditions," *SAE Special Publications*, vol. 1228, pp. 27–38, 1997.

[24] C. Harnisch, B. Lach, R. Jakobs, M. Troulis, and O. Nehls, "A new tyre-soil interaction model for vehicle simulation on deformable ground," *Vehicle System Dynamics*, vol. 43, no. SUPPL., pp. 384–394, 2005.

[25] C. Senatore and C. Sandu, "Off-road tire modeling and the multi-pass effect for vehicle dynamics simulation," *Journal of Terramechanics*, vol. 48, no. 4, pp. 265–276, 2011.

[26] T. O'Neil, *Rally Driving Manual*. Team O'Neil Rally School and Car Control Center, 2006.

[27] M. Abdulrahim, "On the dynamics of automobile drifting," *SAE paper*, 04 2006.

[28] E. Velenis, P. Tsiotras, and J. Lu, "Aggressive maneuvers on loose surfaces: Data analysis and input parametrization," in *Control Automation, 2007. MED '07. Mediterranean Conference on*, june 2007, pp. 1 –6.

[29] J. P. Timings and D. J. Cole, "Minimum maneuver time calculation using convex optimization," *Journal of Dynamic Systems, Measurement, and Control*, vol. 135, no. 3, 2013.

[30] D. Katzourakis, E. Velenis, D. Abbink, R. Happee, and E. Holweg, "Race-car instrumentation for driving behavior studies," *IEEE Transactions on Instrumentation and Measurement*, vol. 61, no. 2, pp. 462–474, 2012.

[31] V. Cossalter, R. Lot, and D. Tavernini, "Optimization of the centre of mass position of a racing motorcycle in dry and wet track by means of the "optimal maneuver method"," in *Mechatronics (ICM), 2013 IEEE International Conference on*. IEEE, 2013, pp. 412–417.

[32] F. Biral and M. DaLio, "Modelling drivers with the optimal maneuver method," in *Proceedings of the Seventh International Conference and Exhibition of the Associazione Tecnica dell'Automobile (ATA2001), Florence, Italy*, no. paper 01A1029, may 2001.

[33] M. Sakamoto, S. , Kubo, T. , Kubota, T. , Inukai, and E. , Yagi, "Optimal motorcycle configuration with performance limitations," *SAE Technical Paper*, no. 2007-32-0123, 2007.

[34] V. Cossalter, *Motorcycle dynamics*. Lulu.com, Raleigh, North Carolina, 2006.